الجمهورية الجزائرية الديمقراطية الشعبية

Democratic and Popular Republic of Algeria

Ministry of Higher Education and Scientific Research

FERHAT ABBAS UNIVERSITY - SETIF1

FACULTY OF TECHNOLOGY

THESIS

Submitted to the Department of Electronics

In Fulfilment of the Requirements for the degree of

DOCTORATE

Domain: Science and Technology

Field: Electronic **Specialty: Microelectronics**

By

MERABET MOUSSA

THEME

Contribution to the Study of Cu-III-VI$_2$ Compounds

Defended on 06/11/2025 in front of Jury:

Pr. SEMCHEDDINE Samia	University of Setif 1	President
Dr. LAIB Salah Eddine	University of Setif 1	Supervisor
Pr. BOUCHAMA Idris	University of M’sila	Co-Supervisor
Dr. ADJROUD Faiza	University of Setif 1	Examiner
Pr. KHELLIL Abdellatif	University of El Oued	Examiner
Pr. DAAMOUCHE Abdelhamid	University of Boumerdas	Examiner

Dedication

I dedicate this humble work to my beloved parents, my dear father and mother, whose constant support and encouragement have been the solid foundation of my academic journey. I pray to Allah to bless their lives and protect them always.

To my dear brothers: Samir, Djamal Eddine, Chems Eddine, and all their children, and to my sister Afaf and her esteemed family.

To my friends who stood by me throughout this journey, especially my close friends: Dr. Islam Tawahria, Habib Bai, Souhaib Louda, Saidi Fayçal, and Tawafok Abdelraouf.

To all my colleagues at work, who shared with me the effort and were a source of support and encouragement along this path.

Merabet Moussa

Acknowledgement

First and foremost, I am profoundly grateful to Almighty Allah, who has granted me health, strength, and patience, and who has blessed me with the determination and perseverance to bring this thesis to completion.

I wish to express my deepest appreciation to my supervisor, ***Dr. Laib Salaheddine****, Professor at the University of Setif 1, for his insightful guidance, rigorous follow-up, and invaluable support throughout the course of this research. My heartfelt gratitude is also extended to my co-supervisor,* ***Prof. Idris Bouchama****, Professor at the University of M'sila, whose continuous encouragement and constructive advice were essential to the completion of this work.*

I also remain indebted to my former supervisors, ***Prof. Messous Ammar*** *(now retired) and* ***Prof. Chihi Tayeb*** *(may Allah have mercy on him), whose mentorship and guidance played a significant role in shaping my academic journey.*

My sincere thanks are further addressed to the distinguished members of the examining committee: ***Prof. Semcheddine Samia*** *from the University of Setif 1, President of the Jury;* ***Dr. Adjroud Faiza*** *from the University of Setif 1, Examiner;* ***Prof. Khellil Abdellatif*** *from the University of El Oued, Examiner; and* ***Prof. Daamouche Abdelhamid*** *from the University of Boumerdas, Examiner. Their acceptance to evaluate this thesis and their anticipated constructive feedback are deeply appreciated.*

Finally, I wish to acknowledge with gratitude all my professors in the Department of Electronics, as well as all my esteemed teachers from whom I had the honor to learn. Their dedication and knowledge have left an enduring mark on my academic and personal development.

Merabet Moussa

TABLE OF CONTENTS

Chapter I: Fundamentals and Structures of Solar Cells

Chapter II: Ab Initio Computational Techniques and Solar Cell Simulation Tools

Chapter III: Results and Discussion

Chapter IV: Photovoltaic Application of CuIn($Se_{1-x}S_x$) materials

List of Abbreviations

$\alpha(\omega)$: Absorption Coefficient
B : Bulk Modulus
B_0 : Pressure Derivative of the Bulk Modulus
CASTEP : Cambridge Sequential Total Energy Package
CB : Conduction Band
CBM : Conduction Band Minimum
CIS : $CuInS_2$
CISe : $CuInSe_2$
CISSe : $CuIn(Se_{1-x}S_x)_2$
DFT : Density Functional Theory
DOS : Density of States
E : Energy
Eg : Band Gap Energy
$\varepsilon(\omega)$: Dielectric Function
GGA : Generalized Gradient Approximation
GGA-PBE : Generalized Gradient Approximation of Perdew–Burke–Ernzerhof
GGA-PBESol : Generalized Gradient Approximation of Perdew–Burke–Ernzerhof for solids
$\hbar\omega$: Photon Energy
LDA : Local Density Approximation
$n(\omega)$: Refractive Index
PBE : Perdew–Burke–Ernzerhof
PDOS : Partial Density of States
PP : Pseudopotential
$R(\omega)$: Reflectivity
SCAPS-1D : Solar Cell Capacitance Simulator – One Dimensional
TDOS : Total Density of States
VB : Valence Band
VBM : Valence Band Maximum

List of Tables

Chapter III: Results and Discussion

Chapter IV: Photovoltaic Application of CuIn(Se_{1-x} S_x)$_2$ materials

List of Figures

Chapter I: Fundamentals and structures of solar cells

Chapter II: Ab Initio Computational Techniques and Solar Cell Simulation Tools

Chapter III: Results and Discussion

Chapter IV: Photovoltaic Application of $CuIn(Se_{1-x}S_x)_2$ Materials

General Introduction

General introduction

The current global energy landscape is undergoing a critical transformation driven by the convergence of environmental, economic, and social challenges. Since the 1980s, humanity has exceeded the Earth's biocapacity, placing immense stress on natural ecosystems and accelerating climate change [1]. Continued reliance on fossil fuels is unsustainable, not only due to resource depletion but also because of their significant contribution to greenhouse gas emissions and global warming [2]. At the same time, energy demand continues to rise, particularly in developing regions where over one billion people remain without access to reliable electricity. Addressing this dual challenge of sustainability and accessibility requires a decisive transition toward renewable, clean, and decentralized energy sources.

Among renewable options, solar energy emerges as one of the most promising and scalable. The sun delivers to Earth in just one hour more energy than humanity consumes in an entire year, highlighting its vast potential as a cornerstone of a sustainable energy future [3]. Unlike other renewables, solar power can be harvested at multiple scales from utility-scale plants to small off-grid installations making it adaptable to diverse geographic and socioeconomic contexts. Photovoltaic (PV) technologies, which directly convert sunlight into electricity using semiconductor materials, offer a simple, silent, and modular route to clean energy with minimal environmental impact.

The technological evolution of PV cells has advanced through successive generations. First-generation crystalline silicon cells dominate the market due to their maturity and relatively high efficiencies, reaching ~25% in laboratories and 15–20% in commercial modules [4]. However, their rigid structures, energy-intensive fabrication, and high material consumption limit flexibility and cost-effectiveness. In response, second-generation thin-film technologies were introduced, exploiting highly absorbing semiconductors that enable efficient light capture with films only a few micrometres thick, compared to the 200–300 µm required for silicon [5]. These thin-film devices offer lower production costs, lightweight and flexible modules, and shorter energy payback times.

Among thin-film absorbers, copper-based chalcogenide semiconductors such as $Cu(In,Ga)Se_2$ (CIGS) and $Cu_2ZnSn(S,Se)_4$ (CZTS) stand out due to their excellent optoelectronic performance and composition from relatively earth-abundant elements [6]. Chalcopyrite-type compounds such as $CuInSe_2$ (CISe) and $CuInS_2$ (CIS) are particularly attractive owing to their direct, tunable band gaps (~1.0–1.5 eV), strong visible-light absorption coefficients (>10^5 cm^{-1}), and resilience to photodegradation [1,7].

To improve efficiency and spectral adaptability, research has increasingly focused on the quaternary alloy $CuIn(Se_{1-x}S_x)_2$ Substituting Se with S allows band-gap engineering in the optimal range of 1.0–1.5 eV, enabling improved matching with the solar spectrum and higher device performance [8,9]. Sulfur incorporation can also enhance thermal stability and reduce defect states, which often limit efficiency in the pure compounds. Thus, tuning the S/Se ratio provides a powerful strategy for tailoring the electronic structure, optical absorption, and defect chemistry of the absorber layer.

Several experimental and theoretical studies have investigated the properties of $CuIn(Se_{1-x}\ S_x)_2$ alloys; notably, Chiang et al. established a one-pot heating-up synthesis that enables gram-scale production of $CuIn(Se_{1-x}\ S_x)_2$ nanocrystals with precise control of the S/Se ratio and systematic band-gap tuning within the chalcopyrite framework. Replacing the solvothermal example to align with this reference: “Several experimental and theoretical studies have investigated the properties of $CuIn(Se_{1-x}\ S_x)_2$ alloys; in particular, a facile heating-up route affords composition-controlled $CuIn(Se_{1-x}\ S_x)_2$ nanocrystals that exhibit predictable lattice and band-gap shifts as the anion ratio is varied, consistent with tunable absorber design for thin-film photovoltaics[10] , while Eisener et al. [11] reported significant sulfur effects on optoelectronic behavior in Bridgman-grown crystals. Wang et al. [12] examined sulfurisation conditions in thin films, and Chen et al. [7] used first-principles calculations to reveal band structure modifications due to sulfur. Additional work by Sheppard et al. [13] and Zeaiter & Llinares [14,15] explored phase uniformity and optical constants, further supporting their potential in solar applications. Despite these advances, most studies are limited to the end-member compositions ($x = 0$ or $x = 1$), leaving a research gap across the intermediate range.

To address this, the present work integrates advanced density functional theory (DFT) calculations using CASTEP within Materials Studio [16,17] with device-level simulations in SCAPS-1D [18]. DFT, employing the generalized gradient approximation (GGA) of Perdew–Burke–Ernzerhof [14], provides atomistic insights into structural, electronic, and optical properties, including band gaps, dielectric functions, reflectivity, and optical conductivity. These microscopic data are then used in SCAPS-1D simulations to evaluate macroscopic photovoltaic performance, specifically short-circuit current density (Jsc), open-circuit voltage (Voc), fill factor (FF), and power conversion efficiency.

The aim of this thesis is to bridge the gap between first-principles modeling and full-device simulation, thereby offering a multi-scale framework to understand and optimize $CuIn(Se_{1-x}S_x)_2$ based solar cells. Special emphasis is placed on:
(a) systematically studying alloy properties across the full compositional spectrum;
(b) optimizing absorber thickness, doping, and defect control using SCAPS-1D; and
(c) proposing and evaluating hybrid cell architectures for enhanced efficiency.

The thesis is organized as follows:

- Chapter I introduces the fundamentals of solar energy and PV technologies, with emphasis on chalcopyrite absorbers.
- Chapter II presents the theoretical foundations of first-principles methods, particularly DFT, and their application to chalcopyrite semiconductors.
- Chapter III reports a comprehensive DFT investigation of $CuIn(Se_{1-x}S_x)_2$ properties across the full S/Se range.
- Chapter IV details device-level simulation and optimization using SCAPS-1D, supported by in-depth photovoltaic performance analysis.

This synergy of atomistic modeling and device simulation provides both fundamental insights and practical guidelines for advancing efficient, stable, and cost-effective thin-film solar cells suitable for large-scale deployment under diverse conditions.

Moreover, this research aims to fill the existing knowledge gap concerning the full compositional range of $CuIn(Se_{1-x}S_x)_2$ alloys by leveraging state-of-the-art quantum mechanical models alongside device simulations to propose optimized material and device structures with enhanced photovoltaic performance. The core novelty lies in systematically linking atomistic understanding with pragmatic device engineering, thus paving the path for scalable, efficient, and environmentally sustainable solar technologies.

The anticipated outcomes are expected to inform future experimental work and industrial applications, contributing to the global drive for sustainable energy solutions aligned with climate action goals and energy equity.

References

1. Fthenakis, V. (2009). Sustainability of photovoltaics: The case for thin-film solar cells. Renewable & Sustainable Energy Reviews, 13, 2746–2750.

2. Mitzi, D. B., Gunawan, O., Todorov, T., Wang, K., & Guha, S. (2011). The path towards a high-performance solution-processed kesterite solar cell. Solar Energy Materials & Solar Cells, 95, 1421–1436.

3. Miles, R. W., Hynes, K. M., & Forbes, I. (2005). Photovoltaic solar cells: An overview. Progress in Crystal Growth and Characterization of Materials, 51(1–3), 1–42.

4. Jehl, Z., Erfurth, F., Naghavi, N., Lombez, L., Gerard, I., Bouttemy, M., ... & Lincot, D. (2011). Thinning of CIGS solar cells: Part II: Cell characterizations. *Thin solid films*, *519*(21), 7212-7215..

5. Paire, M., et al. (2010). Toward microscale Cu(In,Ga)Se_2 solar cells. Journal of Applied Physics, 108(3), 034907.

6. Becquerel, E. (1839). Mémoire sur les effets électriques produits sous l'influence des rayons solaires. Comptes Rendus, 9, 561–567.

7. Chen, H., et al. (2017). First-principles study on sulfur doping in $CuInSe_2$. Computational Materials Science, 136, 83–90.

8. Xiao, X., et al. (2018). Solvothermal synthesis of $CuIn(Se_{1-x}S_x)_2$ and band gap tuning. Journal of Alloys and Compounds, 762, 742–750.

9. Bekker, J. (2009). Band-gap engineering in CuIn $(Se, S)_2$ absorbers for solar cells. *Solar energy materials and solar cells*, *93*(5), 539-543.

10. Chiang, M. Y., Chang, S. H., Chen, C. Y., Yuan, F. W., & Tuan, H. Y. (2011). Quaternary CuIn (S1− x Se x) 2 nanocrystals: facile heating-up synthesis, band gap tuning, and gram-scale production. *The Journal of Physical Chemistry C*, *115*(5), 1592-1599.

11. Eisener, B., Wolf, D., & Müller, G. (2000). Influence of sulphur on the electrical and optical properties of p-type CuIn (SxSe1− x) 2 single crystals. *Thin solid films*, *361*, 126-129.

12. Wang, C., Zhu, C., Zhang, T., & Li, J. (2013). CuIn (S, Se) 2 thin films prepared by selenization and sulfurization of sputtered Cu–In precursors. *Vacuum*, *92*, 7-12.

13. Clark, S. J., et al. (2005). First principles methods using CASTEP. Zeitschrift für Kristallographie, 220(5–6), 567–570.

14. Perdew, J. P., Burke, K., & Ernzerhof, M. (1996). Generalized Gradient Approximation Made Simple. Physical Review Letters, 77(18), 3865–3868.

15. Zeaiter, K., Yanuar, A., & Llinares, C. (2001). Off-stoichiometry effect on the CuInSe2 dielectric function. Solar energy materials and solar cells, 70(2), 213-218.

16. Kohn, W., & Sham, L. J. (1965). Self-consistent equations including exchange and correlation effects. Physical review, 140(4A), A1133.

17. Lv, H., Gao, H., Yang, Y., & Liu, L. (2011). Density functional theory (DFT) investigation on the structure and electronic properties of the cubic perovskite PbTiO3. *Applied Catalysis A: General*, *404*(1-2), 54-58.

18. Al-Hattab, M., Moudou, L. H., Khenfouch, M., Bajjou, O., Chrafih, Y., & Rahmani, K. (2021). Numerical simulation of a new heterostructure CIGS/GaSe solar cell system using SCAPS-1D software. solar energy, 227, 13-22.

Chapter I

Fundamentals and structures of solar cells

I.1 Introduction

A clean, abundant, and sustainable resource, solar energy has the potential to satisfy the world's expanding energy needs. A key component in capturing this energy is photovoltaic solar cells, which directly transform sunlight into electrical power. Thin-film solar cells based on copper-containing semiconductors, such as $Cu(In,Ga)Se_2$ and $Cu_2ZnSn(S,Se)_4$, have garnered a lot of interest among different solar cell technologies because of their high absorption efficiency and utilization of earth-abundant elements. Setting the stage for the experimental and modeling investigations included in this thesis, this chapter presents the basic ideas of solar energy conversion, types of solar cells, and focuses on copper-based materials.

I.2 Solar energy

A clean power source that originates from the sun's rays is solar energy. Systems such as solar panels, which convert sunlight into electrical power using photovoltaic cells, or thermal collectors, which use solar heat to generate energy or warm areas, can be used to capture it. Since this energy source doesn't release any toxins while in use, it is environmentally benign. It provides a sustainable way to lessen reliance on fossil fuels and lower electricity prices. Thanks to technological advancements, solar technology is now more affordable and efficient for both homes and businesses [1].

I.2.1 Solar thermal energy

The process produces heat by transforming visible sunlight into infrared radiation, which is subsequently applied to a fluid or substance that undergoes a phase shift. It is dependent upon thermal collectors, which are made with particular technologies according to the necessary temperature range.

I.2.2 Photovoltaic solar energy:

Through the use of photovoltaic modules, which are constructed of solar cells made of semiconducting materials, sunlight is directly converted into electrical power.

I.2.2.1 Photovoltaic solar energy principle

It depends on the concept of directly generating electricity from sunlight. Solar cells, which are usually composed of semiconductor materials like silicon, are used to do this. When sunlight contacts a cell's surface, the light's energy causes electrons inside the substance to come loose. An electric current is subsequently produced when these liberated electrons flow through the cell. [2]

An inverter can be used to transform the direct current (DC) electricity produced by solar panels into alternating current (AC) for use in homes and businesses. This process is called the photovoltaic effect. How well the materials are made and how much sunshine is received determine how effective this conversion is.

I.3 Structure of solar cells

Typically, a solar cell more specifically, a conventional silicon-based photovoltaic cell—consists of several layers, each of which has a specific function in effectively transforming sunlight into electrical energy [3]. Silicon solar cells are commonly produced using materials such as thin films, polycrystalline wafers, or single-crystal wafers. A large, high-quality crystal ingot is cut into single-crystal wafers, which are between one-third and half a millimeter thick. This item is created by pulling molten silicon at temperatures of roughly 1400 °C, which is a costly and technically difficult process. Silicon needs to be extremely pure and have a nearly flawless crystal structure in order to absorb sunlight efficiently.

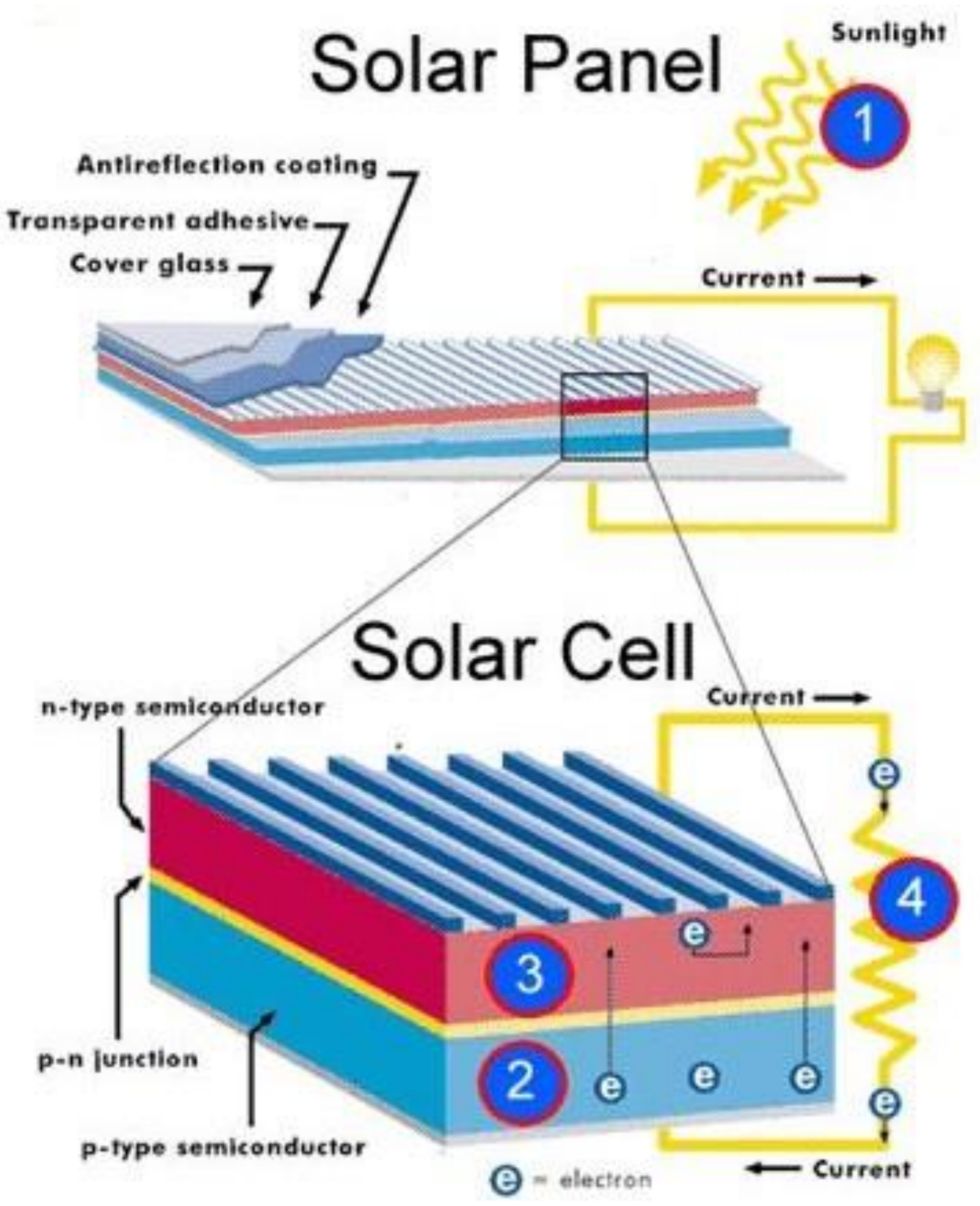

FigureI.1: Structure of solar cell

I.3.1 Glass cover

Acts as a barrier in a solar cell to keep out elements including dust, moisture, and impact. Constructed from sturdy tempered glass, it also lets the most sunlight into the active layers below, guaranteeing effective energy conversion while preserving the solar panel's longevity and structural integrity[4].

I.3.2 Anti-reflective coating (ARC)

Is a thin coating that is put on solar cells' surface to reduce sunlight reflection. It increases the quantity of solar energy absorbed by the cell and boosts efficiency by decreasing light loss. Because of its exceptional optical qualities and resilience, silicon nitride (Si_3N_4) is widely utilized and an essential part of contemporary solar technology[5].

I.3.3 Front contact

Usually composed of silver or other conductive metals, it creates a surface pattern resembling a grid [6]. Its main objective is to gather and move the electrons produced by sunlight. The design enhances the overall performance of the cell by letting the most light through while conducting electricity effectively.

I.3.4 n-type silicon layer

Composed of surplus electrons and forms the negative side of the p-n junction when silicon is doped with phosphorus [7]. . It is essential for conducting sunlight-generated electrons..

I.3.5 p-n junction

Is the central area of a solar cell that produces power. When exposed to sunlight, the electric field created by the meeting of p-type and n-type silicon layers effectively separates charge carriers and permits current flow by pushing electrons to the n-side and holes to the p-side.

I.3.6 Back contact

Typically composed of aluminum, it collects and conducts the electrons that flow through the cell to complete the electrical circuit [6]. It is positioned at the bottom and improves overall efficiency and power output by reflecting unabsorbed light back into the cell and provide structural support.

I.4 Types of solar cells

Solar cells come in a variety of forms, each with its own materials, architectures, efficiency, and uses [8].

I.4.1. Crystalline silicon (c-Si) solar cells

Represent the most popular photovoltaic technology, making up more than 90% of the world's solar market. Monocrystalline and polycrystalline are their two primary varieties.

I.4.1.1 Monocrystalline cells

These cells have a sleek black appearance and a higher efficiency (18–22%) since they are composed of a single, pure silicon crystal. Because of their better performance, they are perfect for small places, but they cost more.

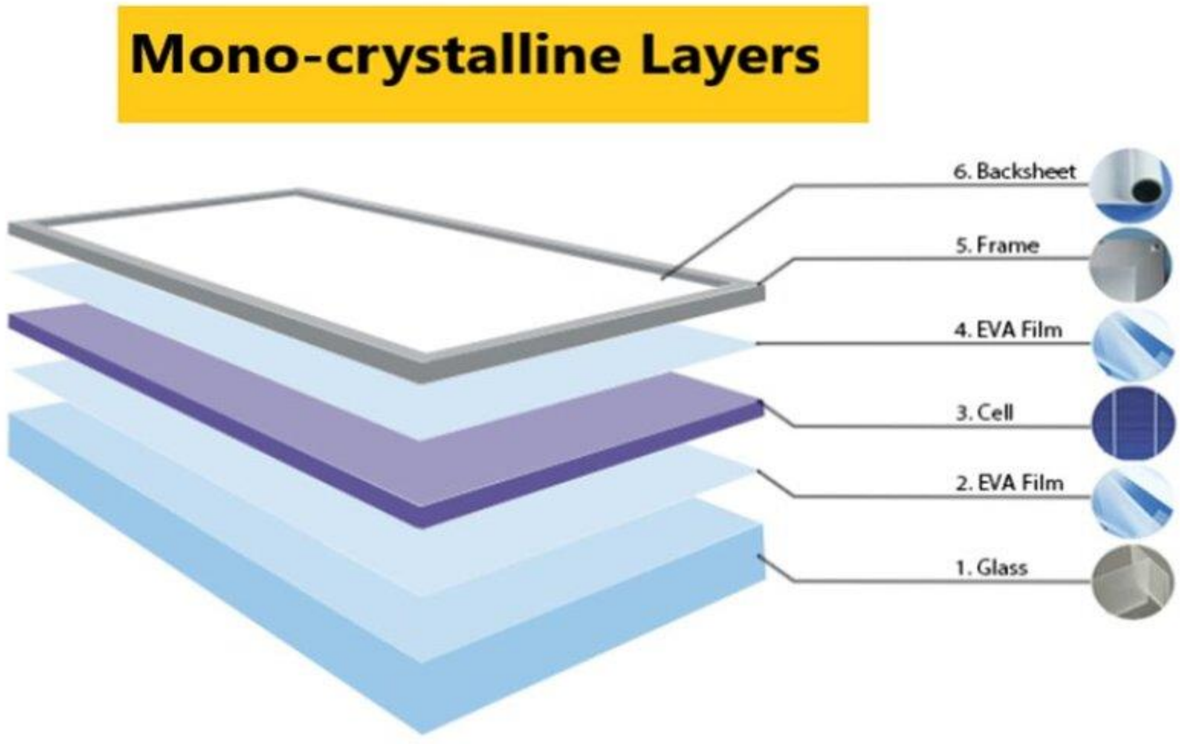

Figure I 2 : Crystalline Silicon Cell

I.4.1.2 Polycrystalline cells

These cells are more reasonably priced but marginally less effective (15–18%) and have a bluish, speckled appearance. They are produced from melted silicon fragments. Both varieties have long lifespans often more than 25 years.

.

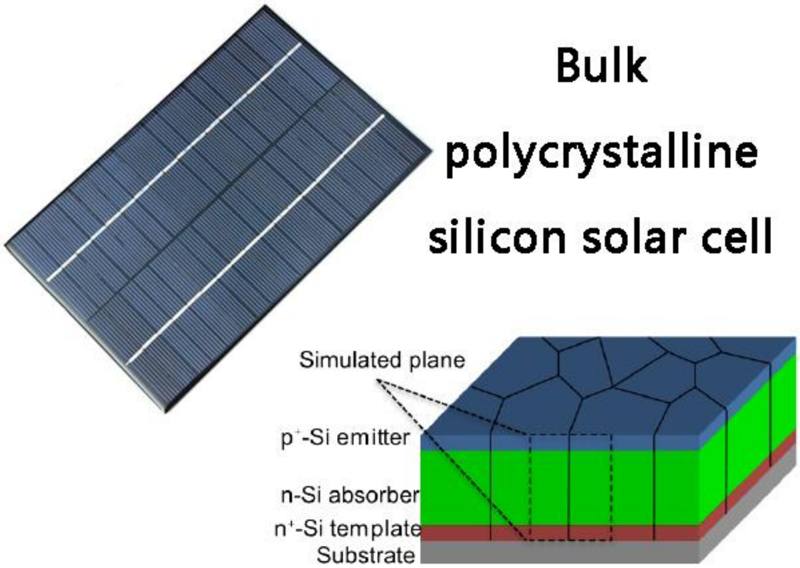

Figure I 3: Polycrystalline Silicon Solar Cell

Rigid crystalline silicon cells are commonly found in commercial installations, solar farms, and residential rooftops. They are the industry standard for solar energy systems globally because, as a result of decades of development, they provide a solid balance between efficiency, cost, and dependability.

I.4.2 Thin-film solar cells

They are produced by applying thin coatings of photovoltaic material on a substrate, such as metal, plastic, or glass. For portable and building-integrated applications, they are perfect since they are more flexible and lighter than conventional silicon cells[9] .

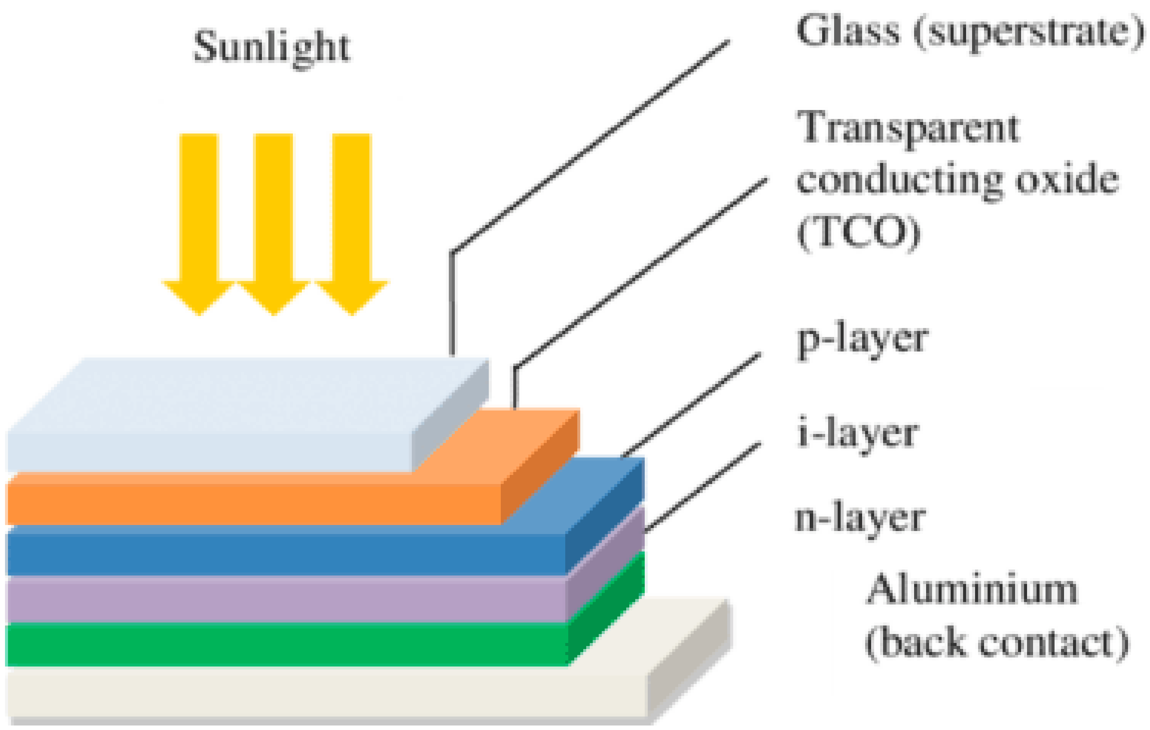

Figure I 4 : Polycrystalline Silicon Solar Cell

Amorphous silicon (a-Si), copper indium gallium selenide (CIGS), and cadmium telluride (CdTe) are the three primary varieties. The most popular is CdTe, which is inexpensive and has good efficiency despite cadmium's toxicity. Although more costly, CIGS provides greater flexibility and efficiency. Although amorphous silicon is flexible and less expensive, it is less effective. Although thin-film cells are less efficient than crystalline silicon, their versatility and portability make them appealing for specialized applications where low weight or flexibility are crucial [9], [10].

I.4.2.1 Substrate layer

All other layers in thin-film solar cells are mechanically supported by the substrate layer. It may be composed of metal, plastic, or glass. Flexible plastic substrates allow for lightweight, bending solar panels that can be used for portable electronics, curved surfaces, or integrated photovoltaic systems in buildings. The selection of the substrate has an impact on overall application flexibility, weight, and durability [9].

I.4.2.2 Transparent conductive layer

In thin-film solar cells, the transparent conductive layer (TCO) performs two essential tasks: it carries the electrical current produced and lets sunlight through to the absorber layer. It ought to be electrically conductive and extremely transparent. Fluorine-doped tin oxide (FTO) and indium tin oxide (ITO) are common materials that have good optical and electrical qualities [10], [11].

Thin-film solar cells frequently use a CdS window layer. Nevertheless, it has a number of disadvantages, including cadmium toxicity, conduction band misalignment with wide band gap chalcopyrite materials, and absorption losses. Because of these factors, a transparent conductive oxide (TCO) layer has taken the place of CdS [10]. These TCO layers must have a conductivity greater than $10^3\ \Omega^{-1}\cdot cm^{-1}$ and a light transmittance greater than 80% in the solar spectrum in order to be successful. Usually, SnO_2, InO_3, their alloy ITO, or ZnO thin films are used to obtain these characteristics.While these layers' optical transparency is correlated with the band gap value, their electrical performance is determined by their composition and doping. To serve as an insulator, a non-doped ZnO layer is typically deposited first, and then a doped ZnO:Al (aluminum-doped ZnO) or ITO layer. Between the absorber and the top contact, current leakage is stopped by the intrinsic ZnO layer.

I.4.2.3 Absorber layer

The most important component of a thin-film solar cell is the absorber layer, which is in charge of absorbing sunlight and producing electron-hole pairs via the photovoltaic effect. The performance and efficiency of the cell are determined by its substance. Amorphous silicon (a-Si), copper indium gallium selenide (CIGS), and cadmium telluride (CdTe) are common absorber materials that each have special benefits in terms of cost, flexibility, and light absorption [10].

The substance used to make the absorber layer needs to have a high visible spectrum absorption coefficient. The ideal direct band gap for this material would be between 1.1 and 1.7 eV. Usually, its p-type conductivity falls between 1 and $10^{-2}\ \Omega^{-1}\cdot cm^{-1}$. Silicon (Si), cadmium telluride (CdTe), copper indium selenide ($CuInSe_2$), copper indium aluminum selenide ($Cu(In,Al)Se_2$), and copper zinc tin sulfide (Cu_2ZnSnS_4) are the most often utilized absorber materials.

I.4.2.4 Buffer layer

The buffer layer in thin-film solar cells shields the layer junction and enhances charge separation. Zinc sulfide (ZnS) and cadmium sulfide (CdS) are common compounds that improve efficiency and lower energy loss [12].

I.4.2.5 Back contact layer

In thin-film solar cells, the rear contact layer completes the electrical circuit by gathering electrons. In order to ensure effective charge flow and overall cell efficiency, it is usually composed of conductive metals like aluminum or molybdenum [13].

I.4.3 Emerging solar cells

Perovskites and organic compounds are examples of innovative materials used in emerging solar cells to increase flexibility and efficiency. Compared to conventional silicon-based cells, they provide lightweight, inexpensive alternatives, but they have stability and commercial scaling issues [14], [15].

I.4.3.1 Perovskite solar cells

The efficiency of perovskite solar cells, a new technology, is increasing quickly; in lab settings, it can reach 25%. They are promise for future solar energy since they use inexpensive, adjustable materials [16]. There are still issues, though, such as stability issues and the hazardous lead present in many formulations.

I.4.3.2 Organic photovoltaic (OPV) solar cells

Carbon-based compounds are used by organic photovoltaic (OPV) solar cells to transform sunlight into electrical power. They are perfect for wearable technology and portable gadgets since they are flexible, lightweight, and affordable to make. Small-molecule OPVs and polymer-fullerene blends are two examples. However, as compared to silicon-based solar cells, OPVs usually have shorter lifespans and poorer efficiency (5–13%) [17], [18].

I.4.4 Quantum dot solar cells

These solar cell types have the potential to be extremely efficient and are a developing technology. However, due to their intricate production process, they are primarily in the research and development stages and have limited commercial availability [19].

I.4.5 Multi-Junction and tandem solar cells

Comprise multiple layers, each of which is intended to absorb distinct portions of the sun's spectrum, greatly increasing their effectiveness, which in lab settings can reach 40–47%. These cells are mostly utilized in specialist domains like aerospace and cutting-edge scientific research rather than in daily applications due to their complexity and expense [20], [21], [22].

I.5 Illumination

Electromagnetic radiation from sunlight is composed of photons that move freely and unhindered through space. But as soon as sunlight reaches the Earth's atmosphere, it reacts with dust, water vapor, air molecules, and other particles. As sunlight travels through the atmosphere and approaches the surface, these interactions result in a decrease in its energy. Scientists employ the idea of Air Mass to quantify and characterize this decrease in solar energy [23]. This item helps to measure how much the atmosphere reduces the amount of sunlight that reaches the earth by showing the relative distance that sunlight travels through the atmosphere as opposed to the shortest path that would be achievable when the sun is directly overhead.

I.5.1 Air Mass (AM)

The amount of atmosphere that sunlight must travel through before reaching a surface is known as air mass, or AM. It is a standard for testing solar panels and other solar technologies by simulating actual solar conditions.[24], [25]

The following formula can be used to define air mass

$$\mathbf{AM = 1 / \cos\theta} \qquad \text{(I.1)}$$

Where:

- AM is Air Mass and θ is the solar incidence angle

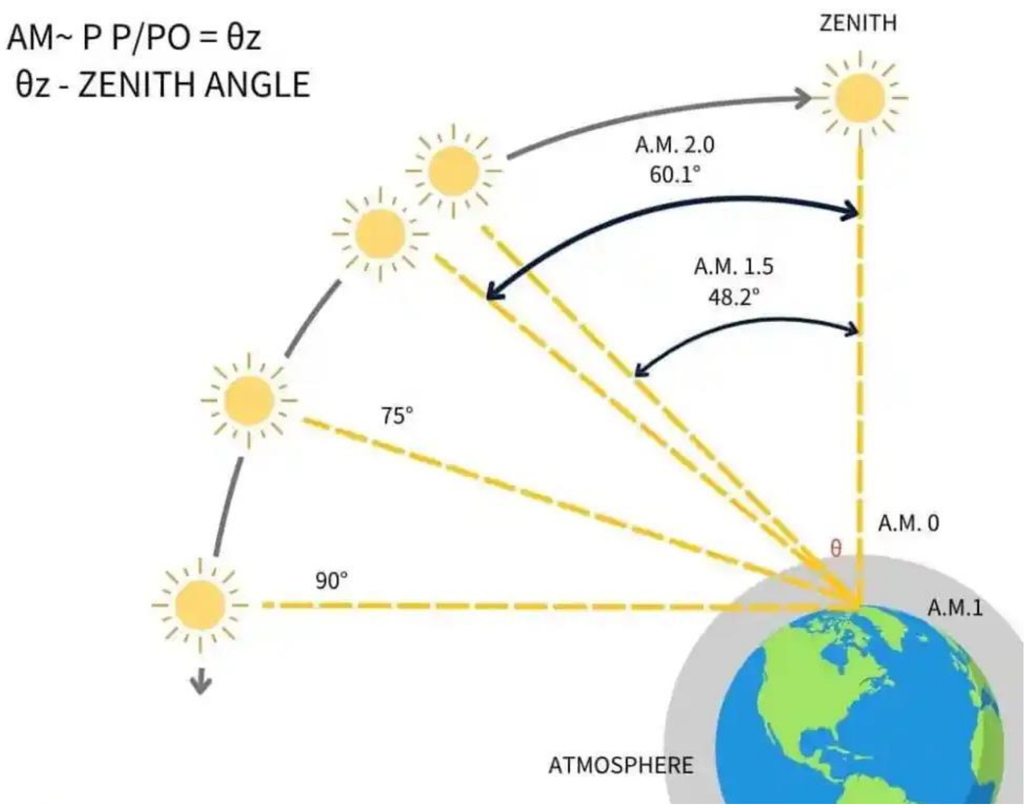

Figure I.5: Air mass factor values

As solar radiation travels through Earth's atmosphere, it is attenuated by a number of processes. Air mass, or the volume of atmosphere sunlight must pass through, is one important component. More energy is lost because the radiation travels a longer journey when the sun is lower in the sky and the air mass increases. The angle formed by sunlight and the horizontal surface is known as the solar incidence angle, and it is another crucial component.

Sunlight loses intensity as it passes through more atmosphere at a greater angle. Another important factor is the makeup of the atmosphere; certain gases absorb particular wavelengths. For example, water vapor absorbs infrared radiation, influencing the energy that reaches the surface, while the ozone layer filters UV rays.

I.5 .1.1 AM0 Space Conditions

Corresponds to the measurement of the solar spectrum in space, where the atmosphere of Earth has not yet allowed sunlight to reach the planet. Usually approximately 1361 W/m^2, it indicates the maximum solar irradiation because there is no air obstruction. The performance of solar technology intended for space, like those on satellites or spacecraft, is mostly evaluated using this standard. It provides a clear, unobstructed view of solar radiation over the entire spectrum without air absorption or scattering effects, making it a reference point for space-based solar cell testing.[26].

I.5 .1.2 AM1.5 – Terrestrial Standard

Sunlight that has passed through around 1.5 times the Earth's atmosphere is referred to as AM1.5. This usually happens when the sun is angled at a 42° angle from directly overhead. It is frequently used to assess how well solar panels work under realistic ground-level circumstances, particularly in mid-latitude regions. This standard is perfect for photovoltaic device certification and laboratory testing because it offers an average sun irradiation of about 1000 W/m². By mimicking the conditions often found during Earth's daily sun exposure, it guarantees uniformity and comparability across various solar technologies.

I.5 .1.3 AM1.5G Global Tilt Standard

The standard solar spectrum known as AM1.5G, or Air Mass 1.5 Global, is used to replicate the circumstances of normal sunlight on Earth. The letter "G" stands for "global radiation," which encompasses both direct sunlight and light that is dispersed by the atmosphere. Flat-plate solar panels inclined at an angle of around 37°, which is an average installation configuration, are frequently tested using this spectrum. AM1.5G offers a practical and reliable reference for assessing and contrasting the effectiveness of solar panels in a variety of geographical regions and climates with an average irradiance of 1000 W/m² during regular daylight hours [27].

I.6 Characteristics of a solar cell

A solar cell's performance is determined by a number of important factors. The maximum voltage that the cell can generate in the absence of any current is known as the open-circuit voltage (Voc). On the other hand, the current at zero voltage is known as the short-circuit current (Isc). When assessing output, the Pmax—the moment at which the cell provides its maximum power—is essential. The cell quality is indicated by the fill factor (FF), which is computed using Pmax, Voc, and Isc. The cell's ability to convert sunlight into electrical energy is measured by its conversion efficiency. The temperature coefficient is also significant since temperature can affect output. The spectral response of a solar cell demonstrates how it responds to various light wavelengths. Finally, internal resistances might affect overall efficiency and energy loss.

I.6.1 Open-circuit voltage (Voc)

The greatest voltage that a solar cell can generate when there is no current flowing—basically, when the circuit is open—is known as the open-circuit voltage, or Voc. It displays the potential difference between the terminals of the cell when there is no load but light present. Temperature, light intensity, and material all affect Voc. Although Voc values are only one aspect of assessing a solar cell's overall efficiency, they often suggest superior photovoltaic performance.

I.6.2 Short-circuit current (Isc)

The highest current that a solar cell can produce when its output terminals are connected directly—that is, when the voltage is zero is known as the Isc. It shows how many charge carriers, or electrons, are produced by light and gathered by the cell. Isc is mostly influenced by the surface area of the cell and the strength of the sun. Better light absorption and charge collection are usually indicated by a greater Isc, which enhances the cell's overall power output.

I.6 .3 Maximum power (Pmax)

The maximum electrical power a solar cell can generate under typical test settings is known as its Pmax. The maximum power point (MPP), a certain voltage and current combination, is where it happens. At this moment, Pmax is determined by multiplying the voltage by the current:

$$Pmax = \mathrm{Vm} \times \mathrm{Im} \qquad (I.2)$$

This amount is used to calculate the cell's overall energy conversion efficiency and represents its actual performance.

I.6.4 Fill factor FF

Is an essential measure used to assess a solar cell's quality. It is the ratio of the open-circuit voltage (Voc) to the product of the short-circuit current (Isc) and the maximum power (Pmax).

$$FF = \frac{Pm}{Isc \times Vco} \qquad \text{(I.3)}$$

A greater FF signifies improved performance and reduced internal losses, demonstrating how well the cell transforms sunlight into useful electricity.

I.6.5 Efficiency η

A solar cell's efficiency (η) is the proportion of sunlight that is transformed into electrical energy. It is computed by dividing the incident solar power by the highest power output (Pmax). Under normal circumstances, more power may be produced from the same quantity of sunlight due to higher efficiency, which translates into improved performancev[28]

$$\eta = \frac{Pm}{A \times Pi} = \frac{Isc \times Vco \times FF}{A \times Pi} \qquad \text{(I.4)}$$

The performance of a solar cell is determined by the associated factors Voc, Isc, Pmax, FF, and efficiency. Pmax denotes the maximum power output, whilst Voc and Isc establish the limitations for voltage and current. How well Pmax is retrieved from Voc and Isc is indicated by the fill factor. Efficiency shows the conversion of sunlight into electricity by combining all the components. When combined, these figures aid in solar cell comparison, design optimization, loss understanding, and energy yield enhancement, making them essential for creating efficient solar technologies.

I.7 Semiconductors

Semiconductors are unique substances that, in specific circumstances, conduct electricity, which makes them perfect for managing electrical impulses. Semiconductors have the ability to transition between conducting and insulating states, in contrast to metals, which are always good conductors. Doping is the process of adding trace amounts of other elements to silicon, a common semiconductor, to increase its conductivity

As a result, two varieties are produced: n-type, which has excess electrons, and p-type, which has electron vacancies. A p-n junction, which is essential in electronic devices, is created when they combine. Electricity is produced in solar cells by semiconductors that absorb sunlight and discharge energized electrons. They are crucial components of electronics, ranging from computers and phones to renewable energy systems like photovoltaic panels, because of their capacity to react to changes in light, heat, or voltage [29].

I.7.1 Intrinsic semiconductors

Pure semiconductor materials devoid of deliberate doping are known as intrinsic semiconductors. The most prevalent examples are silicon (Si) and germanium (Ge). Each atom in their crystalline structure forms stable covalent bonds with its neighbors by sharing electrons in their natural state. Intrinsic semiconductors exhibit insulator behavior at absolute zero. But when the temperature rises, some electrons acquire sufficient energy to escape their connections, creating "holes"voids.

When an electric field is applied, these liberated electrons and holes flow through the material as charge carriers, enabling electrical conduction. The number of electrons and holes in intrinsic semiconductors is the same. Intrinsic semiconductors serve as the foundation for more sophisticated materials utilized in electrical and optoelectronic devices following doping, despite their comparatively low conductivity. [30].

I.7.2 Extrinsic semiconductors

Materials whose electrical characteristics have been improved by doping—the addition of trace amounts of impurities are known as extrinsic semiconductors. Two varieties are therefore produced: n-type, in which phosphorus and other elements contribute extra electrons, and p-type, in which boron and other elements produce electron "holes."

When compared to intrinsic (pure) semiconductors, these charge carriers greatly increase the material's conductivity. To regulate current flow, the electron-hole balance is purposefully changed. Since they serve as the foundation for parts like diodes, transistors, and solar cells utilized in a variety of digital and energy devices, extrinsic semiconductors are crucial to modern electronics[31], [32].

I.7.3 Semiconductors generations

I.7.3.1 First-Generation Semiconductor Material

Pure, elemental semiconductors such as silicon (Si) and germanium (Ge) are considered first-generation semiconductor materials. Because of their inherent semiconducting qualities, they served as the cornerstone of early electronics and were mostly employed in simple devices like transistors and diodes[33].

a. **Properties**:

- plentiful, stable, and simple to cleanse. 1.1 eV is the indirect bandgap.

- crystalline solid having a lattice of diamonds. crystalline solid having a lattice of diamonds.

- modest electrical conductivity that gets better with doping.

- creates a solid and dependable p-n connection.

b. **Applications**:

Diodes, transistors, and integrated circuits are widely employed in both early and contemporary electronic equipment. The fundamental component of the majority of solar cells and microchips.

I.7.3.2 Second-generation semiconductor

Compound semiconductors, such as gallium arsenide (GaAs), indium phosphide (InP), and cadmium telluride (CdTe), are second-generation semiconductor materials. These materials are usually created by combining two or more elements. Compared to first-generation materials, these materials have more electron mobility and operate better at high frequencies and temperatures.They are especially helpful in optoelectronic applications like as LEDs, laser diodes, and high-speed communication devices due to their straight bandgaps. Faster and more effective electronic components were made possible by second-generation semiconductors, which increased the potential of contemporary technology, particularly in the areas of enhanced solar cells, infrared detectors, and telecommunications.

a. Properties:

Direct bandgap, perfect for optoelectronic applications; Higher electron mobility than silicon, allowing for faster operation.. Works better at high temperatures and high frequencies.

b. Applications:

- utilized in high-speed devices such as radio-frequency circuits and microwave transistors..

- essential component for solar cells, laser diodes, and light-emitting diodes (LEDs).

- crucial for fiber-optic communication systems and space technology

I.7.3.3 Third-generation semiconductors

Third-generation semiconductors are advanced wide bandgap semiconductors, characterized by their higher breakdown voltages, higher thermal stability, and greater efficiency at high frequencies and temperatures compared to first and second-generation semiconductors [34].

Third-generation semiconductors include silicon carbide (SiC), which is perfect for power electronics, electric cars, and energy-efficient systems because of its excellent temperature and voltage tolerance. Higher electron mobility makes gallium nitride (GaN) a popular choice for high-power devices including power supplies, LED illumination, and radio frequency amplifiers. Zinc oxide (ZnO), which is used in high-power devices such UV LEDs and transistors as well as optoelectronics, is another example.

a. Properties:

It is appropriate for high-temperature applications due to its high stability and thermal conductivity. high breakdown voltage that makes it possible to operate in high-power settings. Outstanding power conversion and energy system efficiency.

b. Applications:

utilized in power electronics, including electric vehicle (EV) power supplies and inverters.

-A key component of energy-efficient systems, such as electric grids and solar inverters.

-Important in high-voltage, high-temperature applications such as the automotive and aerospace sectors.

I.7.4 Semiconductor structure types

I.7.4 .1 Single-junction solar cells

Possess a simple semiconductor structure with a single active layer that generates energy from sunlight. A semiconductor material, such as crystalline silicon, is commonly used to create this active layer. Its bandgap dictates the portion of sunlight it can absorb.[35].

A p-n junction, which is created by joining a p-type and an n-type semiconductor, is typically a part of the structure. Electrons in the semiconductor are excited when sunlight strikes the cell, forming electron-hole pairs. An electric current is created when these are separated by the electric field at theintersection. Single-junction cells have a theoretical efficiency limit of about 33% because of energy losses from unused photons and heat, despite being easier and less expensive to construct than multijunction cells. Due to their affordability and dependability, they are extensively utilized in portable solar, business, and residential settings.

I.7.4 .2 Bifacial solar cells

They are cutting-edge photovoltaic systems that use sunlight absorbed on both the front and back surfaces to create electricity. The back side makes use of reflected or dispersed light from the ground or nearby surfaces, while the front side absorbs direct sunlight. They can generate more energy than traditional single-sided panels because of its dual-sided absorption.[36]

They are frequently constructed with a translucent back sheet or glass on both sides to allow light to enter and reach the back cell layer. Monocrystalline silicon is frequently the basis for bifacial technology, which works best in locations with reflecting surfaces like sand or snow or in installations that are higher up. Their higher energy output and efficiency might provide greater long-term performance and returns, despite the fact that they are usually more expensive.

I.7.4.3 Superstrate solar cells

They are a kind of photovoltaic device in which light enters through the superstrate, the uppermost supporting layer, and then travels down to the active solar layers. Thin-film technologies like perovskite solar cells, cadmium telluride (CdTe), and amorphous silicon (a-Si) frequently have this structure.[37].

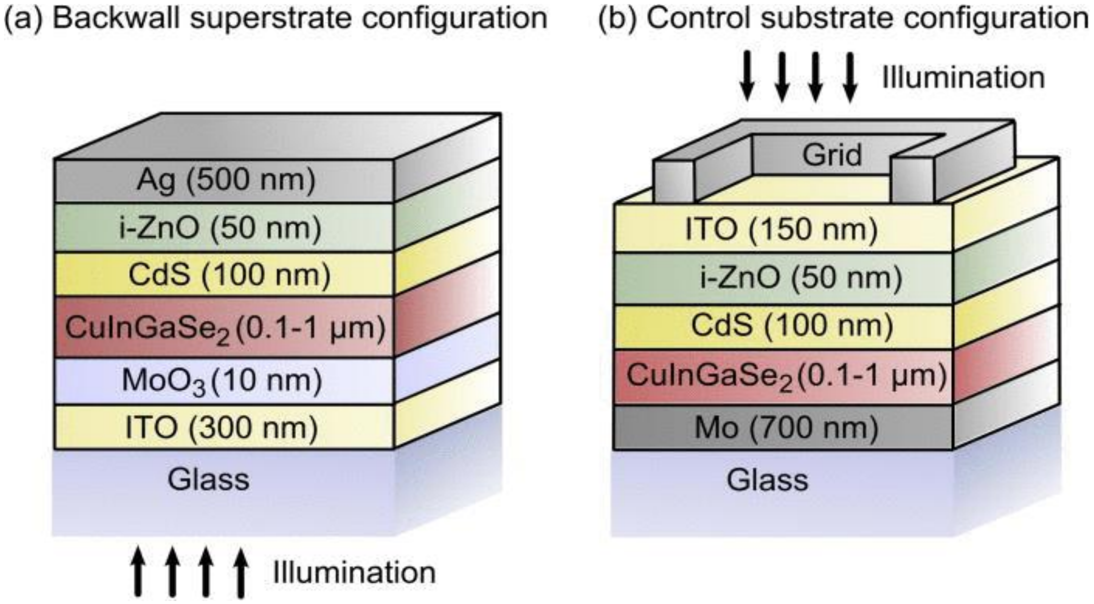

Figure I 6: Superstrate solar cells

The transparent superstrate, which is frequently composed of glass, functions both a light-entry point and a mechanical support in this design. Below the superstrate, the active layers—such as the electrodes and absorber—are deposited, and on the back, the electrical contacts are made. Superstrate arrangements, which are frequently utilized in portable solar technologies and building-integrated photovoltaics (BIPV), are perfect for applications that need for lightweight and flexible designs. In fixed-position solar systems, this construction improves endurance, streamlines production, and enables effective light collecting.

I.7.4.4 Tandem solar cells

Advanced photovoltaic devices known as tandem solar cells combine several semiconductor layers, each of which is intended to absorb a distinct portion of the sun's spectrum. Tandem cells employ two or more sub-cells stacked on top of one another, in contrast to single-junction cells, which have a narrow bandgap and can only effectively exploit a part of sunlight. A distinct semiconductor material with a bandgap designed to absorb high-, medium-, or low-energy photons makes up each sub-cell [38].

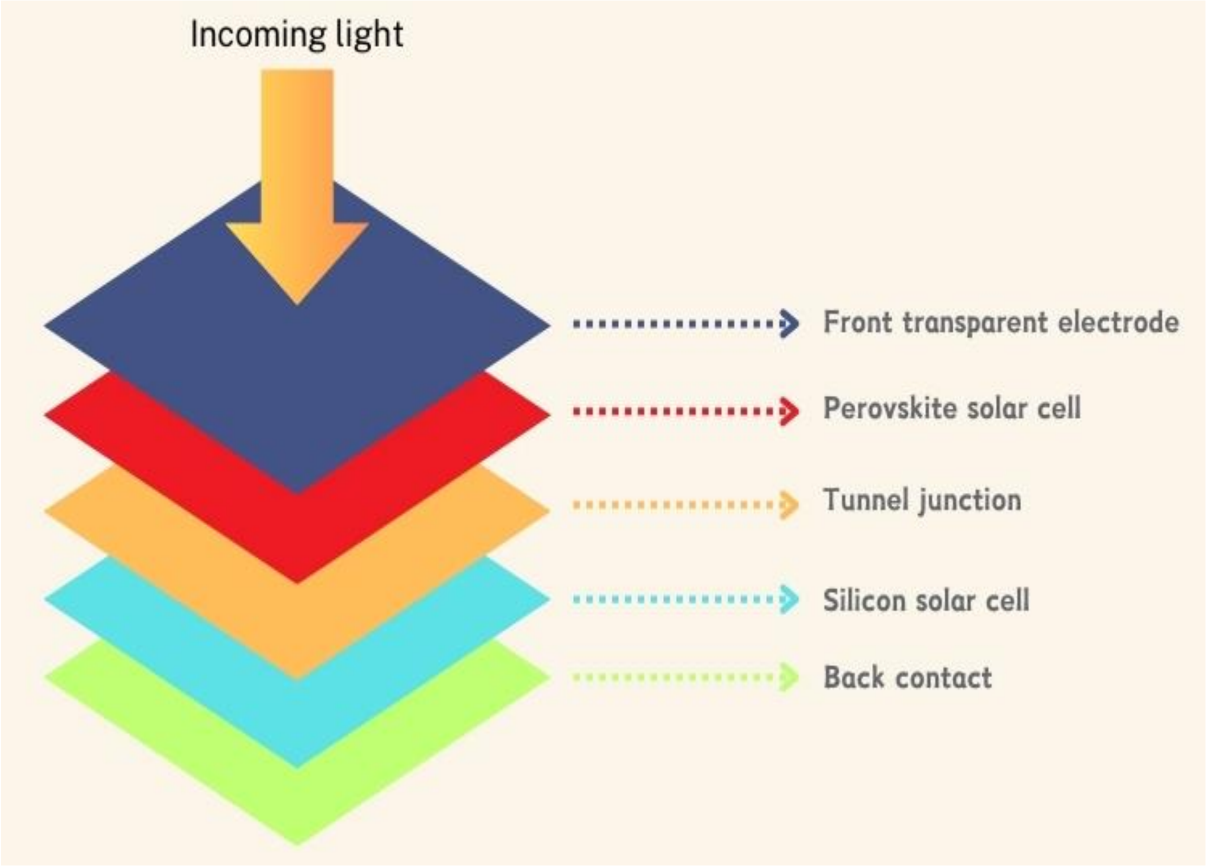

Figure I.7: Tandem solar cells

The bottom cells absorb the remaining lower-energy light, whereas the top cell absorbs high-energy light (short wavelengths). An interlayer or tunnel junction connects these layers, facilitating effective charge transfer between them.

I.7.4.5 Triple-junction solar cells

Three distinct semiconductor layers are used in this kind of multijunction photovoltaic system, each of which is intended to absorb a certain range of the sun's spectrum. Since each of these vertically stacked layers has a unique bandgap, the cell can absorb high-, medium-, and low-energy photons more effectively than single-junction cells [39].

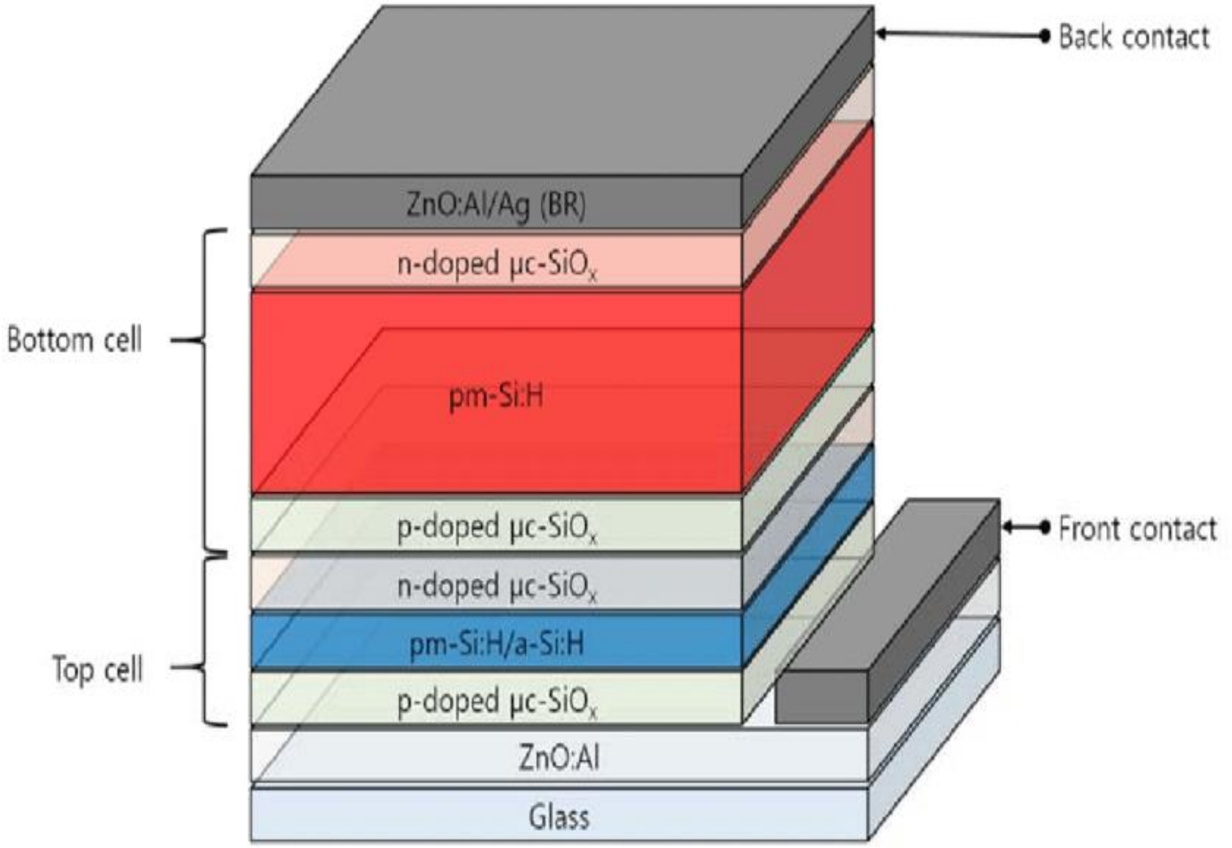

Figure I 8: Multi-junction solar cells

High-energy (short-wavelength) light is usually absorbed by the top cell, mid-range light is captured by the middle cell, and low-energy (long-wavelength) light is collected by the bottom cell. Typically, tunnel junctions connect these layers, allowing electrons to flow freely between them with little energy loss. The materials GaInP (top), GaAs (middle), and Ge (bottom) are frequently utilized. Triple-junction cells are particularly useful in space technology and concentrated photovoltaic systems where performance is crucial because of their structure, which allows them to achieve efficiencies exceeding 35%.

I.8 Solar Cells Based on Copper

One significant class of thin-film photovoltaic devices is copper-based solar cells, which combine inexpensive materials with decent efficiency. $Cu(In,Ga)Se_2$ (CIGS), $CuInSe_2$ (CIS), $Cu_2ZnSn(S,Se)_4$ (CZTSSe), and $CuIn(S,Se)_2$ (CISS) are the most well-known absorbers that contain copper. These substances are part of the chalcopyrite and kesterite material family, which is distinguished by their intense light absorption and modifiable band gaps..[40], [41], [42], [43]

Because it improves carrier collection and contributes to p-type conductivity, copper is essential to these structures. For instance, in laboratory conditions, CIGS solar cells can achieve efficiencies of more than 22%. Although it usually exhibits lower efficiencies because of defect-related recombination, CZTSSe, an option that is devoid of cadmium and indium, uses plentiful elements (Cu, Zn, Sn, S, Se), and is more environmentally friendly. To improve the efficiency and scalability of copper-based solar cells, ongoing research attempts to regulate defect chemistry, grain boundaries, and interface quality.

In a study of A. Díaz-Loera et all.[44] used the Solar Cell Capacitance Simulator (SCAPS-1D) to simulate $CuIn(S_x,Se_{1-x})_2$ thin-film solar cells over the entire composition range of $x = 0$ to $x = 1$. A $CuInSe_2$ substrate design served as the basis for the modeling, and the methodology was verified by contrasting it with experimental data from published works. The authors examined defect densities in the absorber layer, optimized layer thicknesses, and computed the absorption coefficients for $CuInSe_2$ and $CuInS_2$. The best composition for the highest solar cell efficiency was found at $x = 0.5$, according to J-V curve results, suggesting that a balanced sulfur/selenium ratio improves device performance.

C. J. Sheppard and V. Alberts [45] investigated a promising industrial process for creating photovoltaic absorbers: the creation of $CuIn(Se,S)_2$ chalcopyrite absorber layers utilizing dc sputtered CuIn metallic alloys, followed by exposure to a reactive $H_2Se/Ar/H_2S$ environment. Despite its benefits, this method frequently causes $CuInSe_2$ and $CuInS_2$ to phase separate during high-temperature treatment, which limits bandgap adjustment and prevents the creation of a homogenous alloy. Reaching open-circuit voltages above 600 mV, which are essential for high-performance solar modules, is adversely affected by this phase inhomogeneity. In order to overcome these constraints and possibly increase the efficiency of solar cells, the study offers an alternate two-stage deposition technique that makes it possible to fabricate homogenous, single-phase $CuIn(Se,S)_2$ alloys.

C. J. Sheppard, V. Alberts, and J. R. Botha [46] explored ways to improve the $CuInSe_2/CdS/ZnO$ solar cells' conversion efficiency, which is constrained by the material's narrow band gap (~1.0 eV). The absorber's band gap needs to be raised to about 1.2 eV in order to increase efficiency. This can be done by partially substituting another group III element for indium (In) and/or group VI elements like sulfur (S) for selenium (Se). A greater band gap results from lattice contraction brought on by these replacements. Conventional two-step growth methods, which expose metallic precursors to Se and/or S gasses, make uniform substitution difficult to achieve. The authors show how a new two-step deposition technique can produce homogenous, single-phase $CuIn(Se,S)_2$ films with enhanced optical and structural properties, which could result in increased solar performance.

An-Yu Zhu et all [47]used nonadiabatic molecular dynamics simulations and density functional theory to investigate the effects of the Cu–Zn cation disorder in kesterite $CuZnSn(S_{1-x}Se_x)_4$ solar cells. According to their findings, disorder that affects more than one atomic plane—specifically, the Cu–Sn and Cu–Zn planes—is substantially more detrimental to solar cell performance than disorder that just affects the Cu–Zn planes. Sn–S/Se bonds elongate as a result of this cross-plane disorder, which lowers the conduction band minimum, narrows the band gap, and decreases optical absorption. By improving electron-vibrational coupling, it also shortens charge carrier lifetimes and speeds up nonradiative recombination. The work gives recommendations for improving material design in kesterite-based photovoltaic applications as well as theoretical support for the impact of Cu–Zn disorder on device efficiency.

In a study was published by Duan W. J et all [48] , Metal chlorides and chalcogen sources in ethanolamine have been employed in a solvothermal process to create $CuIn(S_xSe_{1-x})_2$ nanoparticles with compositions varying from $x = 0$ to 1. Chalcopyrite was shown to be the predominant phase by XRD analysis, and when $x > 0.5$, a secondary wurtzite phase appeared. As the sulfur level rose, FESEM showed a morphological change from flake-like to particulate forms. A progressive blue shift in the absorption edge was seen by UV-Vis spectroscopy, which corresponded to an increase in the band gap from 1.16 to 1.48 eV. These results show that sulfur/selenium composition adjustment can be used to tune both structural and optical characteristics.

Solange Temgoua, Romain Bodeux, Negar Naghavi, and Sébastien Delbos [49] examined how the crystallization of $Cu_2ZnSn(S_xSe_{1-x})_4$ (CZTSSe) thin-film absorbers was affected by the annealing conditions. Co-sputtering was used to deposit the Cu–Zn–Sn–S precursor layers onto glass substrates covered with Mo. The researchers investigated how the structural and compositional qualities changed by altering the annealing temperature (300–600 °C) and time (1–60 minutes). They found that extended annealing times and higher temperatures improved the crystallization of both undesirable $SnSe_2$ phases and CZTSSe. The coexistence of $SnSe_2$ consistently resulted in performance reduction because of shunt routes, which decreased the open-circuit voltage and fill factor, even if solar cell efficiencies of up to 7% were attained under ideal circumstances. In order to reduce harmful secondary phases and improve the performance of CZTSSe solar cells, the study highlights the necessity of carefully controlling annealing settings..

Zuoyun Wang and colleagues [50] created a synergistic strategy to improve the open-circuit voltage (VOC) and fill factor (FF) of $Cu_2ZnSn(S,Se)_4$ (CZTSSe) solar cells without lowering the short-circuit current density (JSC). Their technique combines surface treatment of $(NH_4)_3S$ with atomic layer deposition (ALD) of Al_2O_3. This method eliminates undesirable Zn- and Sn-related impurities, improves crystallinity, transforms deep-level CuZn defects into shallower VCu defects, and adds sulfur to the absorber surface. These changes result in more effective charge collection by extending minority carrier lifetimes, reducing recombination losses, and expanding the depletion region. Consequently, the efficiency rises to 13.0%, the FF rises from 64.2% to 69.7%, and the VOC deficit decreases from 0.607 V to 0.547 V.

I.9 Conclusion

In conclusion, this chapter has provided a comprehensive foundation on solar energy and photovoltaic technologies, with a particular emphasis on thin-film solar cells and copper-based semiconductor materials. It detailed the structural, optical, and electronic properties that are critical for device performance. Moreover, it presented advanced modeling approaches that integrate first-principles calculations with device-level simulations through SCAPS-1D. The insights gained herein establish a robust framework for the experimental investigations and optimization strategies that will be elaborated upon in the subsequent chapters. Ultimately, the advancement of photovoltaic research relies on such interdisciplinary approaches that bridge fundamental theory and practical engineering, thus paving the way for innovative and efficient solar energy solutions.

References

[1] N. S. M. N. Izam, Z. Itam, W. L. Sing, and A. Syamsir, “Sustainable Development Perspectives of Solar Energy Technologies with Focus on Solar Photovoltaic—A Review,” 2022. doi: 10.3390/en15082790.

[2] C. J. Rhodes, “Solar energy: Principles and possibilities,” *Sci Prog*, vol. 93, no. 1, 2010, doi: 10.3184/003685010X12626410325807.

[3] H. P. Wang, D. Periyanagounder, A. C. Li, and J. H. He, “Fabrication of Silicon Hierarchical Structures for Solar Cell Applications,” *IEEE Access*, vol. 7, 2019, doi: 10.1109/ACCESS.2018.2885169.

[4] “Solar cells—Operating principles, technology and system applications,” *Solar Energy*, vol. 28, no. 5, 1982, doi: 10.1016/0038-092x(82)90265-1.

[5] A. F. Dyadenchuk and R. I. Oleksenko, “Simulation photoconverters of porous-Si/Si with different anti-reflective coatings,” *International Journal of Mathematics and Physics*, vol. 14, no. 2, 2023, doi: 10.26577/ijmph.2023.v14.i2.010.

[6] C. Platzer-Björkman *et al.*, “Back and front contacts in kesterite solar cells: State-of-the-art and open questions,” *JPhys Energy*, vol. 1, no. 4, 2019, doi: 10.1088/2515-7655/ab3708.

[7] S. Qiao, J. Liu, G. Fu, and S. Wang, “Research progress on lateral photovoltaic effect in solar cell structural materials,” 2020. doi: 10.1360/TB-2020-0416.

[8] A. Mohammad Bagher, “Types of Solar Cells and Application,” *American Journal of Optics and Photonics*, vol. 3, no. 5, 2015, doi: 10.11648/j.ajop.20150305.17.

[9] K. ElKhamisy, H. Abdelhamid, E. S. M. El-Rabaie, and N. Abdel-Salam, “A Comprehensive Survey of Silicon Thin-film Solar Cell: Challenges and Novel Trends,” 2024. doi: 10.1007/s11468-023-01905-x.

[10] K. L. Chopra, P. D. Paulson, and V. Dutta, “Thin-film solar cells: An overview,” *Progress in Photovoltaics: Research and Applications*, vol. 12, no. 2–3, 2004, doi: 10.1002/pip.541.

[11] G. V. Kaliyannan, R. Gunasekaran, S. Sivaraj, S. Jaganathan, and R. Rathanasamy, “Thin-Film Solar Cells,” in *Fundamentals of Solar Cell Design*, 2023. doi: 10.1002/9781119725022.ch4.

[12] Mamta, K. K. Maurya, and V. N. Singh, “Enhancing the performance of an sb2se3-based solar cell by dual buffer layer,” *Sustainability (Switzerland)*, vol. 13, no. 21, 2021, doi: 10.3390/su132112320.

[13] B. Zhou *et al.*, “Application of bromide-iodide lead perovskite thin film as a copper-free back contact layer for CdTe solar cells,” *Solar Energy*, vol. 230, 2021, doi: 10.1016/j.solener.2021.11.005.

[14] M. Cellura, L. Q. Luu, F. Guarino, and S. Longo, "A review on life cycle environmental impacts of emerging solar cells," 2024. doi: 10.1016/j.scitotenv.2023.168019.

[15] A. Wibowo *et al.*, "ZnO nanostructured materials for emerging solar cell applications," 2020. doi: 10.1039/d0ra07689a.

[16] N. Suresh Kumar and K. Chandra Babu Naidu, "A review on perovskite solar cells (PSCs), materials and applications," *Journal of Materiomics*, vol. 7, no. 5, 2021, doi: 10.1016/j.jmat.2021.04.002.

[17] S. Lizin, S. Van Passel, E. De Schepper, and L. Vranken, "The future of organic photovoltaic solar cells as a direct power source for consumer electronics," *Solar Energy Materials and Solar Cells*, vol. 103, 2012, doi: 10.1016/j.solmat.2012.04.001.

[18] A. Dolara, S. Leva, G. Manzolini, R. Simonetti, and I. Trattenero, "Outdoor Performance of Organic Photovoltaics: Comparative Analysis," *Energies (Basel)*, vol. 15, no. 5, 2022, doi: 10.3390/en15051620.

[19] H. Anwar, I. Arif, U. Javeed, H. Mushtaq, K. Ali, and S. K. Sharma, "Quantum Dot Solar Cells," in *Solar Cells: From Materials to Device Technology*, 2020. doi: 10.1007/978-3-030-36354-3_9.

[20] A. W. Y. Ho-Baillie, J. Zheng, M. A. Mahmud, F. J. Ma, D. R. McKenzie, and M. A. Green, "Recent progress and future prospects of perovskite tandem solar cells," 2021. doi: 10.1063/5.0061483.

[21] F. E. Cherif and H. Sammouda, "Optoelectronic simulation and optimization of tandem and multi-junction perovskite solar cells using concentrating photovoltaic systems," *Energy Reports*, vol. 7, 2021, doi: 10.1016/j.egyr.2021.09.014.

[22] A. Hadipour, B. De Boer, and P. W. M. Blom, "Organic tandem and multi-junction solar cells," *Adv Funct Mater*, vol. 18, no. 2, 2008, doi: 10.1002/adfm.200700517.

[23] L. A. A. Bunthof, J. Bos-Coenraad, W. H. M. Corbeek, E. Vlieg, and J. J. Schermer, "The illumination angle dependency of CPV solar cell electrical performance," *Solar Energy*, vol. 144, 2017, doi: 10.1016/j.solener.2017.01.026.

[24] A. O. M. Maka and T. S. O'Donovan, "Analysis of thermal response and electrical characterisation of triple-junction solar cells based on variable solar spectral irradiance and air mass," *Thermal Science and Engineering Progress*, vol. 10, 2019, doi: 10.1016/j.tsep.2019.02.005.

[25] A. Guechi, M. Chegaar, and M. Aillerie, "Air mass effect on the performance of organic solar cells," in *Energy Procedia*, 2013. doi: 10.1016/j.egypro.2013.07.083.

[26] C. Baur, E. F. Lisbona, and J. R. González, "Air mass zero (AM0) studies and solar cell calibration," in *Photovoltaics for Space: Key Issues, Missions and Alternative Technologies*, 2022. doi: 10.1016/B978-0-12-823300-9.00008-X.

[27] P. Schygulla *et al.*, “Two-terminal III–V//Si triple-junction solar cell with power conversion efficiency of 35.9 % at AM1.5g,” *Progress in Photovoltaics: Research and Applications*, vol. 30, no. 8, 2022, doi: 10.1002/pip.3503.

[28] M. Minbashi, A. Ghobadi, M. H. Ehsani, H. Rezagholipour Dizaji, and N. Memarian, “Simulation of high efficiency SnS-based solar cells with SCAPS,” *Solar Energy*, vol. 176, 2018, doi: 10.1016/j.solener.2018.10.058.

[29] K. W. Böer and U. W. Pohl, *Semiconductor Physics*, vol. 1–2. 2023. doi: 10.1007/978-3-031-18286-0.

[30] Q. Li, Q. Chen, and B. Song, “Giant radiative thermal rectification using an intrinsic semiconductor film,” *Materials Today Physics*, vol. 23, 2022, doi: 10.1016/j.mtphys.2022.100632.

[31] N. Balkan and A. Erol, “Intrinsic and Extrinsic Semiconductors,” 2021. doi: 10.1007/978-3-319-44936-4_2.

[32] Z. Dilli, “Intrinsic and Extrinsic Semiconductors , Fermi-Dirac Distribution Function , the Fermi level and carrier concentrations Review : Charge Carriers in Semiconductors,” *Enee*, vol. 313, 2009.

[33] S. wu, “Optical Amplification Achieved in a First-Generation Dendritic Organic Semiconductor,” *MRS Bull*, vol. 29, no. 5, 2004, doi: 10.1557/mrs2004.86.

[34] Y. Chen *et al.*, “Review—Progress in Electrochemical Etching of Third-Generation Semiconductors,” *ECS Journal of Solid State Science and Technology*, vol. 12, no. 4, 2023, doi: 10.1149/2162-8777/acce03.

[35] K. Attari, L. Amhaimar, A. El Yaakoubi, A. Asselman, and M. Bassou, “The Design and Optimization of GaAs Single Solar Cells Using the Genetic Algorithm and Silvaco ATLAS,” *International Journal of Photoenergy*, vol. 2017, 2017, doi: 10.1155/2017/8269358.

[36] T. C. R. Russell, R. Saive, A. Augusto, S. G. Bowden, and H. A. Atwater, “The Influence of Spectral Albedo on Bifacial Solar Cells: A Theoretical and Experimental Study,” *IEEE J Photovolt*, vol. 7, no. 6, 2017, doi: 10.1109/JPHOTOV.2017.2756068.

[37] E. Peksu, C. Yener, C. G. Unlu, and H. Karaagac, “Exploring graphene’s potential as a transparent conductive layer in Cu2ZnSnS4 superstrate solar cells,” *J Alloys Compd*, vol. 976, 2024, doi: 10.1016/j.jallcom.2023.172979.

[38] M. Jošt, L. Kegelmann, L. Korte, and S. Albrecht, “Monolithic Perovskite Tandem Solar Cells: A Review of the Present Status and Advanced Characterization Methods Toward 30% Efficiency,” 2020. doi: 10.1002/aenm.201904102.

[39] J. Aulich *et al.*, “Spectrometric Characterization for Triple-Junction Solar Cells,” *Solar RRL*, vol. 8, no. 3, 2024, doi: 10.1002/solr.202300783.

[40] S. Amiri and S. Dehghani, “Design and Simulation of Single-Junction and Multi-junction Thin-Film Solar Cells Based on Copper Tin Sulfide,” *J Electron Mater*, vol. 49, no. 10, 2020, doi: 10.1007/s11664-020-08382-6.

[41] A. Nagata, T. Oku, T. Akiyama, and A. Suzuki, “Effects of Au nanoparticle addition to hole transfer layer in organic solar cells based on copper naphthalocyanine and fullerene,” *Progress in Natural Science: Materials International*, vol. 24, no. 3, 2014, doi: 10.1016/j.pnsc.2014.04.002.

[42] T. T. T Luong, Z. Chen, and H. Zhu, “Flexible solar cells based on copper phthalocyanine and buckminsterfullerene,” *Solar Energy Materials and Solar Cells*, vol. 94, no. 6, 2010, doi: 10.1016/j.solmat.2010.02.023.

[43] G. Wisz *et al.*, “Solar cells based on copper oxide and titanium dioxide prepared by reactive direct-current magnetron sputtering,” *Opto-Electronics Review*, vol. 29, no. 3, 2021, doi: 10.24425/opelre.2021.139039.

[44] A. Díaz-Loera, J. R. Ramos-Serrano, and M. E. Calixto, “Semiconducting CuIn(SX,Se1−X)2 thin-film solar cells modeling using SCAPS-1D,” *MRS Adv*, vol. 7, no. 2–3, 2022, doi: 10.1557/s43580-022-00231-4.

[45] C. J. Sheppard and V. Alberts, “Deposition of single-phase CuIn(Se,S)2 thin films from the sulfurization of selenized CuIn alloys,” *J Phys D Appl Phys*, vol. 39, no. 17, 2006, doi: 10.1088/0022-3727/39/17/008.

[46] C. J. Sheppard, V. Alberts, and J. R. Botha, “Structural and optical characterization of single-phase CuIn(Se,S) 2 thin films deposited using a two-step process,” in *Physica Status Solidi (C) Current Topics in Solid State Physics*, 2008. doi: 10.1002/pssc.200776837.

[47] A. Y. Zhu, R. X. Ding, H. T. Xu, C. J. Tong, and K. P. McKenna, “Cu-Zn Cation Disorder in Kesterite Cu2ZnSn(SxSe1-x)4 Solar Cells,” *ACS Energy Lett*, vol. 9, no. 2, 2024, doi: 10.1021/acsenergylett.3c02653.

[48] W. J. Duan, X. C. Duan, L. L. Li, H. Xia, and Y. Y. Zhu, “Microstructure and optical properties of CuIn (SxSe1-x)2 nanoparticles synthesized by solvothermal route,” *Fenmo Yejin Cailiao Kexue yu Gongcheng/Materials Science and Engineering of Powder Metallurgy*, vol. 20, no. 1, 2015.

[49] S. Temgoua, R. Bodeux, N. Naghavi, and S. Delbos, “Effects of SnSe2secondary phases on the efficiency of Cu2ZnSn(Sx,Se1 - X)4based solar cells,” in *Thin Solid Films*, 2015. doi: 10.1016/j.tsf.2014.10.058.

[50] Z. Wang *et al.*, “Toward High Efficient Cu2ZnSn(Sx,Se1−x)4 Solar Cells: Break the Limitations of VOC and FF,” *Small*, vol. 19, no. 22, 2023, doi: 10.1002/smll.202300634.

Chapter II

Ab Initio Computational Techniques and Solar Cell Simulation Tools

II.1 Introduction

The ab initio techniques covered in this chapter [1], in particular density functional theory (DFT) with Materials Studio's CASTEP tool [5], offer strong tools for investigating and forecasting the electrical, structural, and photovoltaic behavior of materials [8]. However, because of its superior optoelectronic qualities and high efficiency in thin-film solar cell applications, the quaternary semiconductor $CuIn(Se_{1-x}S)_2$ has drawn a lot of interest. This substance, which is a member of the chalcopyrite crystal family, has an adjustable straight band gap between 1.0 and 1.5 eV, making it perfect for effectively absorbing sunlight [18].

II.2.1 Ab initio methods

In quantum chemistry, the ab initio method is a computational technique that determines molecular properties only from basic physical principles, independent of empirical or experimental data. These techniques provide precise predictions of molecular geometry, energies, and electronic structures by solving the Schrödinger equation to explain the behaviour of electrons in a molecule [1].

The Hartree–Fock (HF) approach, which approximates electron interactions but ignores electron correlation, is a fundamental type of ab initio computation. By taking electron correlation effects into account, more sophisticated post-Hartree–Fock techniques like Møller–Plesset (MP2, MP4), Configuration Interaction (CI), and Coupled Cluster (CC) increase accuracy. Density Functional Theory (DFT), while not strictly ab initio, is frequently employed because it strikes a compromise between computational expense and precision [2].

Ab initio methods are widely used to analyse physical and chemical properties, but they are computationally challenging, especially for large molecules or high-level techniques, and they demand a lot of memory and processing capacity.

II.2.2 Common Types of Ab Initio Methods

II.2.2.1 Hartree–Fock (HF) Method

Hartree created what are now known as the Hartree equations for atoms in 1927, a year after Schrödinger first proposed his wave equation. Hartree expanded on Lindsay's idea of self-consistency, which was first put forth in relation to Bohr's atomic model, by proposing that the nucleus of an atom and the electrons that surround it could be thought of as creating a spherically symmetric potential field. The Schrödinger equation inside this potential, represented as v(r), was solved to determine the charge distribution of each electron. Hartree needed the final field, which was determined from the individual electron solutions, to match the initial anticipated field in order to guarantee correctness. The self-consistent field (SCF) method, which is still essential in quantum chemistry today, was developed as an iterative procedure to achieve agreement between the input and output potentials [3].

Consequently, a basic ab initio technique in quantum chemistry for approximating the electronic structure of atoms and molecules is the Hartree–Fock (HF) method. By assuming that every electron travels independently within an average field produced by every other electron, it resolves the Schrödinger equation. One Slater determinant is used to describe the entire wavefunction, guaranteeing that fermions are properly antisymmetric.
Schrödinger equation

$$H\psi = E\psi \tag{II.1}$$

where E: is the total energy of the system, ψ the wave function and H the Hamiltonian of this system. For a system with N nuclei and n electrons

$$H_{total} = T_n + T_e + V_{nn} + V_{ne} + V_{ee} \tag{II.2}$$

$$H = \frac{-\hbar^2}{2m}\sum_i \nabla_i^2 + \frac{1}{2}\sum_i^n \sum_{i\neq k}^n \frac{e^2}{4\pi\varepsilon_0 r_{ij}} + \sum_i^n \sum_k^N \frac{Z_k e^2}{4\pi\varepsilon_0 r_{ij}} - \frac{-\hbar^2}{2}\sum_k^N \frac{1}{M_k}\nabla_i^2 + \frac{1}{2}\sum_k^N \sum_l^N \frac{Z_k Z_l e^2}{4\pi\varepsilon_0 R_{ij}} \tag{II.3}$$

Where: m: is the mass of the electron.

r_{ij}: is the distance between electron i and electron j.

M_k: is the mass of the nucleus.

R_{kl}: is the distance between the centers of nuclei k and l.

Z_k, Z_l: The atomic numbers of nuclei k

T_c: is the kinetic energy of electrons.

T_n: is the kinetic energy of nuclei.

V_{ee}: is the electron-electron interaction energy.

V_{en}: is the nucleus-electron interaction energy.

V_{nn}: is the nucleus-nucleus interaction energy.

The "independent particle" or "independent electron" approximation are popular terms used to describe the Hartree–Fock (HF) technique. Rather than being disregarded, this simply implies that electron-to-electron interactions are handled in an averaged way. The method uses a mean-field approach rather than taking into account the precise repulsion between each pair of electrons.

As a result, a single spin orbital describes every electron in the system, and the total number of spin orbitals is equal to the number of electrons. The variational concept is then used to optimize these spin orbitals in order to provide the most accurate approximation of the electronic structure of the system.

The way electrons avoid one another is not fully taken into account by HF, which computes energy and molecular orbitals but ignores electron correlation. For systems where correlation is crucial, this reduces its accuracy. It does, however, form the foundation for more sophisticated techniques such as MP2 or Coupled Cluster. HF is frequently utilized as a foundation in theoretical physics and for geometry optimization.

II.2.2.2 Post-Hartree–Fock methods

The Hartree-Fock (HF) method's shortcomings, notably its disregard for electron correlation the interaction between electrons outside of the mean-field approximation were addressed by these sophisticated quantum chemistry techniques. Real electrons have a more direct impact on one another than HF, which treats electrons as flowing independently in an averaged field. This has an impact on the precision of computed energies and molecule characteristics[4]
A number of post-HF techniques have been developed to remedy this. By include correlation energy as a perturbative correction, Møller–Plesset perturbation theory (MP2, MP4) enhances HF results. More accurate treatment of excited states is made possible by Configuration Interaction (CI), which builds a wavefunction as a linear combination of several electronic configurations.[4]

Among the most accurate are Coupled Cluster (CC) approaches, especially CCSD and CCSD(T), which systematically incorporate correlations through an exponential expansion of the wavefunction.

Although these techniques provide far higher precision than Hartree-Fock, they require more computing power, particularly for big systems.

II.2.3 Density Functional Theory (DFT)

One popular quantum mechanical technique in computational chemistry and physics is density functional theory, or DFT. Since it is founded on basic physical principles and does not depend on experimental settings, it is sometimes grouped with ab initio approaches even though its foundation is not entirely ab initio[5].

DFT focusses on the electron density, a function of just three spatial variables, independent of the number of electrons, in contrast to wavefunction-based techniques like Hartree-Fock, which characterize the behavior of each electron separately. This increases the computational efficiency of DFT, particularly for solids and large molecular systems.

DFT is based on the Hohenberg–Kohn theorems, which assert that a system's electron density is the only factor that can determine all of its ground-state characteristics. The Kohn–Sham method greatly simplifies the problem by introducing a system of non-interacting electrons that produces the same density as the interacting system.

I.2.3.1 Hohenberg–Kohn theorems

Pierre Hohenberg and Walter Kohn developed the Hohenberg–Kohn theorems in 1964. According to these theorems, a many-electron system's electron density, not the entire many-electron wavefunction, is the only factor that can define its ground-state characteristics [6].

II.2.3.1.1 First Hohenberg–Kohn Theorem (Existence Theorem)

The external potential (and hence the Hamiltonian and other features of the system) is determined only by the ground-state electron density. This indicates that the ground-state electron density $\rho(r)$ contains all of the system's information, including the entire energy, forces, and wavefunction. You are fully aware of the system if you know the precise density [7].

$$E[\rho(\vec{r})] = F_{HK}[\rho(\vec{r})] + \int Ven(\vec{r})\rho(\vec{r})d\vec{r} \quad \text{(II.4)}$$

When $F_{HK}[\rho(\vec{r})]$ It is the universal Hohenberg–Kohn functional, which exists for any type of system and is expressed as:

$$F_{HK}[\rho(\vec{r})] = T\,[\rho(\vec{r})] + V\,[\rho(\vec{r})] \quad \text{(II.5)}$$

$T\,[\rho(\vec{r})]$ is the kinetic energy.

$V\,[\rho(\vec{r})]$ is the electron–electron interaction.

II.2.3.1.2 Second Hohenberg–Kohn Theorem (Variational Principle)

The energy functional is minimized by the proper ground-state electron density. By minimizing an energy functional E[ρ], this theorem offers a method for determining the ground-state density. The density that provides the least amount of energy is the genuine ground-state density [7].

$$E(\rho_0) = \min E(\rho) \quad \text{(II.6)}$$

II.2.3.2 The Kohn–Sham approach

A key element of Density Functional Theory (DFT), the Kohn–Sham (KS) approach offers a useful method for calculating the ground-state electron density, which makes it easier to solve the problem of many-electron systems quantum mechanical behavior. Kohn and Sham demonstrated that the self-consistent solution of the Kohn-Sham equations, a collection of single-particle Schrödinger-type equations, provides the correct density [8].

$$\left\{-\frac{1}{2}\nabla^2 + V_{KS}(r)\right\}\psi_i(r) = \varepsilon_i\psi_i(r) \quad \text{(II.7)}$$

This is the Kohn-Sham equation. It describes the behavior of the so-called Kohn-Sham orbitals $\psi_i(r)$ for non-interacting electrons in an effective potential V_{KS}(r). The operator $-1/2\nabla^2$ represents the kinetic energy, while V_{KS}(r) includes all electron-electron interactions via the effective Kohn-Sham potential. The eigenvalues ε_i correspond to the orbital energies.

The following equation is used to solve the Kohn and Sham equations and determine the total energy.

$$E(\rho) = \sum_{ioccup} \varepsilon_i - \int \frac{\rho(r)\rho(r)}{|r-r|} drdr + E_{XC}(\rho) - \int V_{XC}(r)\rho(r)dr \quad \text{(II.8)}$$

$\sum_{i\in occupied} \varepsilon_i$: Sum of eigenvalues for all occupied Kohn-Sham orbitals.

$E_{XC}(\rho)$: Exchange-correlation energy, which accounts for quantum mechanical effects beyond mean-field.

$-\int V_{XC}(r)\, \rho(r)\, dr$: This term subtracts the contribution of the exchange–correlation potential that was already included in the eigenvalues, to avoid double-counting.

Figure.II.1 illustrates the method adopted for solving the self-consistent problem of Kohn and Sham.

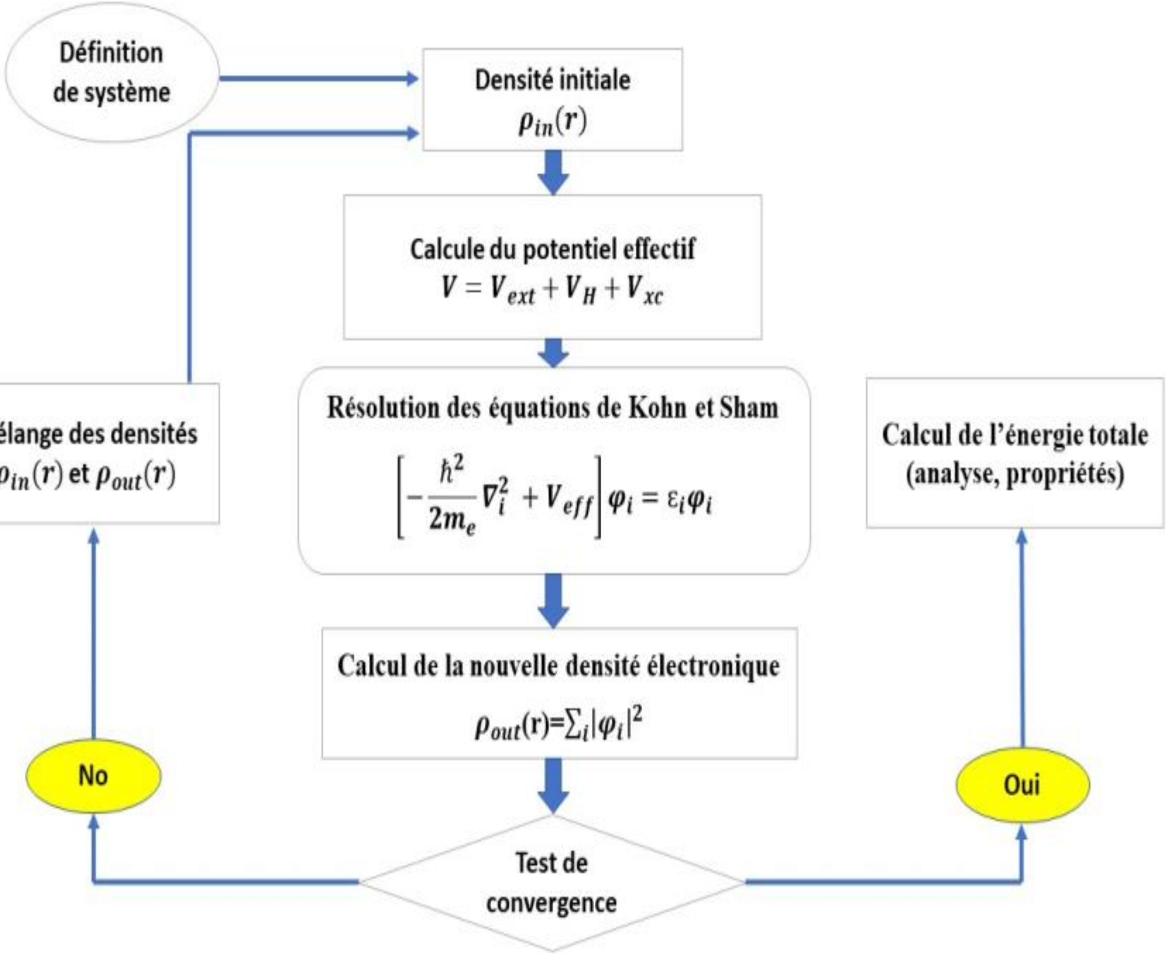

Figure II.1 Representation of the self-consistent cycle for solving the Kohn-Sham equations [21]

II.2.3.3 Exchange–Correlation Functional

Exchange-correlation functionals are used in DFT to account for electron correlation and exchange effects. The selection of these functionals, such as LDA, GGA, or hybrid types (e.g., B3LYP), has a significant impact on the accuracy of DFT. DFT is perfect for energy calculations, electronic property prediction, and shape optimization because it strikes a fair compromise between accuracy and computational cost.

II.2.4 Approximation

In order to make the Kohn-Sham equations and Density Functional Theory (DFT) actually applicable, an explicit expression for the exchange-correlation energy Exc(ρ) must be defined. However, an approximation must be made because the precise shape is unknown. For this reason, a number of strategies have been devised, including:

- **The Local Density Approximation (LDA)** which postulates that the local electron density is the only factor influencing the exchange-correlation energy at each location [9].
- **The Generalized Gradient Approximation (GGA)**, For inhomogeneous systems, the Generalized Gradient Approximation (GGA), which takes into account both the density and its spatial variation (gradient), provides more accuracy [10].

In addition to this, there are more sophisticated, non-local techniques that, in some circumstances, offer greater accuracy and take interactions across greater distances into consideration. Since they allow the estimation of electron correlation effects without resolving the entire many-body issue, these approximations serve as the foundation for realistic DFT computations.

II.2.4.1 Local Density Approximation (LDA)

Density functional theory (DFT), a quantum mechanical theory for examining the electronic structure of many-body systems, including atoms, molecules, and solids, relies heavily on LDA. According to DFT, a system's total energy is a functional of its electron density, ρ(r). By assuming that every location in a system acts as a homogeneous electron gas with the same local density, LDA approximates the exchange-correlation energy Exc[ρ], a vital but complex component of the total energy [11].

$$E_{xc}LDA[\rho]=\int\rho(r)\varepsilon_{xc}(\rho(r))\ dr \qquad \text{(II.9)}$$

where**:** $\varepsilon_{xc}(\rho)$ is the exchange-correlation energy per particle of a homogeneous electron gas at density ρ

Accurately characterizing the exchange-correlation (XC) energy, represented by the symbol Exc[ρ], which captures the many-body effects of electron exchange and correlation outside of the realm of conventional electrostatics, is the main issue in DFT. Approximations are necessary since the precise functional form of Exc[ρ] is unknown. One of the earliest and most straightforward approximations for this use is the LDA[11].

The main goal of the LDA is to use data from the homogeneous electron gas model—a system of electrons flowing in a uniform positive background charge density—to estimate the XC energy of an inhomogeneous electron system. Using quantum Monte Carlo techniques, this model has been solved with remarkable accuracy and yields trustworthy information for the XC energy per electron at a specific density.

II.2.4.2 Generalized Gradient Approximation (GGA)

Is a significant improvement on Density Functional Theory (DFT) that was created to increase the precision of exchange-correlation energy computations. By include both the local electron density and its gradient that is, how the density varies in space GGA goes beyond the Local Density Approximation (LDA), which assumes that the electron density is uniform or roughly constant at every location in space [10].

With this extra information, GGA can more accurately depict systems with widely fluctuating electron densities, including molecules, surfaces, or low-dimensional systems. Consequently, when compared to LDA, GGA offers more precise estimates for bond lengths, reaction energies, cohesive energies, and other molecular or material characteristics.

The exchange-correlation energy is expressed mathematically via GGA functionals as a function of the electron density ρ(r) and its gradient ∇ρ(r). As a result, the functionals become more adaptable and ideal for electron systems that are not homogeneous.

$$E_{XC}^{GGA}[\rho(\vec{r})] \approx \int \varepsilon_{XC}[\rho(\vec{r}), |\nabla\rho(\vec{r})|]\rho(\vec{r})dr \qquad \text{(II.10)}$$

Where $\varepsilon_{XC}[\rho(\vec{r}), |\nabla\rho(\vec{r})|]$ represents the exchange-correlation energy per electron in a system of mutually interacting electrons of non-uniform density

In the context of Density Functional Theory (DFT) computations, the Generalized Gradient Approximation (GGA) provides a number of significant advantages. GGA is a popular and reliable tool in computational chemistry and materials science because of these benefits: Higher Accuracy Compared to LDA GGA can better capture changes in electron distribution since it incorporates both the local electron density and its gradient. Compared to the Local Density Approximation (LDA), this results in predictions of structural, electrical, and energetic properties that are more accurate.

Improved Surface and Molecule Treatment For molecular systems, surfaces, and inhomogeneous materials where the electron density fluctuates quickly GGA outperforms LDA by a considerable margin.

Dependable Energies and Geometries Understanding chemical reactivity and stability requires knowledge of bond lengths, binding energies, and reaction energies, all of which are generally improved by GGA functionals.

II.2.4.3 The meta-Generalized Gradient Approximation (meta-GGA or mGGA)

Is a sophisticated class of Density Functional Theory (DFT) exchange-correlation functionals. By including the kinetic energy density, commonly known as the Laplacian of the density, in addition to the electron density and its gradient, it improves upon the Generalized Gradient Approximation(GGA)[12].

In research involving transition metals, semiconductors, and noncovalent interactions, where conventional GGAs might not be enough, meta-GGA is very helpful.

II.2.4.3.1 Key Features of meta-GGA:

- ✓ Greater Accuracy: mGGA functionals are able to characterize both localized and delocalized electrons more accurately by incorporating more specific information about the electronic environment, such as kinetic energy density [13].

- ✓ Bridges the gap between GGA and Hybrid Functionals: mGGAs frequently provide precision comparable to hybrid functionals, which combine exact exchange and computational cost.
- ✓ Enhanced Performance: With a reasonable computational cost, meta-GGA functionals typically provide more accuracy than LDA and GGA in predicting atomization energies, reaction barriers, structural characteristics, and occasionally band gaps.

II.2.5 Applications of Ab Initio Methods

Ab initio techniques are essential to semiconductor research and design. Among their uses are:

II.2.5.1 Electronic Structure Calculation

In order to comprehend electrical and optical behaviour, they aid in the determination of band structures, band gaps, and density of states[14] .

II.2.5.2 Defect and Doping Analysis

Ab initio simulations help design more efficient devices by illuminating the effects of flaws, impurities, and dopants on semiconductor performance[15].

II.2.5.3 Optoelectronic Properties

For LEDs, solar cells, and photodetectors, they forecast optical absorption, photoluminescence, and dielectric functions[16].

II.2.5.4 Surface and Interface Studies

beneficial for investigating heterojunctions, passivation layers, and surface reconstructions—all of which are essential in components like transistors and solar cells [17].

II.2.5.5 Strain and Lattice Dynamics

They evaluate the effects of phonons, strain, and temperature characteristics on material stability and carrier mobility.

II.3 $CuIn(Se_{1-x}S)_2$ semiconductor

The chemical formula Two semiconducting compounds are represented by the solid solution or alloy $CuIn(Se_{1-x}S)_2$: Copper indium disulfide, or $CuInS_2$, and copper indium diselenide, or $CuInSe_2$ [18]

II.3.1 Composition and Meaning of $(Se_{1-x}S)_2$

- ✓ The crystallographic location is shared by the atoms of sulfur (S) and selenium (Se).
- ✓ The fraction of sulfur is determined by the variable x ($0 \leq x \leq 1$), whereas the fraction of selenium is given by $1 - x$.
- ✓ So:
  - ➢ If $x = 1$, the material is pure $CuInS_2$.
  - ➢ If $x = 0$, it's pure $CuInSe_2$.
  - ➢ Intermediate values (e.g., $x = 0.5$) represent mixed compositions.

II.3.2 Crystal Structure

- ✓ $CuIn(Se_{1-x}S)_2$ crystallizes in the chalcopyrite structure, which is a tetragonal distortion of the cubic zinc blende (sphalerite) lattice.
- ✓ Its space group is I-42d (No. 122).
- ✓ The unit cell contains eight atoms: two Cu, two In, and four chalcogen (S and/or Se) atoms.
- ✓ Four anions (S/Se) tetrahedrally coordinate each cation (Cu or In), while two Cu and two In atoms encircle each anion.

II.3.3 Lattice Parameters

- ✓ The lattice constants vary with the S/Se ratio (**x**):
  - ➢ $CuInSe_2$: $a \approx 5.78$ Å, $c \approx 11.62$ Å
  - ➢ $CuInS_2$: $a \approx 5.52$ Å, $c \approx 11.05$ Å
- ✓ Because S has a smaller ionic radius than Se, the lattice constants fall as the S content rises.

II.3.4 Ordering and Defects

- ✓ The electrical characteristics and structural symmetry are impacted by anion mixing (S/Se substitution) and cation disorder (Cu-In antisite defects)..
- ✓ Ab initio techniques are frequently used to study defects like vacancies and antisites in order to determine their formation energies and performance effects.

II.3.5 Band Gap Energy (Eg)

- ✓ Tunable from ~1.0 eV ($CuInSe_2$) to ~1.5 eV ($CuInS_2$).
- ✓ This band gap range is ideal for solar energy absorption, especially in thin-film photovoltaics.
- ✓ The band gap increases with sulfur content (x) due to stronger S–p orbital interactions.
- ✓ Because ordinary DFT (like GGA) frequently underestimates Eg, ab initio calculations are necessary for precise prediction.

II.3.6 Band Structure

- ✓ The Γ point shows a direct band gap, which is advantageous for optoelectronic devices.
- ✓ Cu 3d and Se/S 4p orbitals make up the majority of the valence band maximum (VBM).
- ✓ The In 5s and Se/S 4p orbitals are the primary sources of the conduction band minimum (CBM).

II.3.7 Carrier Transport

- ✓ Shows high absorption coefficient ($>10^5$ cm^{-1}) near the band edge.
- ✓ Typically, p-type conductivity results from the shallow acceptors known as copper vacancies (V_Cu).
- ✓ Good carrier mobility is made possible by the moderate effective mass of electrons and holes.
- ✓ Effective masses, density of states, and carrier lifetimes are computed using ab initio methods.

II.3.8 Dielectric Properties

- ✓ Although it varies with composition, the static dielectric constant often promotes effective charge defect screening.
- ✓ Crucial for reducing solar cell recombination losses

II.4 Advantages of $CuIn(Se_{1-x}S)_2$

a) Tunable Band Gap (1.0–1.5 eV) A large portion of the solar spectrum can be covered by optimizing the band gap for solar absorption by varying the S/Se ratio (x).

b) High Absorption Coefficient allows for the employment of small absorber layers (~1–2 µm) since it efficiently absorbs sunlight ($>10^5$ cm^{-1}).

c) Direct Band Gap facilitates: efficient electron-hole generation and separation, increasing device efficiency.

d) Flexible Composition Engineering Structural and electrical properties can be modified using elemental substitution (S/Se).

e) Good Thermal and Chemical Stability: Suitable for outdoor photovoltaic use, stable under a variety of environmental situations.

f) Good Photovoltaic Performance: Optimized $CuInGa(S,Se)_2$ (CIGS) devices have demonstrated efficiencies of over 20% in laboratory-scale solar cells. Furthermore, it demonstrates low temperature coefficients, preserving functionality in hot conditions.

g) Flexibility and Lightweight Suitable: for applications requiring portability and limited space, it can be placed onto flexible surfaces.

II.5 Inconvenances of $CuIn(Se_{1-x}S)_2$

II.5.1 Indium scarcity and Cost: Indium is relatively rare and expensive, limiting large-scale commercial deployment [19].

II.5.2 Toxicity concerns: Although less toxic than cadmium-based materials, selenium can pose environmental risks during manufacturing and disposal [20].

II.5.3 Complex Stoichiometry Control: Requires precise control of Cu, In, S, and Se ratios to avoid defects (e.g., antisites, vacancies) that reduce performance.

II.5.4 Cation disorder: Cu–In antisite defects can introduce mid-gap states, increasing carrier recombination and lowering efficiency.

II.5.5 Phase segregation Risks: Under certain processing conditions, S-rich or Se-rich phases can segregate, leading to non-uniform performance.

II.6 Numerical Simulation Tool: SCAPS-1D

II.6.1 Introduction to SCAPS-1D

SCAPS-1D The One-Dimensional Solar Cell Capacity Simulator is a powerful numerical tool developed at the University of Gent, Belgium, to simulate the electrical behavior of thin-film heterojunction solar cells under both dark and illuminated conditions [22,23]. It provides reliable current–voltage (I–V) characteristics that closely reproduce experimental behavior. Originally, the software was designed for modeling CdS- and $Cu(In,Ga)(Se,S)_2$ based thin-film photovoltaic devices, which are among the most promising candidates for high-efficiency solar cell technologies [24].

A key strength of SCAPS-1D is its flexibility: it can simulate device architectures composed of multiple semiconductor layers with user-defined doping profiles that vary spatially. The program also includes advanced defect modeling, accounting for both donor and acceptor states in the absorber and other layers. These defect states can be described by various energy distributions discrete levels, Gaussian functions, or band-tail states located either in the semiconductor bulk or at heterojunction interfaces.

In addition, SCAPS-1D enables detailed optical and electrical simulations under a wide range of conditions. It can model device responses to different spectral illuminations, such as monochromatic light or the standardized AM1.5G solar spectrum, while considering variations in bias voltage, illumination intensity, and temperature. The program also calculates transmitted and absorbed spectra within arbitrary frequency ranges, allowing precise analysis of light–matter interactions inside the solar cell.

In this study, SCAPS-1D has been chosen as a practical bridge between first-principles calculations and device-level performance analysis. Key parameters such as band gap, absorption coefficient, refractive index, and defect densities, partly obtained from DFT calculations were used as inputs, enabling a realistic assessment of the photovoltaic performance of $CuIn(Se_{1-x}S_x)_2$ based solar cells.

II.6.2 Model Construction and Simulation Workflow

II.6.2.1 Device Structure

A typical thin-film solar cell consists of several stacked layers, each performing a specific function:

- **Front Electrode (Transparent Conductive Oxide, TCO):** Acts as a transparent contact that allows light to enter while conducting collected carriers to the external circuit. Common materials include ZnO, ITO, or FTO [25].
- **Buffer/Window Layer:** Located directly below the TCO, typically made of CdS or ZnO. It forms an n-type region, minimizes interface recombination, and helps establish the main junction [26].
- **Absorber Layer:** The active layer (e.g., CdTe, CIGS, CZTS) that absorbs photons and generates electron–hole pairs. Its thickness and material properties are critical for device efficiency [27].
- **Back Contact:** Usually a metal such as Mo, Au, or Al, ensuring good carrier extraction and circuit completion [25].

The thickness, composition, and doping of these layers can be tuned to optimize photovoltaic performance.

The figure II.2 shows the main interface of SCAPS-1D used to construct and visualize the solar cell layer sequence and specify structural/model parameters prior to simulation.

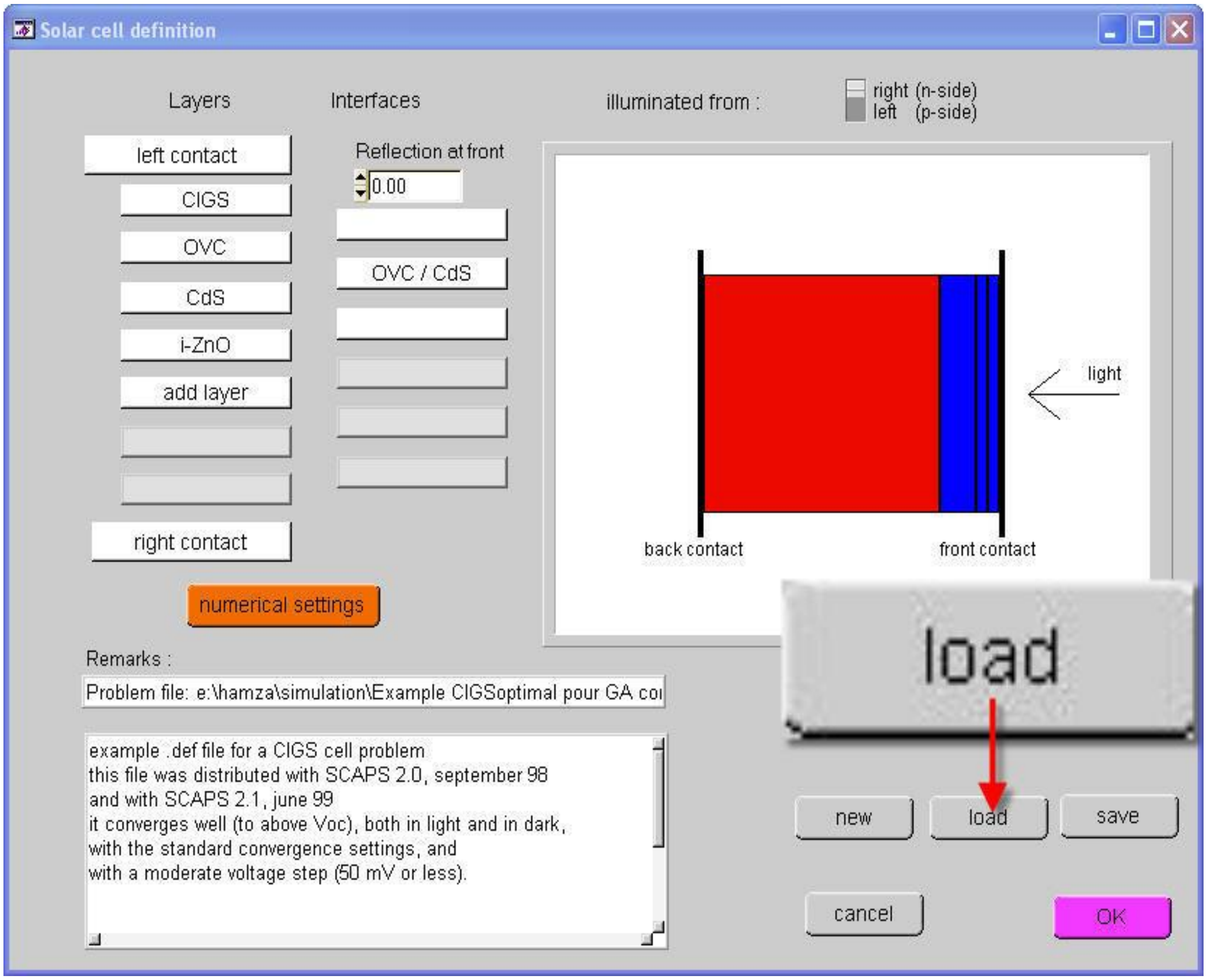

Problem file: e:\hamza\simulation\Example CIGSoptimal pour GA co

example .def file for a CIGS cell problem
this file was distributed with SCAPS 2.0, september 98
and with SCAPS 2.1, june 99
it converges well (to above Voc), both in light and in dark,
with the standard convergence settings, and
with a moderate voltage step (50 mV or less).

Figure II.2 SCAPS-1D Interface for Solar Cell Structure Definition

II.6.2.2 Key Simulation Parameters

Accurate modeling requires input of essential physical and material parameters for each layer, including:

- **Layer Thickness (t):** Ranging from tens of nanometers (buffer) to several micrometers (absorber), affecting light absorption and carrier transport [28].
- **Energy Band Gap (Eg):** Determines the spectral absorption range and must balance light absorption with minimized losses [27].
- **Doping Concentration (ND, NA):** Defines conductivity type, carrier density, and electric field distribution [29].

- **Defect Density and Types:** Bulk or interface traps and recombination centers characterized by their energy levels and capture cross-sections [30].
- **Carrier Mobilities (µn, µp):** Influence charge transport efficiency via drift and diffusion [31].
- **Optical Constants (n, k):** Such as refractive index and absorption coefficient, governing light matter interaction [32].

II.6.2.3 Application to $CuIn(Se_{1-x}S_x)_2$ Solar Cells

For $CuIn(Se_{1-x}S_x)_2$ based devices, the simulated structure typically includes [33]:

- **Front Contact (TCO):** ZnO:Al or ITO.
- **Buffer Layer:** Usually CdS, which improves band alignment and reduces interface recombination.
- **Absorber Layer:** $CuIn(Se_{1-x}S_x)_2$, serving as the photon-absorbing and carrier-generating layer.
- **Back Contact:** Often Mo, providing a good ohmic contact with the absorber.

The following parameters are crucial:

- **Layer Thickness (t):** Governs absorption and carrier transport.
- **Band Gap (Eg):** Varies with the S/Se ratio.
- **Electron Affinity (χ) and Dielectric Constant (ε):** Control band alignment and charge screening.
- **Doping Concentration (N_D, N_A):** Determines conductivity and carrier density.
- **Carrier Mobilities (µn, µp):** Define transport efficiency.
- **Defect States:** Bulk/interface defect densities, energy levels, and capture cross-sections.
- **Optical Constants (n, k):** Derived from DFT calculations and converted into absorption coefficients (α) and reflectivity (R).

II.6.2.4 Simulation Workflow in SCAPS-1D

The SCAPS-1D simulation process follows a systematic sequence [33]:

1. **Define Layer Stack:** Enter layer sequence and thicknesses.
2. **Assign Material Parameters:** Eg, χ, ε, μn, μp, Nc, Nv, and optical constants.
3. **Introduce Defects:** Bulk and interface states with proper energy levels and recombination parameters.
4. **Set Boundary Conditions:** Define contact types (ohmic or Schottky) and work functions.
5. **Operating Conditions:** Choose illumination (AM1.5G, 1000 W/m^2), temperature, and applied bias.
6. **Numerical Solution:** Run the self-consistent solver for Poisson and continuity equations.
7. **Extract Results:** Current–voltage (I–V) curves, efficiency, quantum efficiency spectra, band diagrams, and carrier distributions.

II.6.3 Key Simulation Features and Outputs

The SCAPS-1D software provides a wide range of features and outputs essential for evaluating and analyzing the performance of thin-film solar cells. The primary outputs and characteristics include [27],[34]:

a. **Current-Voltage (I-V) Curve:** This curve shows the relationship between the electrical current and the voltage applied to the solar cell, enabling the calculation of key performance parameters such as open-circuit voltage (Voc), short-circuit current density (Jsc), fill factor (FF), and overall efficiency of the device.

b. **Capacitance-Voltage (C-V) Curve:** This output is employed to understand junction characteristics and charge distribution within the device layers.

c. **AC Response Analysis:** It studies the device behavior under varying frequencies to investigate transport properties and electrical dynamics of the cell.

d. **External Quantum Efficiency (EQE):** EQE represents the cell's ability to convert photons of different wavelengths into effective electrical charges, thus revealing wavelength-dependent conversion efficiency.

e. **Energy Band Diagram:** This provides a visual representation of the energy levels throughout the different layers, aiding the analysis of charge transport mechanisms and potential barriers.

f. **Defect and Recombination Analysis:** SCAPS-1D allows detailed modeling of bulk and interface defect states and their impact on device performance by defining their energy levels and recombination parameters.

g. **Batch Calculations Support:** The software facilitates repeated simulations with varying parameters to systematically study their influence and optimize device design.

h. **Quantum Tunneling Modeling:** Detailed modeling of quantum tunneling effects across thin barrier layers is included, which is crucial for devices with ultra-thin layers.

Figure II.3 shows the graphical representations available in the Energy Band Panel of SCAPS-1D visualizing band edges, carrier profiles, current densities, and deep defect occupancies, all of which are critical for in-depth device analysis.

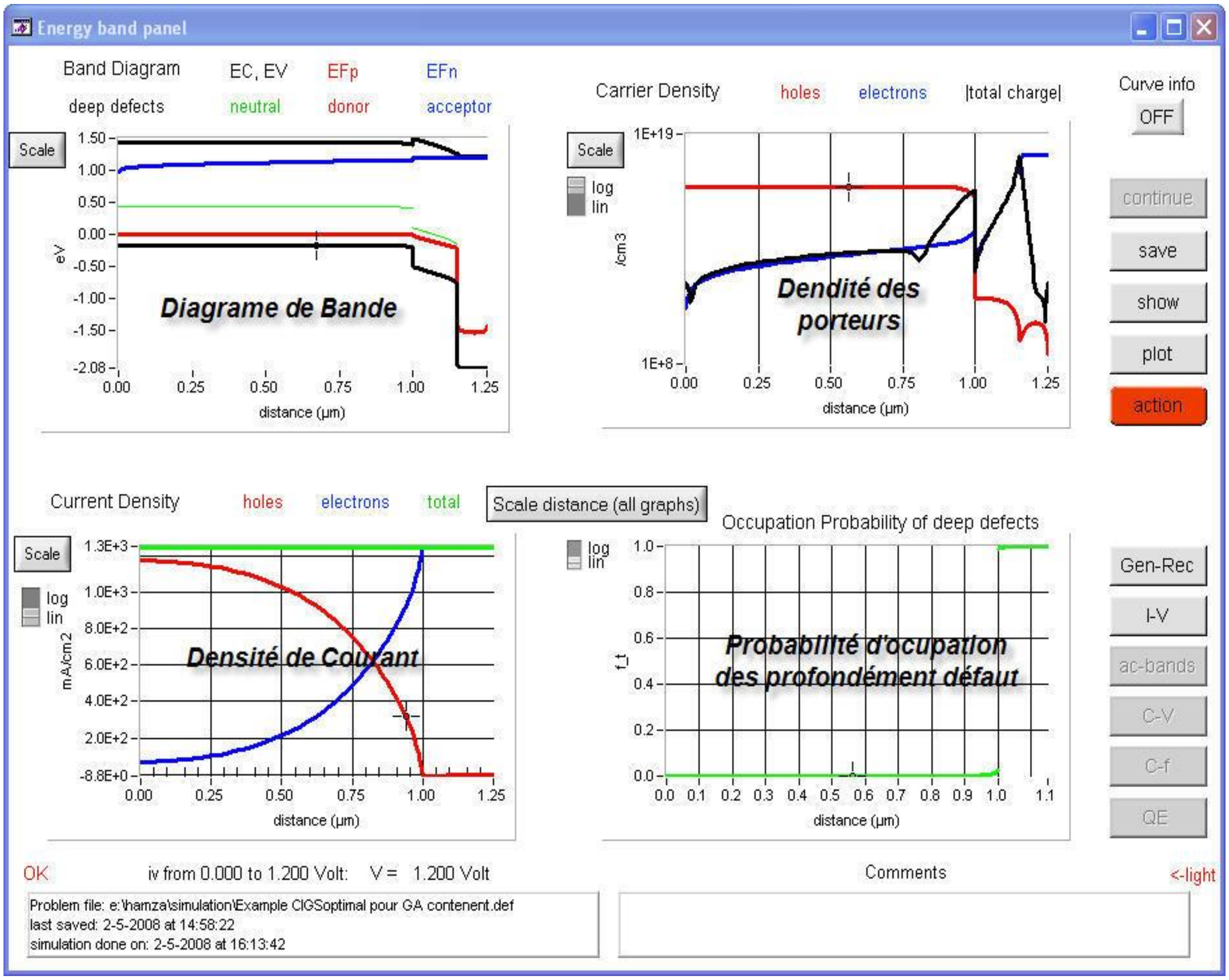

OK iv from 0.000 to 1.200 Volt: V = 1.200 Volt

Problem file: e:\hamza\simulation\Example CIGSoptimal pour GA contenent.def
last saved: 2-5-2008 at 14:58:22
simulation done on: 2-5-2008 at 16:13:42

Figure II.3 Energy Band Panel in SCAPS-1D: Visualization of Band Edges, Carrier Profiles, and Defect States

II.6.4 Effect on This Work

In this research, SCAPS-1D serves as a complementary tool to the ab initio calculations performed using Density Functional Theory (DFT). While the first-principles approach carried out with CASTEP provides fundamental material properties such as band gap, refractive index, extinction coefficient, and defect formation tendencies, SCAPS-1D translates these microscopic inputs into macroscopic device performance predictions.

Specifically:

- Band Gap (Eg): The tunable band gap values obtained from DFT calculations for

CuIn $(Se_{1-x}S_x)_2$ were directly used to define the absorber layer parameters within SCAPS-1D.

- Optical Constants (n, k): The refractive index and extinction coefficients computed from DFT were converted into absorption coefficients and reflectivity values, which were incorporated into SCAPS-1D to accurately model photon absorption and carrier generation processes.
- Defect Parameters: Insights gained from DFT regarding vacancies and antisite defects guided the selection of defect densities, energy levels, and capture cross-sections modeled in the simulator.
- Band Alignment: Electron affinity and dielectric constant values derived from DFT were employed to adjust conduction and valence band offsets at heterojunction interfaces within the device model.

By combining these two approaches, the study establishes a direct linkage between microscopic material properties predicted via ab initio calculations and the macroscopic photovoltaic behavior simulated by SCAPS-1D. This synergy enhances the understanding of how sulfur concentration and defect states impact the performance of $CuIn(Se_{1-x}S)_2$ thin-film solar cells.

II.7 Conclusion

Chapter II presents a comprehensive overview of ab initio computational techniques, with a particular focus on Density Functional Theory (DFT) using the CASTEP module within Materials Studio, as powerful tools for exploring and predicting the structural, electronic, and photovoltaic properties of semiconductor materials. The chapter emphasizes the suitability of the $CuIn(Se_{1-x}S)_2$ alloy, a chalcopyrite semiconductor with a tunable direct band gap ranging from 1.0 to 1.5 eV, for high-efficiency thin-film solar cells due to its excellent optoelectronic characteristics and capacity for band gap engineering via sulfur and selenium composition.

The theoretical background includes foundational quantum chemistry methods such as Hartree-Fock and post-Hartree-Fock techniques, highlighting their limitations particularly in electron correlation treatment, which DFT addresses effectively through the use of exchange-correlation functionals. Various approximation methods within DFT Local Density Approximation (LDA), Generalized Gradient Approximation (GGA), and meta-GGA are detailed as vital to accurate computational predictions.

The chapter further elucidates the crystal structure, compositional tuning, defect characteristics, band structure, carrier transport, and dielectric properties of $CuIn(Se_{1-x}S)_2$, underscoring the importance of controlling stoichiometry and defects for optimized device performance. Despite challenges such as cation disorder, defect formation, and material scarcity (notably indium), ab initio calculations provide critical insights for guiding experimental efforts and improving photovoltaic device designs.

Moreover, the integration of computational tools like CASTEP for electronic structure and SCAPS-1D for device-level simulation bridges the gap between fundamental material properties and device performance, enabling a holistic approach to solar cell optimization. The chapter concludes that leveraging these computational techniques significantly advances the understanding and development of $CuIn(Se_{1-x}S)_2$ based thin-film solar cells, thereby contributing to the progress of next-generation photovoltaic technologies.

References

[1] K. Laasonen, "Ab initio molecular dynamics," *Methods in Molecular Biology*, vol. 924, 2013, doi: 10.1007/978-1-62703-17-5_2.

[2] J. P. Martinez, "The Hartree-Fock method: from self-consistency to correct symmetry," *Ann Phys*, vol. 529, no. 1–2, 2017, doi: 10.1002/andp.201600328.

[3] S. Gulania and J. D. Whitfield, "Limitations of Hartree-Fock with quantum resources," *Journal of Chemical Physics*, vol. 154, no. 4, 2021, doi: 10.1063/5.0018415.

[4] Y. Shikano, H. C. Watanabe, K. M. Nakanishi, and Y. ya Ohnishi, "Post-Hartree–Fock method in quantum chemistry for quantum computer," 2021. doi: 10.1140/epjs/s11734-021-00087-z.

[5] D. Bagayoko, "Understanding density functional theory (DFT) and completing it in practice," *AIP Adv*, vol. 4, no. 12, 2014, doi: 10.1063/1.4903408.

[6] L. Garrigue, "Hohenberg–Kohn Theorems for Interactions, Spin and Temperature," *J Stat Phys*, vol. 177, no. 3, 2019, doi: 10.1007/s10955-019-02365-6.

[7] A. Zhou, "A mathematical aspect of Hohenberg-Kohn theorem," *Sci China Math*, vol. 62, no. 1, 2019, doi: 10.1007/s11425-018-9337-2.

[8] J. K. Desmarais, G. Ambrogio, G. Vignale, A. Erba, and S. Pittalis, "Generalized Kohn-Sham approach for the electronic band structure of spin-orbit coupled materials," *Phys Rev Mater*, vol. 8, no. 1, 2024, doi: 10.1103/PhysRevMaterials.8.013802.

[9] J. Li, S. Meng, J. Niu, and H. Lu, "Electronic structures and optical properties of monoclinic ZrO2 studied by first-principles local density approximation + U approach," *Journal of Advanced Ceramics*, vol. 6, no. 1, 2017, doi: 10.1007/s40145-016-0216-y.

[10] J. P. Perdew, K. Burke, and M. Ernzerhof, "Generalized gradient approximation made simple," *Phys Rev Lett*, vol. 77, no. 18, 1996, doi: 10.1103/PhysRevLett.77.3865.

[11] M. Lewin, E. H. Lieb, and R. Seiringer, "THE LOCAL DENSITY APPROXIMATION IN DENSITY FUNCTIONAL THEORY," *Pure and Applied Analysis*, vol. 2, no. 1, 2020, doi: 10.2140/paa.2020.2.35.

[12] H. Peng, Z. H. Yang, J. P. Perdew, and J. Sun, "Versatile van der Waals density functional based on a meta-generalized gradient approximation," *Phys Rev X*, vol. 6, no. 4, 2016, doi: 10.1103/PhysRevX.6.041005.

[13] F. Hofmann and S. Kümmel, "Molecular excitations from meta-generalized gradient approximations in the Kohn-Sham scheme," *Journal of Chemical Physics*, vol. 153, no. 11, 2020, doi: 10.1063/5.0023657.

[14] S. Curtarolo, D. Morgan, and G. Ceder, "Accuracy of ab initio methods in predicting the crystal structures of metals: A review of 80 binary alloys," *CALPHAD*, vol. 29, no. 3, 2005, doi: 10.1016/j.calphad.2005.01.002.

[15] X. Zhang *et al.*, "Synergistic Boron Doping of Semiconductor and Dielectric Layers for High-Performance Metal Oxide Transistors: Interplay of Experiment and Theory," *J Am Chem Soc*, vol. 140, no. 39, 2018, doi: 10.1021/jacs.8b06395.

[16] Y. Xu *et al.*, "Unraveling Crystallization Mechanisms and Electronic Structure of Phase-Change Materials by Large-Scale Ab Initio Simulations," *Advanced Materials*, vol. 34, no. 11, 2022, doi: 10.1002/adma.202109139.

[17] S. A. Fischer, C. M. Isborn, and O. V. Prezhdo, "Excited states and optical absorption of small semiconducting clusters: Dopants, defects and charging," *Chem Sci*, vol. 2, no. 3, 2011, doi: 10.1039/c0sc00626b.

[18] W. Wirjoadi and B. Siswanto, "PENGARUH KANDUNGAN SULFUR TERHADAP KONSTANTE KISI KRISTAL CuIn (Sx,Se1-x)2," *GANENDRA Majalah IPTEK Nuklir*, vol. 13, no. 2, 2010, doi: 10.17146/gnd.2010.13.2.50.

[19] A. Tanaka *et al.*, "Review of pulmonary toxicity of indium compounds to animals and humans," 2010. doi: 10.1016/j.tsf.2009.10.123.

[20] X. Nie *et al.*, "Bioconversion of inorganic selenium to less toxic selenium forms by microbes: A review," 2023. doi: 10.3389/fbioe.2023.1167123.

[21] S. Cottenier *et al.*, "Density functional theory and the family of (l) apw-methods: a step-by-step introduction," *Instituut voor Kern-en Stralingsfysica, KU Leuven, Belgium*, vol. 4, no. 0, p. 41, 2002.

[22] A. Niemegeers, S. Gillis et M. Burgelman, 1998. " UN programme de l'utilisateur pour simulation réaliste d'heterojunction du polycrystalline cellules solaires: SCAPS-1D ", Débats de la 2e Conférence Mondiale sur Conversion D'énergie Photovoltaïque (Wien, Österreich, july 1998), pp. 672-675, JRC, Ordre européen,

[23] M. Burgelman, P. Nollet et S. Degrave, semi-conducteur du polycrystalline du 1999. " Modelage cellules " solaires, (a invité) a présenté à la Société de la Recherche des Matières européenne, E-MRS, Strasbourg, France.

[24] A. Niemegeers et M. Burgelman, modelage 1996. " Numérique d'ac caractéristiques de CdTe et CIS cellules " solaires, Proc. 25e IEEE Conférence des Spécialistes Photovoltaïque (D.C. de Washington, april 1996), pp. 901-904, IEEE, Nouveau York,

[25] Acevedo-Luna, A., Bernal-Correa, R., Montes-Monsalve, J., & Morales-Acevedo, A. (2017). Design of thin film solar cells based on a unified simple analytical model. *Journal of applied research and technology*, *15*(6), 599-608.

[26] Mostakim, K., & Hasanuzzaman, M. (2022). Solar photovoltaic thermal systems. In *Technologies for Solar Thermal Energy* (pp. 123-150). Academic Press.

[27] El-Naggar, A. A., Eid, A. M., Rafat, Y., Khamis, M. A., Bakry, M., Elkun, S., ... & Abdelfatah, M. (2025). SCAPS simulation and design of highly efficient CuBi2O4-based thin-film solar cells (TFSCs) with hole and electron transport layers. *Scientific Reports*, *15*(1), 28300.

[28] Acevedo-Luna, A., Bernal-Correa, R., Montes-Monsalve, J., & Morales-Acevedo, A. (2017). Design of thin film solar cells based on a unified simple analytical model. *Journal of applied research and technology*, *15*(6), 599-608.

[29] Jahan, N., Khan, R., & Matin, M. A. (2024). Design and simulation of highly efficient CZTS/CZTSSe based thin-film solar cell. *Heliyon*, *10*(21).

[30] Araújo, V. H. D., Nogueira, A. F., Tristão, J. C., & dos Santos, L. J. (2025). Advances in Lead-Free Perovskite Solar Cell Design via SCAPS-1D Simulations. *RSC Sustainability*.

[31] Maiberg, M., Song, C. Y., Morawski, M., Neduck, F., Kempa, H., Damm, J., ... & Scheer, R. (2024). Toward digital twins by one-dimensional simulation of thin-film solar cells: Cu (In, Ga) Se 2 as an example. *Physical Review Applied*, *21*(3), 034051.

[32] Hafaifa, L., Maache, M., Rabhi, S., Allam, Z., Gouchida, Z. I., Benbouzid, Y., ... & Adjouz, R. (2025). Enhanced CZTSSe thin-film solar cell efficiency: key parameter analysis. *physica status solidi (a)*, *222*(2), 2400332.

[33] Kodigala, S. R. (2010). Cu (In1− xGax) Se2 and CuIn (Se1− xSx) 2 thin film solar cells. In *Thin films and nanostructures* (Vol. 35, pp. 505-679). Academic Press.

[34] Burgelman, M., Nollet, P., & Degrave, S. (2000). Modelling polycrystalline semiconductor solar cells. *Thin solid films*, *361*, 527-532.

Chapter III

Results and Discussions

III.1 Introduction

Solar cells represent one of the most promising and rapidly evolving technologies in the field of renewable energy, primarily because they enable the direct conversion of solar radiation into electrical energy through environmentally friendly and sustainable means. Among the various materials employed in the development of these cells, chalcopyrite-type compounds, particularly $CuInSe_2$(copper indium selenide), have garnered significant attention due to their exceptional optoelectronic properties [1]. These include a high absorption coefficient in the visible spectrum and a near-optimal band gap (~1.0 eV) that is particularly well-suited for solar energy conversion [2], in addition to superior thermal stability and resistance to photo-degradation [3]. The energy band gap (Eg) is a decisive factor that influences the electrical conductivity of solids: materials with large band gaps behave as insulators, while those with moderate gaps are classified as semiconductors; conductors, on the other hand, often exhibit very narrow or nonexistent gaps due to valence-conduction band overlap. The band-gap value is a unique property of each semiconductor and plays a key role in determining the overall efficiency and performance of solar cells made from them. Despite the progress made, efforts to enhance the efficiency and adaptability of these devices remain a central focus of current research [4–7].

One particularly promising strategy for improving the performance of $CuInSe_2$ based solar cells is sulfur doping, where part of the selenium is replaced with sulfur to form the alloyed compound $CuIn(Se_{1-x}S_x)_2$. This modification enables fine-tuning of the band gap and other material properties, potentially increasing device efficiency. A number of studies have been dedicated to understanding the impact of sulfur incorporation into $CuInSe_2$. For example, Xiao et al. [8] synthesized $CuIn\ (Se_{1-x}S_x)_2$ using a simple solvothermal method and investigated the changes in lattice parameters and optical characteristics. Eisener et al. [9] employed the solution Bridgman technique with CuInSe as a solvent to grow crystals of the same compound and studied the influence of sulfur on its electrical and optical behaviour. In another effort, Wang et al. [10] fabricated thin films of $CuIn\ (Se_{1-x}S_x)_2$ by carefully adjusting the sulfurization temperature of $CuInSe_2$, providing insight into the effect of synthesis conditions on film quality. Chen et al. [11] performed first-principles calculations to explore how variations in lattice volume due to sulfur doping affect the band-gap. Similarly, Sheppard et al. [12] developed a two-step deposition process to achieve single-phase $CuIn(Se_{1-x}S_x)_2$ and validated its phase purity and uniformity. Zeaiter and Llinares [13] employed spectroscopic ellipsometry to characterize the optical constants of the alloy and observed how these evolve with sulfur content. While these works have contributed significantly to the understanding of $CuIn(Se_{1-x}S_x)_2$, most studies remain limited to either end compositions (x = 0 or x = 1), leaving a gap in the detailed investigation of compositional dependence.

The present study aims to address this gap by performing a comprehensive theoretical investigation of the structural, electronic, and optical properties of $CuIn(Se_{1-x}S_x)_2$ across the full range of sulfur concentrations, with specific focus on the composition dependence of key parameters. Using first-principles calculations based on density functional theory (DFT), as implemented in the CASTEP code within the Materials Studio framework [14,15], and employing the generalized gradient approximation (GGA) [16], this research systematically analyses the evolution of dielectric function, refractive index, extinction coefficient, reflectivity, band gap, and optical conductivity. The computed results are thoroughly compared with available experimental and theoretical data to ensure consistency and reliability. This work not only enhances the fundamental understanding of $CuIn(Se_{1-x}S_x)_2$ chalcopyrite alloys but also highlights their potential applications in next-generation optoelectronic and photovoltaic devices, offering pathways for designing tunable materials with optimised light–matter interaction properties.

III.2. Computational Details

III.2.1 Calculation Details

$CuIn(Se_{1-x}S_x)_2$ and related chalcopyrite-type semiconductors have attracted significant attention in recent years as leading candidates for next-generation, high-efficiency thin-film photovoltaic technologies. Their growing prominence is primarily attributed to their outstanding optoelectronic properties, which include high absorption coefficients in the visible to near-infrared spectral range, direct and tunable band gaps ideally suited for solar energy harvesting, and excellent charge carrier transport and collection characteristics [1,17-19]. These intrinsic features make them particularly attractive as absorber layers in solar cell architectures, enabling devices with improved efficiency, flexibility, and long-term stability.

Structurally, $CuIn(Se_{1-x}S_x)_2$ crystallizes in the well-known tetragonal chalcopyrite structure, characterized by tetrahedral coordination geometry in which each cation is surrounded by four anions forming a [Cu/In–Q_4] unit (Q = Se or S). This arrangement can be conceptualized as a derivative of the cubic zinc blende (sphalerite) lattice, where two face-centered cubic (FCC) sub-units are stacked along the crystallographic c-axis. The stacking induces a tetragonal distortion that breaks the inversion symmetry inherent in the parent cubic structure, which not only affects the electronic structure and optical transitions but also enhances nonlinear optical and piezoelectric properties key for optoelectronic and photovoltaic applications. This symmetry-breaking also modifies the selection rules for electronic transitions, thereby improving the material's light-matter interaction efficiency, a crucial factor in solar energy conversion.

In the present theoretical investigation, we employed a 16-atom tetragonal unit cell, classified under the space group $I\bar{4}2d$, to model the parent compound $CuInSe_2$. To simulate sulfur doping and explore its effect on material properties, selenium atoms were partially substituted by sulfur atoms at defined anion lattice sites. This substitution strategy allows for systematic tuning of the anion sublattice and thereby modifies both the structural parameters and the electronic band structure. Six compositions were studied in detail, corresponding to sulfur concentrations of $x = 0, 0.2, 0.4, 0.6, 0.8$, and 1.0, covering the full compositional range from pure $CuInSe_2$ to pure $CuInS_2$. This compositional gradient enables band gap engineering through anion substitution, a method frequently employed to optimize the absorption edge of absorber materials to match the solar spectrum.

To investigate the structural, electronic, and optical behavior of these compounds across varying sulfur contents, we performed first-principles calculations grounded in Density Functional Theory (DFT) [20], a widely used quantum mechanical framework capable of accurately predicting the ground-state properties of complex crystalline systems. Geometry optimizations were conducted to minimize the total energy and identify the most energetically favorable atomic configurations for each sulfur concentration. These optimizations yielded equilibrium lattice constants, atomic positions, and deformation trends associated with sulfur incorporation.

All simulations were conducted using the CASTEP (Cambridge Sequential Total Energy Package) module, integrated within the Materials Studio platform. CASTEP employs a plane-wave basis set, suitable for periodic systems, and incorporates advanced numerical techniques to solve the Kohn–Sham equations. The interactions between valence electrons and ionic cores were described using norm-conserving pseudopotentials [21], chosen for their balance between computational efficiency and physical accuracy. These pseudopotentials ensure that the pseudo-wavefunctions retain the correct behavior outside the core region, making them well-suited for detailed electronic structure analysis.

For the exchange-correlation energy, we used the Generalized Gradient Approximation (GGA), specifically the Perdew–Burke–Ernzerhof (PBE) functional [16]. Compared to the Local Density Approximation (LDA), the GGA-PBE functional incorporates gradient corrections that account for spatial inhomogeneities in the electron density. This results in improved accuracy in predicting structural parameters, band gaps, and total energies, especially for systems involving light elements and semiconductors.

To ensure convergence and reliability of the calculated quantities, a Monkhorst–Pack [22] k-point mesh of 9 × 9 × 5 was adopted for Brillouin zone integration. Furthermore, a high kinetic energy cutoff of 900 eV was applied to truncate the plane-wave basis set, ensuring numerical precision and stability across all doping levels. This rigorous computational setup enabled the evaluation of a comprehensive set of physical properties, including but not limited to: lattice constants, bulk modulus, pressure derivatives, band structures, energy gap values, total and projected electronic densities of states (TDOS and PDOS), and several optical parameters such as the complex dielectric function, refractive index, reflectivity, and absorption coefficient. These descriptors collectively provide a holistic picture of how sulfur doping modulates the fundamental behavior of $CuIn(Se_{1-x}S_x)_2$.

The valence electronic configurations used for the constituent atoms were as follows: Cu: $3d^{10}$ $4s^1$, In: $4d^{10}$ $5s^2$ $5p^1$, Se: $4s^2$ $4p^4$, and S: $3s^2$ $3p^4$. These configurations were selected to capture the essential physics of bonding and electronic transitions within the material, particularly the hybridization between Cu–d and chalcogen–p orbitals, which plays a central role in determining the band structure and optical absorption behavior.

Through this methodology, the study offers an in-depth understanding of the impact of sulfur incorporation on the structural stability, band gap tuning, and optical performance of $CuIn(Se_{1-x}S_x)_2$, thereby reinforcing its potential as a customizable material platform for high-efficiency photovoltaic applications.

III.2.2 Convergence Parameters Selection: Cut-off Energy and Nk Point

The initial and crucial step in first-principles calculations, particularly those based on Density Functional Theory (DFT) using the Plane-Wave Pseudopotential (PP-PW) method with Norm-Conserving Pseudopotentials, involves selecting a suitable basis set for representing the electronic wave functions and carefully determining key input parameters. These parameters directly impact both the accuracy of the simulation results and the computational resources required. Therefore, it is essential to conduct systematic convergence tests to ensure that the results are physically meaningful, numerically stable, and reproducible.

Two main parameters require careful optimization to accurately model the studied system: (1) the cut-off energy (E_cutoff), which sets the upper limit for the kinetic energy of the plane waves used to build the basis set, and (2) the density of the k-point mesh (N kpt), which defines how finely the reciprocal space specifically the irreducible Brillouin zone is sampled for integration over electronic states. The cut-off energy controls the completeness of the plane-wave basis expansion; a higher cut-off energy includes more plane waves, enabling a more precise description of the Kohn-Sham orbitals, but at the cost of increased computational demand. On the other hand, choosing too low a cut-off energy risks inadequate wave function representation, which leads to errors in total energies and forces.

The number and distribution of k-points influence the sampling resolution of the reciprocal space and are critical for accurately computing properties sensitive to electronic structure, such as total energy, charge density, band structure, and density of states. To perform the Brillouin zone integration needed for summing over occupied states, discrete special k-points are selected. Crystal symmetry operations help reduce the number of irreducible k-points, thus optimizing computational efficiency without sacrificing accuracy. The Kohn-Sham equations are then solved in reciprocal space at these discrete points, with orbitals expanded as linear combinations of plane waves.

Although this plane-wave expansion is mathematically exact only in the limit of an infinite basis set, practical computations require truncation, achieved by imposing the cut-off energy. Convergence is considered reached when increasing either the cut-off energy or k-point density leads to negligible changes in total energy, indicating that the physical quantities calculated are no longer dependent on the basis set size or sampling density but represent true ground-state properties.

For the $CuIn(Se_{1-x}S_x)_2$ compound, convergence tests were performed by varying the cut-off energy from 200 eV up to 1100 eV while employing a fixed Monkhorst-Pack k-point grid of 9 × 9 × 5 for Brillouin zone sampling. This k-point grid was chosen based on previous experience with similar chalcopyrite semiconductors, balancing computational efficiency with accuracy. The total energy values obtained demonstrated a clear plateau around 900 eV, indicating convergence. Consequently, 900 eV was selected as the optimal cut-off energy for all subsequent calculations.

This choice guarantees an adequately large and accurate basis set to capture essential wave function features, enabling reliable predictions of structural properties such as lattice constants and bulk modulus and electronic properties, including band gaps and density of states, across various sulfur concentrations. Moreover, this consistent computational setup allows meaningful comparison between different compositions, ensuring that observed trends are genuinely due to material modifications rather than numerical artifacts.

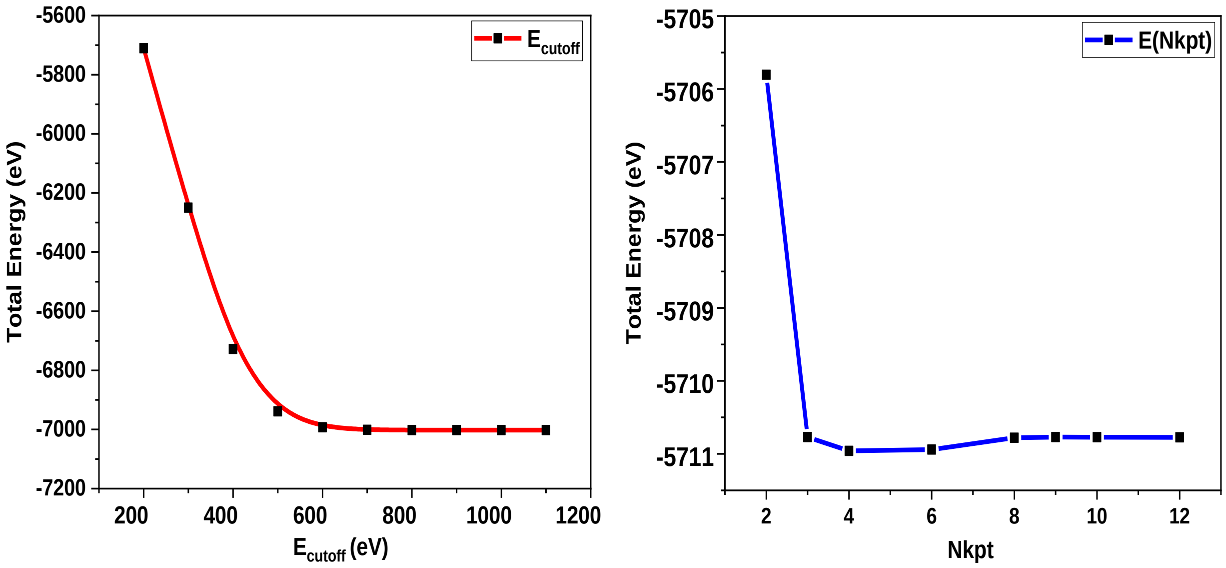

Figure III.1 Total energy as a function of the cut-off energy E_{cutoff} and of k-points "Nkpt".

III.3. Structural Properties

$CuInSe_2$ crystallizes in the well-known chalcopyrite structure, a tetragonal crystal system characterized by a specific ordered arrangement of copper, indium, and selenium atoms, as illustrated in Figure III.2. This structure is notable for its importance in semiconductor materials, particularly in photovoltaic applications, due to its favorable electronic and optical properties. Importantly, when $CuInSe_2$ is doped with sulfur atoms, the material retains the same chalcopyrite crystalline framework, demonstrating a high degree of structural stability and robustness. In this doped form, sulfur atoms substitute selenium atoms in the lattice sites without causing any significant change or disruption to the fundamental crystal symmetry or space group. This substitutional doping is possible because sulfur and selenium are chemically similar chalcogen elements, though they differ slightly in ionic radius and electronegativity. Consequently, the ability of sulfur to replace selenium within the chalcopyrite lattice allows for the tuning of various physical properties of $CuIn(Se_{1-x}S_x)_2$ compounds, such as band gap energy and lattice parameters, without compromising the overall structural integrity. This structural persistence upon doping is a critical factor for the practical utilization of these materials in optoelectronic devices, as it ensures predictable and controllable modification of their electronic and mechanical properties while maintaining a stable crystalline framework.

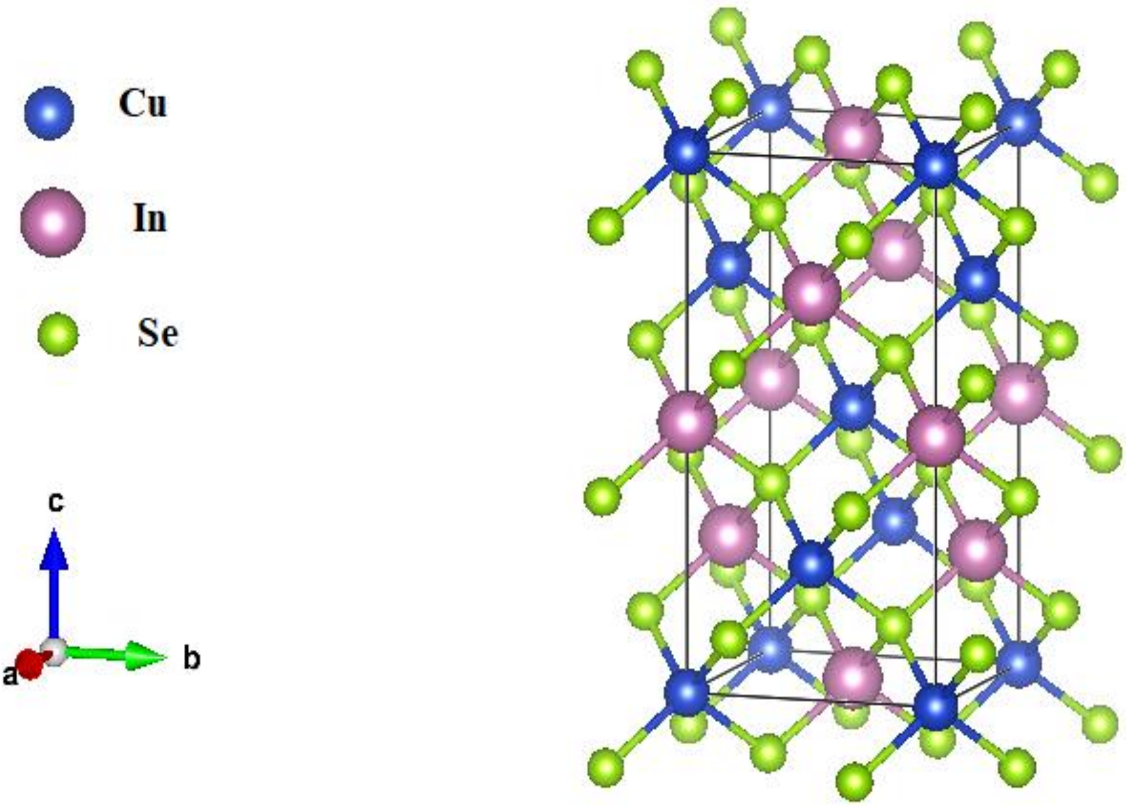

Figure III.2 Graphical presentation in 3D of chalcopyrites $CuInSe_2$

The structural properties of the $CuIn(Se_{1-x}S_x)_2$ compounds, including the equilibrium lattice constants (a and c), the bulk modulus (B), and its first pressure derivative (B'), were thoroughly investigated using Murnaghan's equation of state [23]. This equation relates the total energy of the system to its volume, and was fitted to the energy versus volume curves obtained from density functional theory (DFT) calculations within the generalized gradient approximation (GGA-PBE). The structural optimizations were performed at various pressures, as illustrated in Figure III.3, to analyze how the crystal structure responds under compression. Murnaghan's equation is given by:

$$E(V) = E_0 + \left[\frac{B_0 V}{B'(B'-1)}\right].\left[B'\left(1-\frac{V_0}{V}\right)+\left(\frac{V_0}{V}\right)^{B'}-1\right] \qquad (1)$$

where E_0 is the total energy at the equilibrium volume V_0 , B_0 is the bulk modulus at zero pressure, and ${B_0}'$ is the first pressure derivative of the bulk modulus. This equation effectively captures the variation of total energy with volume and allows extraction of important mechanical properties such as compressibility and stiffness of the material. The pressure derivative of the bulk modulus

$$B_0' = \frac{\partial B}{\partial p} \qquad (2)$$

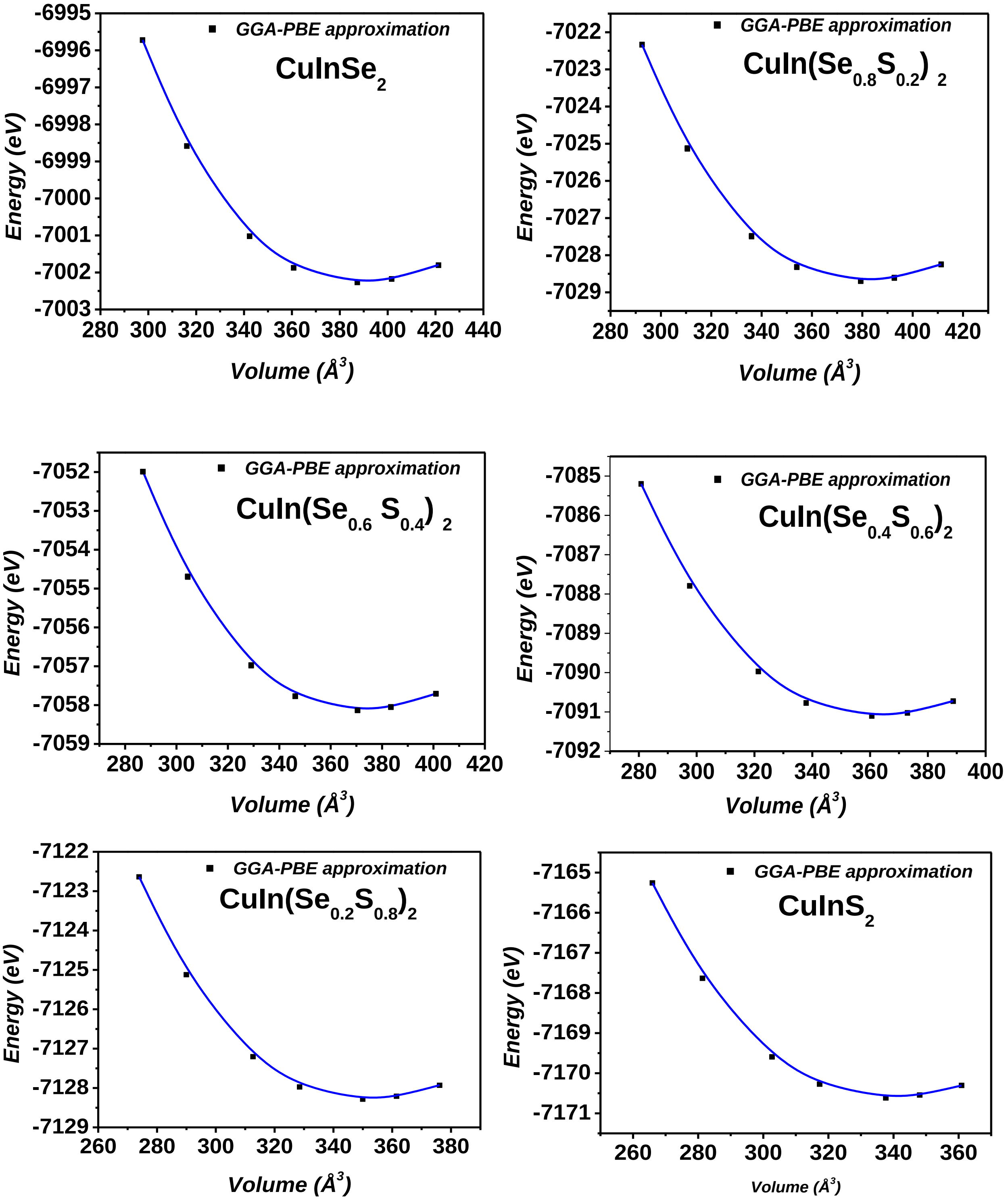

Figure III.3 Calculated total energy as a function of unit cell volume for chalcopyrite $CuIn(Se_{1-x}S_x)_2$.

The results of the optimized structural parameters for the $CuIn(Se_{1-x}S_x)_2$ compounds are presented in Table III.1. A clear trend is observed: as the sulfur (S) concentration increases, the lattice constants a and c exhibit a consistent decrease. This behavior can be attributed to the size disparity between the substituting anions. Specifically, the effective ionic radius of the sulfide ion S^{2-} is approximately 1.70 Å, which is smaller than that of the selenide ion Se^{2-}, approximately 1.84 Å [24]. Consequently, when selenium atoms are progressively replaced by sulfur atoms in the crystal lattice, a reduction in the unit cell dimensions naturally occurs due to the smaller ionic size of sulfur, which leads to a tighter packing of atoms.

This structural contraction with increasing sulfur content is not only consistent with theoretical expectations based on ionic radii, but also corroborated by our first-principles calculations. Moreover, the calculated lattice constants obtained within the GGA-PBE approximation show very good agreement with both experimental measurements and previous theoretical studies reported in the literature for the $CuIn(Se_{1-x}S_x)_2$ system. These findings reinforce the reliability of our computational approach and confirm the structural stability of the chalcopyrite phase across the entire compositional range from x = 0 to x = 1. Importantly, this contraction in lattice dimensions influences the mechanical properties of the material, such as its stiffness and compressibility, which are critical for practical applications.

Table III.1. Crystal structure parameters of $CuIn(Se_{1-x}S_x)_2$ compounds.

Compound	a(Å)	c(Å)	c/a	B_0(GPa	B_0
$CuInSe_2$ [46]	5.802	11.504	1.982	58.752	4.40
Expt. [25]	5.780	11.55	1.998		
Expt. [31]	5.814	11.63	2.0003		
Theo. [25]	5.862	11.792	2.012		
Theo. [26]	5.8455	11.683	1.998		
Theo. [28]	5.817	11.743	2,018	54.56	4.89
Theo. [29]	5.883	11.842	2.013	54.200	
$CuIn(Se_{0.8}S_{0.2})_2$ [46]	5.761	11.427	1.983	62.497	4.36
$CuIn(Se_{0.6}S_{0.4})_2$ [46]	5.717	11.334	1.982	64,257	4.361
$CuIn(Se_{0.4}S_{0.6})_2$ [46]	5.664	11.237	1,983	66,788	4.21
$CuIn(Se_{0.2}S_{0.8})_2$ [46]	5.607	11.130	1.983	69,233	4.21
$CuInS_2$ [46]	5.538	11.007	1.987	70,769	4.32
Expt. [25]	5.520	11.080	2.007		
Expt. [28]	5.574	11.248	2.017	65.81	4.80
Expt. [32]	5.561 ±0.002	11.116 ±0.007		75 ± 5	4.00
Expt. [30]	5.517	11.122	2.015		
Theo. [25]	5.576	11.251	2.018		
Theo. [26]	5.5734	11.228	2.02		
Theo. [27]	5.592	11.285	2.018	68.7	3.57
Theo. [29]	5.598	11.277	2.014	65.547	

Regarding the bulk modulus B_0, there is a noticeable increase with rising sulfur content, from approximately 58.75 GPa for $CuInSe_2$ to about 70.77 GPa for $CuInS_2$. This increase signifies a higher stiffness and reduced compressibility of the material due to stronger atomic bonding within the more compact lattice created by the smaller S ions. The first pressure derivative of the bulk modulus B_0' remains fairly stable around 4.3 to 4.4 across compositions, suggesting a consistent manner in which the stiffness changes with applied pressure, in agreement with values reported in prior works as shown in the Table III.1.

The energy versus volume plots (Figure III.4) reinforce these findings by showing smooth, well-defined curves where energy decreases as volume contracts until reaching a minimum at the equilibrium volume, after which energy rises sharply under further compression, indicating structural stability. The gradual shift of this minimum towards smaller volumes with increasing sulfur content visually confirms the lattice contraction trend observed in the tabulated data.

In summary, this study, through detailed theoretical calculations and structural analysis, validates the accuracy of the measured properties of $CuIn(Se_{1-x}S_x)_2$ compounds. It demonstrates that substituting sulfur for selenium leads to a reduction in lattice dimensions and an increase in material stiffness, while maintaining the structural integrity of the chalcopyrite phase. These insights are critical for understanding how chemical composition influences material properties, with important implications for their application in photovoltaic devices and electronic components.

III.4. Electronic Properties

Analyzing the band structure is a crucial step in understanding the fundamental physical properties of materials. It provides valuable insights into key characteristics such as the spectral distribution of optical absorption, the spatial distribution of charge density, and the mobilities of electrons and holes parameters that directly influence the performance of semiconductor devices. In this study, we present the calculated energy band structures of $CuIn(Se_{1-x}S_x)_2$ compounds along multiple high-symmetry directions in the Brillouin zone, accompanied by their corresponding density of states (DOS) profiles, As seen in Figure III.4. These band structures clearly exhibit a direct band gap nature across all compositions examined.

It is important to emphasize that the band gap values obtained from our theoretical calculations differ quantitatively from those measured experimentally. This discrepancy arises primarily from the use of the generalized gradient approximation (GGA) within the framework of density functional theory (DFT) to approximate the exchange-correlation potential. While GGA provides a reasonable balance between computational efficiency and accuracy, it is well-known to systematically underestimate the band gap values of semiconductors due to its approximate treatment of electron-electron interactions.

Our results encompass a range of sulfur concentrations, with x varying from 0 to 1 in increments of 0.2, allowing us to systematically investigate the impact of S substitution on the electronic structure of the material. Throughout this series, the Fermi level ‘indicated by dashed lines in the plots’ is consistently set to zero to provide a uniform reference. Notably, the calculated band gap exhibits a clear trend of increasing magnitude with higher sulfur content, which aligns well with experimental observations. This increase can be attributed to the difference in electronic structure and bonding characteristics between selenium and sulfur atoms, where sulfur’s higher electronegativity and smaller atomic radius result in a wider band gap.

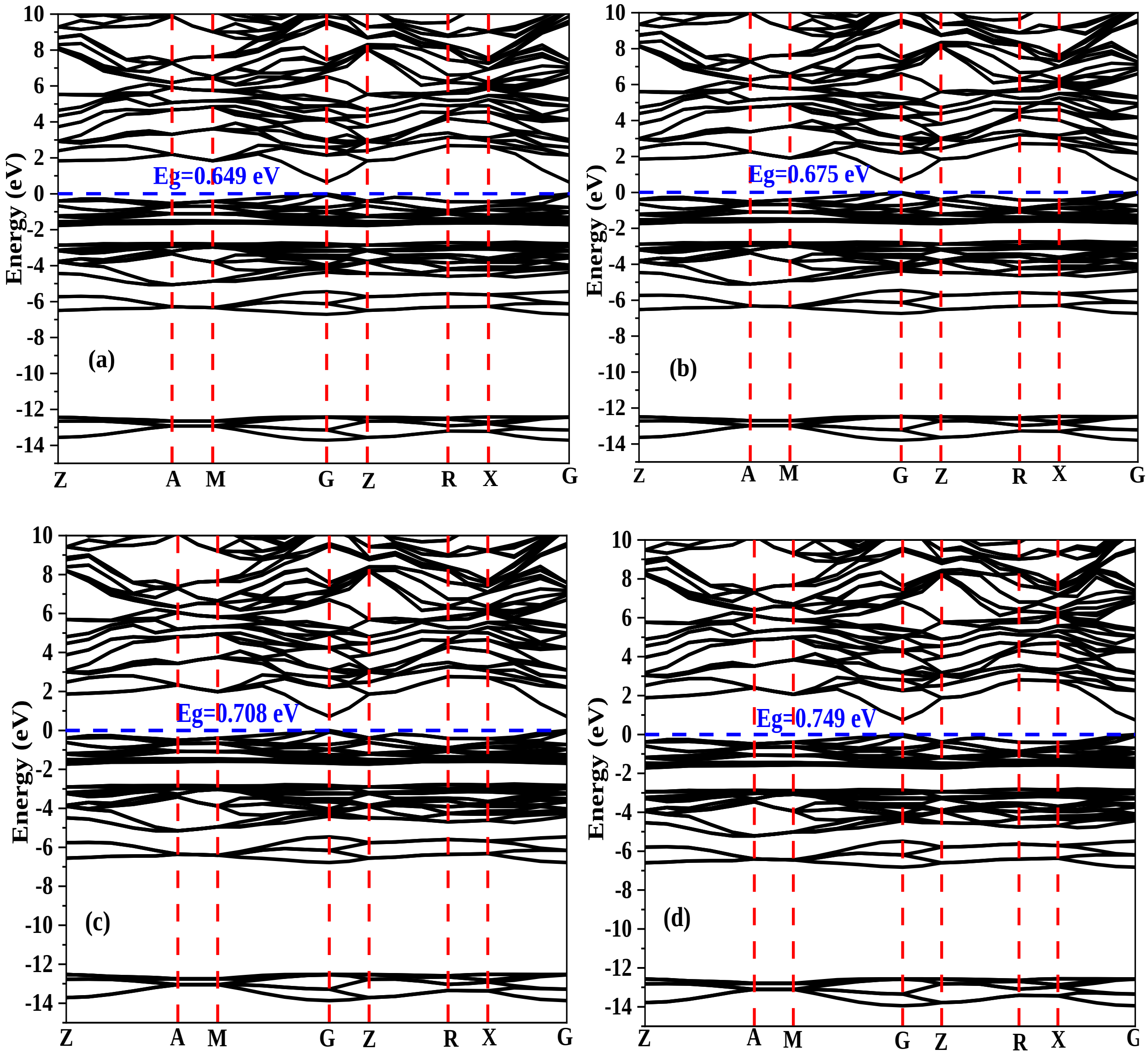

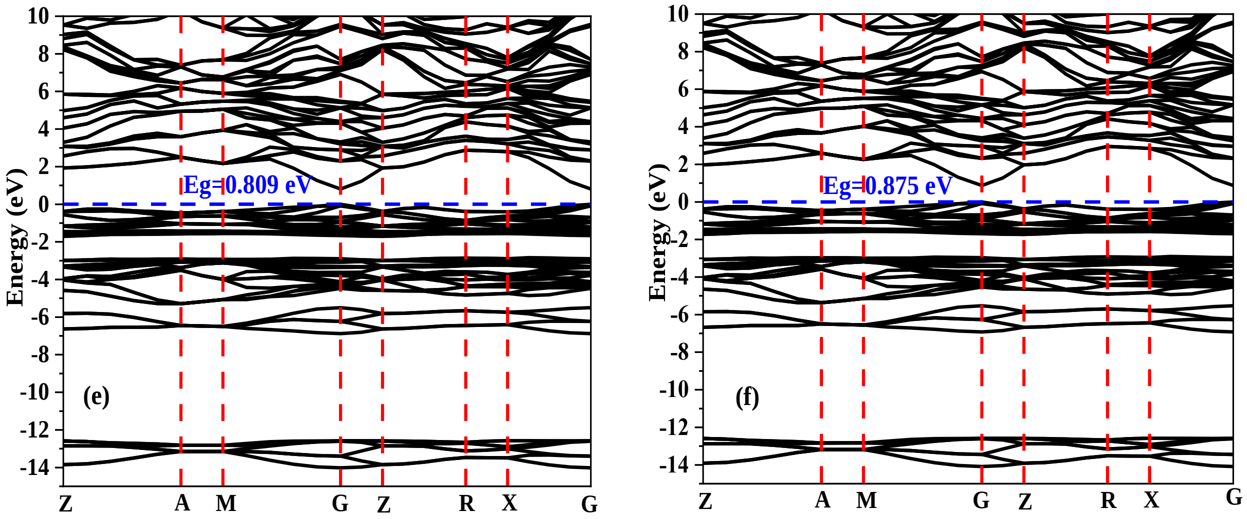

Figure III.4 Band structure curves for chalcopyrite CuIn $(Se_{1-x}S_x)_2$ ((a) x =0, (b) x =0.2, (c) x =0.4, (d) x =0.6, (e) x =0.8, (f) x =1), with GGA approximation.

The valence band of all $CuIn(Se_{1-x}S_x)_2$ compounds consist of three distinct sub-bands, as clearly demonstrated by the total density of states (DOS) diagrams. The highest valence sub-band extends from the Fermi level, set at 0 eV, down to approximately 2 eV below it. This upper valence band is primarily formed through the hybridization of Cu-d orbitals and Se-p orbitals in $CuInSe_2$. In contrast, for $CuInS_2$, the hybridization occurs between Cu-d orbitals and S-p orbitals due to the substitution of selenium by sulfur, which alters the electronic environment subtly but significantly. The lowest valence sub-band, located between approximately -12 eV and -14 eV, is mainly derived from Se-s orbitals with minor contributions from In-s and In-p orbitals. This deep energy sub-band reflects the core-like character of the Se-s states. Meanwhile, the middle valence sub-band, ranging from around -3 eV to -7 eV, results from the hybridization between Se-p orbitals and In-s and In-p orbitals. This interplay of orbitals contributes to the complex electronic structure within the valence band, influencing the optical and transport properties of the material.

The Fermi level is fixed at 0 eV throughout the analysis, providing a common reference point. The conduction band, on the other hand, is predominantly composed of states from Cu-p, Se-p, In-s, and In-p orbitals, as shown in Figure III.4 and Figure III.5 This reflects the involvement of both copper and indium orbitals, along with chalcogen p-orbitals, in defining the conduction band characteristics.

For $CuInSe_2$, the total density of states (DOS) closely resembles that of $CuInS_2$, with the principal difference being the progressive replacement of Se-p and Se-s states by S-p and S-s states as the sulfur concentration xxx increases in $CuIn(Se_{1-x}S_x)_2$. This substitution modifies the electronic structure gradually, reflecting the change in chemical composition.

Furthermore, Figure III.4 illustrates a notable upward shift in the position of the Conduction Band Minimum (CBM) as Se atoms are replaced by S atoms. This shift can be attributed to the higher energy levels of sulfur orbitals compared to selenium, which effectively raises the conduction band edge. This phenomenon is considered the primary mechanism responsible for the observed increase in the band gap energy with increasing sulfur content.

The dependence of the energy band gap Eg on sulfur concentration x is nonlinear and can be accurately modeled by the following quadratic equation: $Eg(x)= 0.650 + 0.096x + 0.129x^2$
Finally, both the total density of states (DOS) and partial density of states (PDOS) for $CuIn(Se_{1-x}S_x)_2$ with six different sulfur concentrations are presented in Figure III.5. The PDOS analysis provides a detailed breakdown of the contribution of individual atomic orbitals to the overall electronic states, offering insight into how specific substitutions influence the band structure and electronic properties.

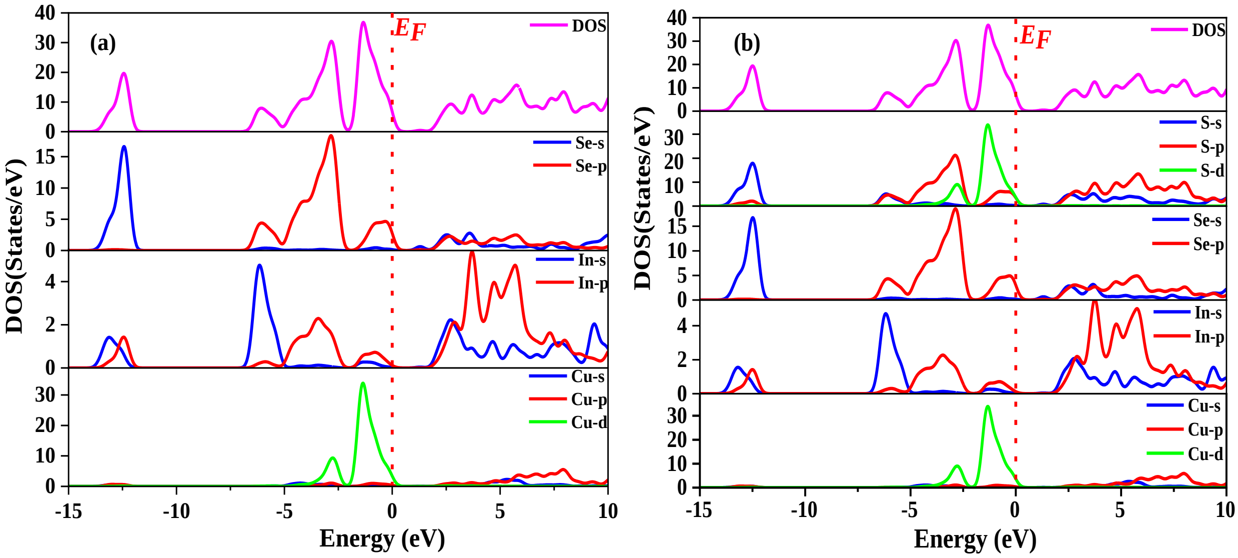

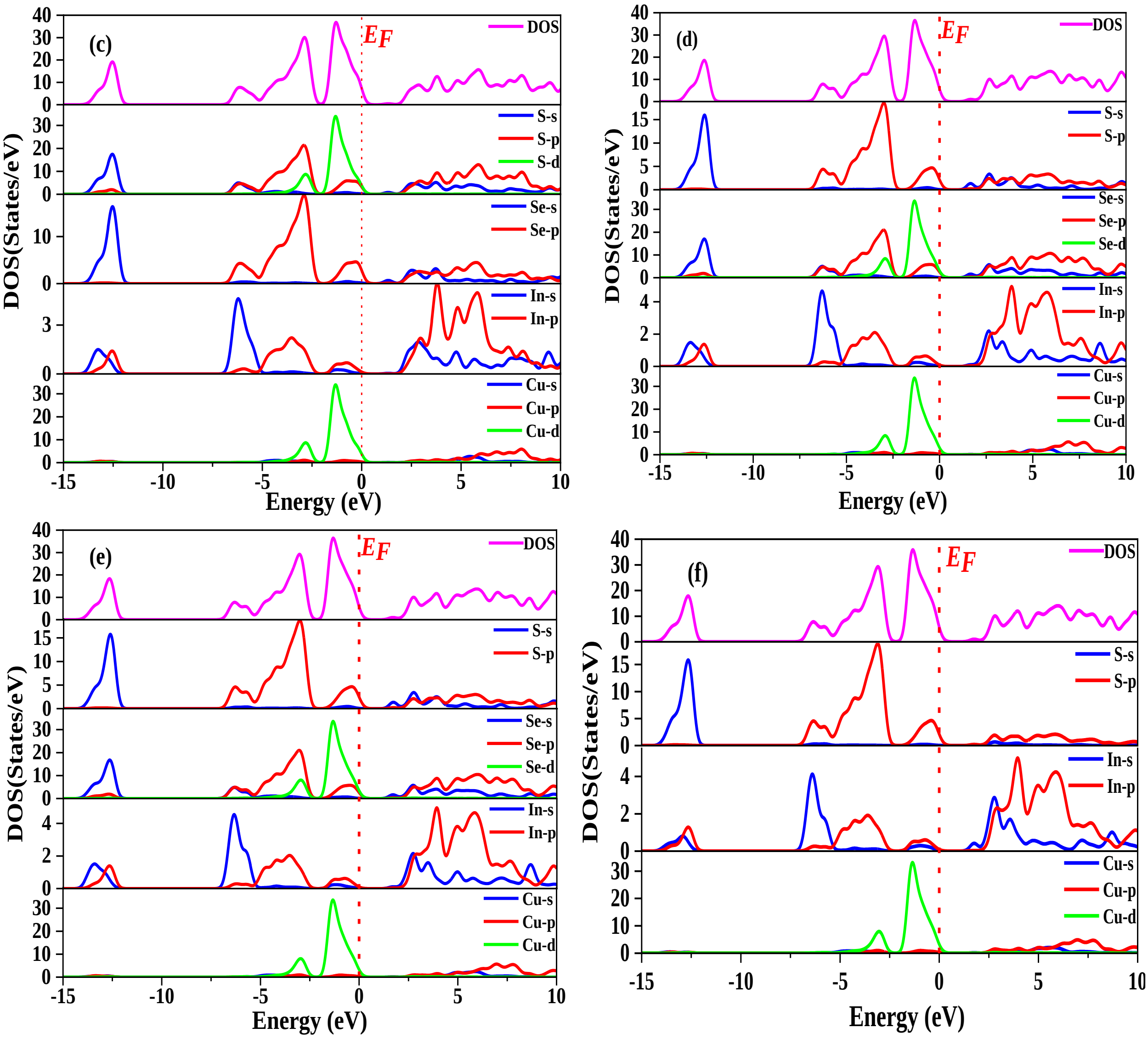

Figure III.5. DOS and PDOS for chalcopyrite CuIn (Se$_{1-x}$S$_x$)$_2$ ((a) x =0, (b) x =0.2, (c) x =0.4,(d) x =0.6, (e) x =0.8, (f) x =1), with GGA approximation.

Table III.2. Calculated Band Gap (Eg) within GGA approximations of chalcopyrite CuIn(Se$_{1-x}$S$_x$)$_2$ compound, compared with experimental and other theoretical works.

Materials	Eg	Eg	Eg
	Present work	Expt.	Theo.
CuInSe$_2$	0.649	1 [34] 0.98 [33]	1.07 [24] 0.8 [34]
CuIn(Se$_{0.8}$S$_{0.2}$)$_2$	0.675		
CuIn(Se$_{0.6}$S$_{0.4}$)$_2$	0.708		
CuIn(Se$_{0.4}$S$_{0.6}$)$_2$	0.749		
CuIn(Se$_{0.2}$S$_{0.8}$)$_2$	0.809		
CuInS$_2$	0.875	1.43 [30]	1.384 [24] 0.821 [34]

III.5. Optical Properties

The analysis of a material's optical spectrum is considered an effective and essential tool for understanding the electronic and physical behaviour of solids. It allows for the examination of interactions between matter and electromagnetic radiation through various techniques, including absorption, reflection, and light emission. These techniques are particularly important when dealing with semiconducting materials, as they provide accurate data on the energy bandgap, the distribution of electronic states, and the material’s response to radiation—critical parameters for the development of advanced electronic and optical applications.

In this context, ternary chalcopyrite semiconductors, such as the $CuIn(Se_{1-x}S_x)_2$ compound, exhibit unique optical characteristics due to their complex crystal structure and diverse electronic interactions. This makes them promising candidates in several fields, including solar cell technology, photodetectors, and laser systems. The significance of this study lies in its theoretical analysis of the optical properties of this compound using computational methods grounded in first principles, ensuring accurate and reliable results when compared with experimental data.

The Generalized Gradient Approximation (GGA), a widely used functional within Density Functional Theory (DFT), was employed to compute the optical properties of the compound for two limiting values of x ($x = 0$ and $x = 1$), representing the two end-members of the alloy. The calculations included the complex dielectric function, optical conductivity, refractive index, reflectivity, and absorption coefficient. These were carried out with the aim of determining the optimal energy bandgap values, which are crucial for evaluating the performance of semiconductors in photovoltaic and optoelectronic applications.

Furthermore, the optical dielectric constant, static reflectivity, and static refractive index of the $CuIn(Se_{1-x}S_x)_2$ compound were calculated and compared with both experimental findings and previously published theoretical results [35, 36]. This comparative analysis highlights areas of agreement or discrepancy, thereby enhancing the reliability of the adopted methodology and guiding future studies toward more accurate predictions of the optical behaviour of such complex materials.

III.5.1 Dielectric Function

The dielectric functions of $CuIn\,(Se_{1-x}S_x)_2$ (x=0;1), which are materials used in thin-film solar cells, are important for understanding their optical and electrical properties. The dielectric function describes how these materials interact with electromagnetic radiations including light. The dielectric function of these materials typically consists of two main parts: the real part (ε_1) and the imaginary part (ε_2). The complex dielectric function $\varepsilon(\omega)$ of semiconductor materials given by:

$\varepsilon(\omega)=\varepsilon_{real}(\omega)+i\varepsilon_{imaginary}(\omega)$ can help to calculate other optical parameters such as the absorption coefficient α(ω), refractive index n(ω) and reflectivity R(ω). Imaginary part of the dielectric function is given ask

$$\varepsilon_{\alpha\beta}^{(2)}(\omega)=\frac{4\pi^2e^2}{\Omega}\lim_{q\to 0}\frac{1}{q^2}\sum\nolimits_{c,v,k}2w_k\delta(\varepsilon_{ck}-\varepsilon_{vk}\ -\omega)\times\langle u_{ck}+e_{\alpha q}|\,u_{vk}\rangle\langle u_{ck}+e_{\beta q}|\,u_{vk}\rangle * \quad (3)$$

u_{ck} is the cell periodic component of the wave function at the k-point k, e_α and e_β are unit vectors for the three Cartesian directions, and **c** and **v** are the indices of the conduction and valence band states, respectively. The Kramers–Kronig bidirectional mathematical relation connects the imaginary and real parts of any complex function that is analytic in the upper half-plane. The real part of the dielectric function can be obtained from the imaginary part using this relation according to [37,38]

$$\varepsilon_{\alpha\beta}^{(1)}(\omega)=\ 1\ \frac{2}{\pi}P\int_0^\infty\frac{\varepsilon_{\alpha\beta}^{(2)}(\omega\prime)\omega\prime}{\omega\prime^2-\omega^2+i\eta}\ d\omega' \quad (4)$$

Where the principal value is represented by P. In the Kramers–Kronig transformation [39] a small complex shift η is used. In our calculations η is set to be 0.1 eV. Knowledge of both the real and imaginary parts of the dielectric function can help in calculating other optical properties.

The optical properties were examined under two types of polarizations: ordinary along the x and y directions (E// (100)) and extraordinary along the z direction (E// (001)).

Figure III.6. illustrates the plots of the real part of the dielectric function in relation to photon energy for $CuIn(Se_{1-x}S_x)_2$ (x=0;1), covering a range of 0 to 20 eV. The zero-frequency limit $\varepsilon_1(0)$ is a significant quantity actually governed by the band gap of the material. The computed values of $\varepsilon_1(0)$ using GGA-PBE approximation are listed in Table III.3 which are in good agreement with theoretical and experimental results obtained under ordinary and extraordinary polarization for both chalcopyrite compounds. The imaginary part of the dielectric function, $\varepsilon_2(\omega)$, indicates the optical response of a material and offers essential information regarding the inter-band electronic transitions occurring between the valence and conduction bands. These transitions occur when photons with sufficient energy excite electrons from occupied states in the valence band to unoccupied states in the conduction band, influencing the material's optical absorption properties. The results obtained align with the theoretical curves and the experimental data documented in the referenced sources [40- 42].

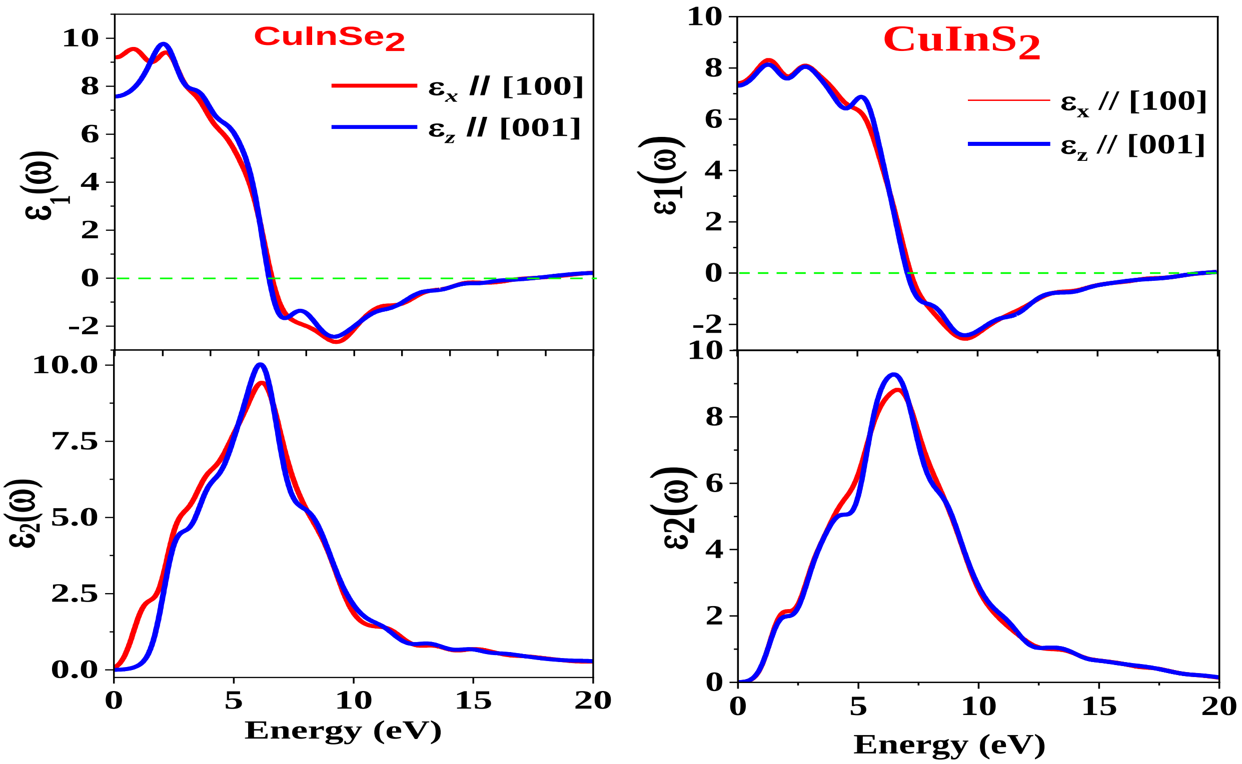

Figure III.6. Real and Imaginary part of dielectric function for chalcopyrite CuInSe$_2$ and CuInS$_2$ compound.

The dielectric functions of CuInSe$_2$ (x = 0) and CuInS$_2$ (x = 1) provide critical insights into their optical behaviour and underscore their high potential for advanced photovoltaic applications. For CuInSe$_2$, the real part of the dielectric function $\varepsilon_1(\omega)$ exhibits a prominent peak near 6 eV, indicating strong refractive characteristics within this energy domain. This peak suggests that incident light is highly concentrated and effectively interacts with the material's electronic structure at this energy level. As the photon energy increases beyond approximately 10 eV, $\varepsilon_1(\omega)$ crosses the zero line, marking the plasma frequency, a threshold beyond which the material's optical response shifts from absorptive to reflective. This transition is key to understanding the depth of light penetration and optical losses at high energies. Additionally, the imaginary part $\varepsilon_2(\omega)$ displays a sharp and intense peak around 4 eV, attributed to strong inter-band electronic transitions where photons promote electrons from the valence to conduction band. This absorption capability is essential for generating electron-hole pairs, a fundamental process in solar energy conversion. In contrast, CuInS$_2$ demonstrates a similar but slightly shifted optical behaviour. The real part $\varepsilon_1(\omega)$ peaks around 5.5 eV, indicating effective refractive properties at slightly lower photon energies. Its plasma frequency appears between 8 and 10 eV, suggesting a reflective transition occurring earlier than in CuInSe$_2$. The imaginary part $\varepsilon_2(\omega)$ shows a notable absorption peak at approximately

3.5 eV, slightly lower than that of $CuInSe_2$, indicating $CuInS_2$ strong capacity to absorb lower-energy (longer-wavelength) photons. This makes $CuInS_2$ particularly suitable for capturing the infrared portion of the solar spectrum, complementing $CuInSe_2$, which is more efficient in the visible and ultraviolet ranges. The combination of these two materials through compositional engineering in the form of CuIn $(Se_{1-x}S_x)_2$ allows for bandgap tuning and the creation of tandem or graded-bandgap solar cells. These hybrid structures can exploit a broader portion of the solar spectrum, enhancing light absorption, reducing thermalization losses, and significantly improving overall energy conversion efficiency.

Table III.3. Calculated optical dielectric constant, static reflectivity and static refractive index for the chalcopyrite CuIn $(Se_{1-x}S_x)_2$ compound, compared with experimental and other theoretical works.

Static parameters	$\varepsilon_1(0)$		R(0)		n(0)	
Materials	E//(100)	E//(001)	E//(100)	E//(001)	E//(100)	E//(001)
$CuInSe_2$ (x=0)	9.314	7.577	0.252	0.218	3.06	2.753
Ref [31]	8.95	8.44	0.25	0.24	2.99	2.90
Ref [32]					2.937	2.950
$CuInS_2$ (x=1)	7.422	7.340	0.227	0.213	2.728	2.709
Ref [22]	7.63				2.76	

III.5.2. Reflectivity

The reflectivity (R) of a material, which represents the fraction of incident light that is reflected from its surface, is a critical optical property for evaluating light–matter interaction and is especially relevant in the context of thin-film photovoltaic and optoelectronic materials. Reflectivity can be derived from the refractive index (n) and the extinction coefficient (k) using the equation:

$$R = \frac{(n-1)^2+k^2}{(n+1)^2+k^2} \qquad (5)$$

This relation assumes normal incidence of light from a vacuum onto a dielectric surface and provides an essential link between intrinsic material constants and measurable optical behaviour. The refractive index itself is defined as the ratio of the speed of light in vacuum to that in the material, indicating how much the light path is bent or slowed inside the medium. Using the GGA-PBE approximation, the calculated values of R(0) for $CuInSe_2$ and $CuInS_2$, presented in Table III.3, show a strong agreement with both theoretical models and experimental findings under different polarization modes (ordinary and extraordinary). As illustrated in Figure III.7, the reflectivity spectra of both compounds were evaluated across a wide photon energy range (0–20 eV). $CuInSe_2$ (x = 0) displays a distinct and stronger reflectivity in the low-energy region between 1 and 4 eV, which corresponds to increased photon–material interaction due to its smaller bandgap. This behaviour is advantageous in devices requiring effective light manipulation at lower energies. The high reflectivity in this region implies that a significant portion of incident light is reflected rather than absorbed, potentially influencing surface-level device design or anti-reflective layer needs. However, with the increase in sulfur content as the composition transitions toward $CuInS_2$ (x = 1), the reflectivity in the low-energy range decreases slightly. This is due to the wider bandgap of $CuInS_2$, which restricts the interaction with low-energy photons and renders the material more transparent in this region. Interestingly, the reflectivity of $CuInS_2$ becomes more pronounced and stable at higher photon energies (above 6 eV), where it begins to resemble the behaviour of $CuInSe_2$. This compensation effect at higher energies is significant, as it suggests that $CuInS_2$ maintains its reflective strength in ultraviolet regions, despite reduced low-energy reflectance. The shift in reflectivity patterns across the energy spectrum not only reflects the fundamental band structure differences between the two materials but also highlights their potential for complementary use in optoelectronic devices, where control over spectral reflectivity is essential for enhancing device performance, especially in multilayer or graded-bandgap solar cell architectures.

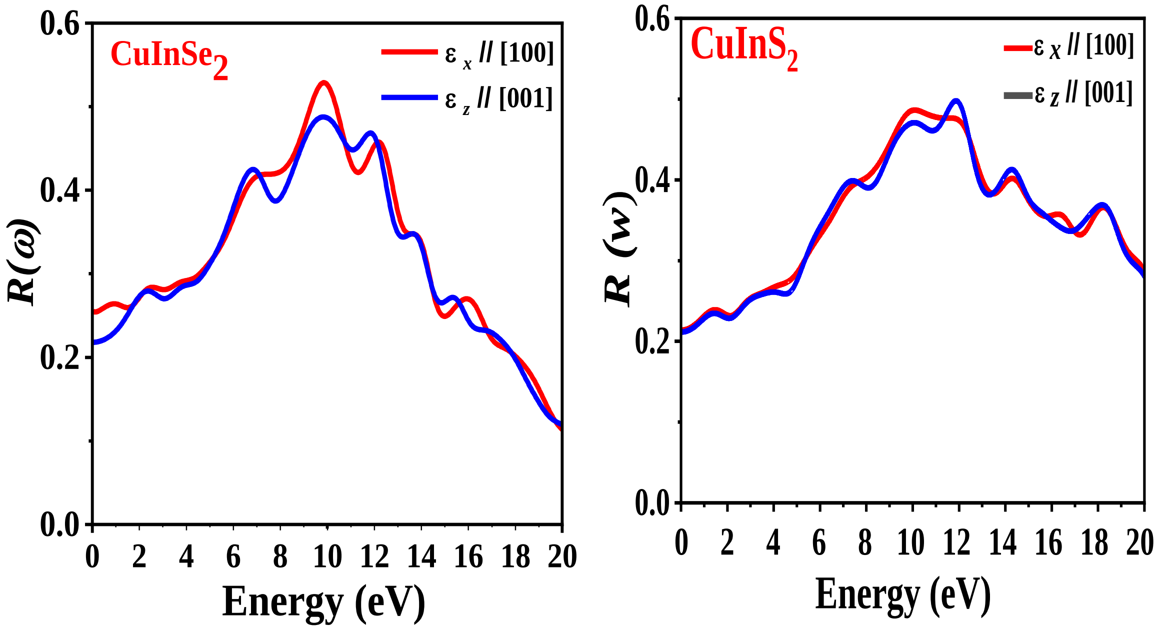

Figure III.7. Reflectivity Spectra of Chalcopyrite $CuInSe_2$ and $CuInS_2$ Compounds for Different Polarizations

III.4.3. Refractive and extinctive indexes

The complex refractive index N, which characterises how light propagates through a material, is composed of two components: the real part nnn, known as the refractive index, and the imaginary part k, known as the extinction coefficient. Mathematically, it is expressed as

$$n = \left(\frac{\sqrt{\varepsilon_1^2(\omega)+\varepsilon_2^2(\omega)}+\varepsilon_1}{2} \right)^{1/2} \quad (6)$$

$$k = \left(\frac{\sqrt{\varepsilon_1^2(\omega)+\varepsilon_2^2(\omega)}-\varepsilon_1}{2} \right)^{1/2} \quad (7)$$

Table III.3 highlights that the calculated zero-frequency refractive index values, n(0), for the $CuIn(Se_{1-x}S_x)_2$ system at x = 0 and x = 1, using the GGA-PBE approximation, are in strong agreement with both theoretical and experimental results obtained under ordinary and extraordinary polarization conditions. This consistency validates the accuracy and reliability of the computational approach.

Figure III.8 provides a spectral overview of the optical constant, namely the refractive index n(ω), for $CuInSe_2$ and $CuInS_2$ across the photon energy range of 0–20 eV. Notably, although both materials demonstrate convergence of optical properties at higher energies, their behavior diverges significantly in the low-energy region. $CuInSe_2$ exhibits a higher refractive index at photon energies below 3 eV, indicating enhanced light–matter interaction, increased optical density, and more pronounced light bending at these wavelengths. This characteristic is beneficial in applications requiring strong photon confinement and effective anti-reflection behavior. In contrast, $CuInS_2$ presents a lower refractive index in the same energy range, suggesting reduced interaction with low-energy photons, which can lead to improved light transmission through thin layers and reduced surface reflection losses.

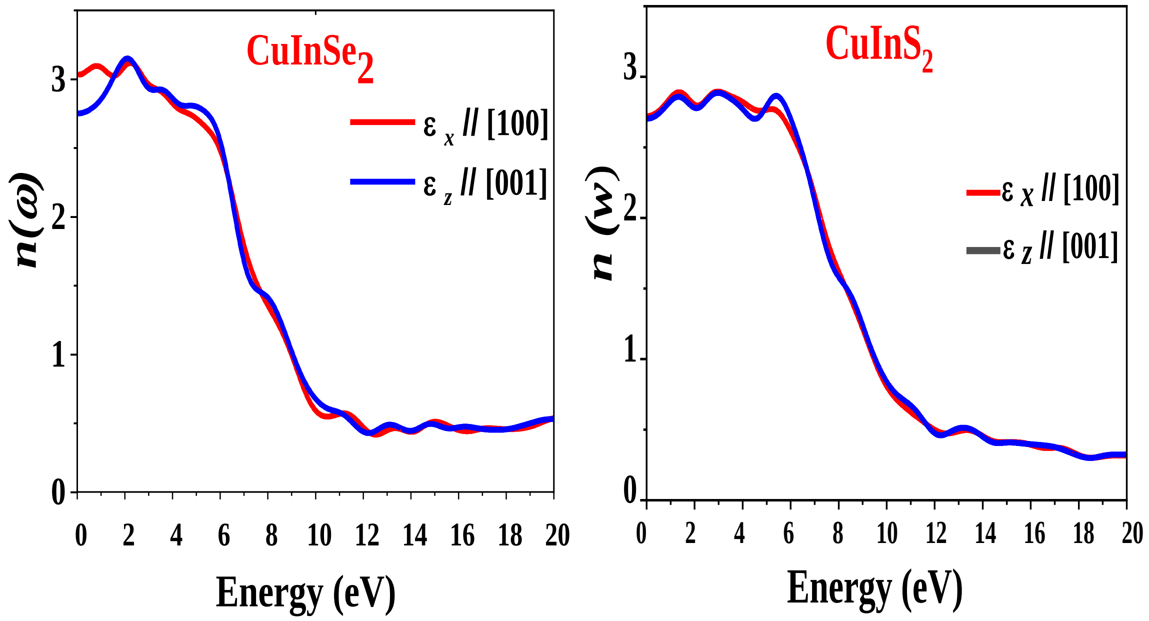

Figure III.8. Variation of Refractive Index with Photon Energy for $CuInSe_2$ and $CuInS_2$ Single Crystals in Different Polarization Directions

As for the extinction coefficient k(ω), Figure III.9 shows that $CuInSe_2$ displays higher values, particularly in the energy interval of approximately 2–6 eV, signifying robust light absorption due to interband electronic transitions. However, k(ω) decreases gradually beyond this range, reflecting diminished absorption losses in the ultraviolet spectrum. On the other hand, $CuInS_2$ maintains consistently lower k(ω) values across the entire spectral domain, indicating reduced energy dissipation and enhanced material transparency, especially in the visible range.

Importantly, sulfur doping in $CuIn(Se_{1-x}S_x)_2$ provides a powerful mechanism for tailoring the material's optical behavior. By modulating the Se/S ratio, it becomes possible to lower the refractive index n, thereby facilitating better light penetration at lower energies, and simultaneously adjust the extinction coefficient k to optimize transparency and absorption across different spectral regions. Such control enables precise engineering of the optical response for photovoltaic applications, where materials must efficiently absorb sunlight while minimizing reflection and non-radiative losses. This ability to fine-tune optical constants through composition makes the $CuIn(Se_{1-x}S_x)_2$ system highly attractive for the design of next-generation thin-film solar cells and optoelectronic devices that demand superior spectral response and energy conversion efficiency.

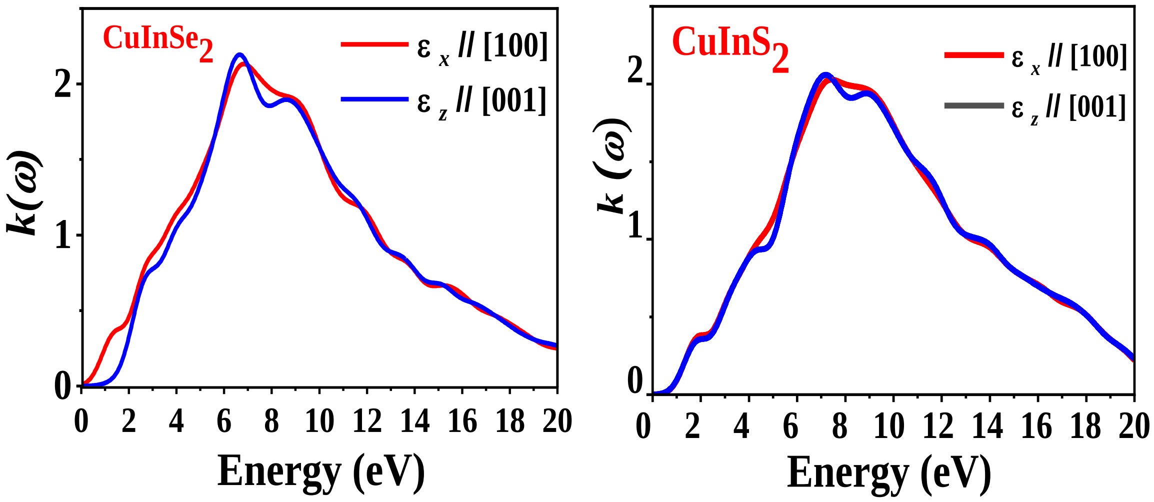

Figure III.9 Energy-Dependent Extinction Coefficient in $CuInSe_2$ and $CuInS_2$ Crystals for Various Polarization Orientations

III.4.4. Absorption Coefficient

The absorption coefficient $\alpha(\omega)$ determines how far light of a specific wavelength may enter a material before being absorbed. It can be calculated directly from the dielectric function using this formula [20]

$$\alpha(\omega) = \sqrt{2}\omega\left[\sqrt{\varepsilon_1^2(\omega) + \varepsilon_2^2(\omega)} - \varepsilon_1(\omega)\right]^{1/2} = 2\omega \quad (8)$$

Figure III.10 presents the absorption spectra of the $CuIn(Se_{1-x}S_x)_2$ material for two doping concentrations, x = 0 ($CuInSe_2$) and x = 1 ($CuInS_2$), offering valuable insight into its optical absorption behaviour and band structure. The absorption spectrum is a critical tool for estimating the optical band gap (Eg) of a semiconductor, as it reflects how the material responds to incident photons of varying energies. Absorption takes place when the photon energy (hν) surpasses the material's band gap, enabling electrons in the valence band to gain sufficient energy to transition to the conduction band. Conversely, when the photon energy is below the band gap, such transitions do not occur, and the material does not absorb the light, rendering it transparent in that spectral range. This optical transparency is evident in the spectra below the absorption edge. As the doping level of sulfur increases (i.e., as x increases), the absorption edge noticeably shifts toward higher photon energies, indicating an expansion of the band gap. This blue-shift in the edge reflects a material that requires more energetic photons for electron excitation, implying enhanced ability to absorb in the ultraviolet range. Notably, sharp increases in absorption, known as the absorption edge, become more prominent with increasing x, confirming the widening of Eg due to S-doping. In addition, the spectra exhibit distinct absorption peaks around 8 eV and 11 eV, whose positions and intensities vary with composition. These peaks are likely associated with interband transitions involving deeper energy levels and are strongly influenced by modifications in the electronic structure induced by the substitution of selenium with sulfur. At photon energies above 6 eV, the differences between $CuInSe_2$ and $CuInS_2$ become more apparent, which may be attributed to higher-order optical transitions that emerge due to changes in orbital hybridization and band dispersion caused by the increased sulfur content. Overall, the observed trends demonstrate that S-doping not only increases the band gap but also modifies the absorption profile significantly, making the material more responsive to high-energy photons. This tunability of the absorption edge and spectral response through compositional engineering positions $CuIn(Se_{1-x}S_x)_2$ as a promising candidate for advanced optoelectronic devices, particularly in photovoltaic applications where tailoring the band gap to match the solar spectrum is essential for optimizing energy conversion efficiency.

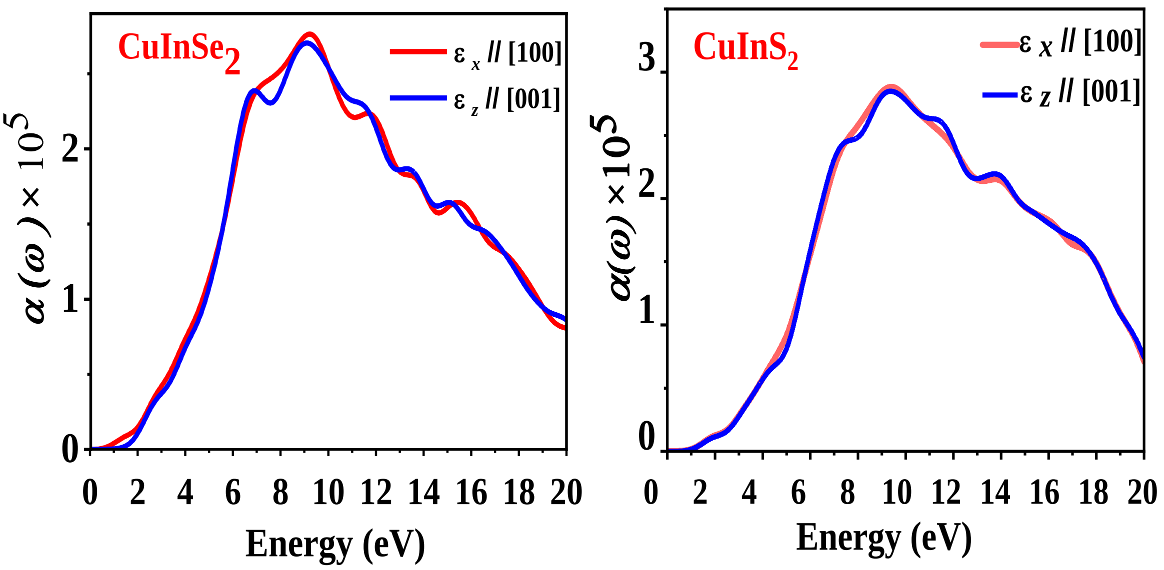

Figure III.10. Absorption Coefficient Spectra of $CuInSe_2$ and $CuInS_2$Crystals in Different Polarization Directions

III.4.5. Optical Conductivity

The optical conductivity σ(ω), which characterizes a material's ability to conduct electricity in response to incident electromagnetic radiation, provides critical insight into the interaction between light and electronic states. Figure III.11 highlights the variation of optical conductivity for the $CuIn(Se_{1-x}S_x)_2$ system, revealing distinct behaviours for the two end-member compounds $CuInSe_2$ ($x = 0$) and $CuInS_2$ ($x = 1$). The plot clearly shows that $CuInSe_2$ exhibits a higher and more pronounced optical conductivity peak in the lower photon energy range of approximately 3 to 6 eV. This indicates that $CuInSe_2$ possesses a stronger electronic response to low-energy photons, which is particularly important in applications such as near-infrared or visible light absorption. The enhanced conductivity in this energy window suggests efficient interband transitions and a higher density of available electronic states near the valence and conduction band edges. On the other hand, $CuInS_2$ shows its optical conductivity peak at slightly higher energies, around 4 to 7 eV, which corresponds to its wider bandgap. However, the peak magnitude is lower than that of $CuInSe_2$, indicating comparatively reduced optical response within this spectral range. This shift implies that $CuInS_2$ becomes more active in the higher-energy part of the spectrum, making it more suitable for devices operating in the ultraviolet or higher-frequency visible regions. The reduced optical conductivity of $CuInS_2$ at lower energies also supports its higher transparency and lower absorption in that range. Overall, the contrast in optical conductivity profiles between $CuInSe_2$ and $CuInS_2$ reflects their intrinsic electronic structures and confirms the impact of sulfur doping on tuning light–matter interaction. These differences underline the potential of engineering $CuIn\,(Se_{1-x}S_x)_2$ materials with tailored optical conductivities across the solar spectrum, enabling their optimal use in photonic and photovoltaic devices where spectral selectivity and efficient charge carrier dynamics are essential.

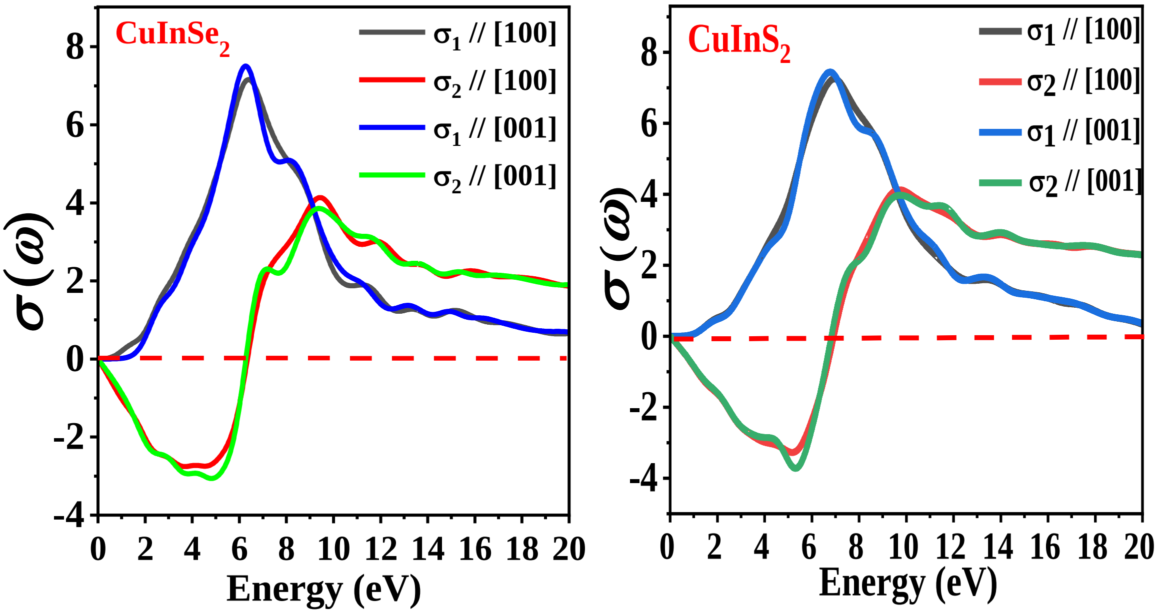

Figure III.11 Energy-Dependent Optical Conductivity Spectra of $CuInSe_2$ and $CuInS_2$ for Various Polarization Orientations

III.6. Conclusion

In conclusion, this study has comprehensively investigated the structural, optical, and electronic properties of the chalcopyrite compound $CuIn(Se_{1-x}S_x)_2$, with sulfur doping ranging from x = 0 ($CuInSe_2$) to x = 1 ($CuInS_2$), using first-principles calculations based on Density

Functional Theory (DFT) within the GGA-PBE approximation. A detailed analysis of the complex dielectric function, refractive index, extinction coefficient, reflectivity, absorption coefficient, optical conductivity, and electronic bandgap has been presented. The obtained energy bandgap values were in good agreement with experimental data and showed significant improvement over previously reported theoretical predictions. Notably, several structural and optical parameters including the bulk modulus (B_0 and B_0') and energy gap variations with sulfur content were theoretically calculated and reported for the first time. The substitution of selenium by sulfur in $CuIn(Se_{1-x}S_x)_2$ significantly affects the optical behaviour of the material. As sulfur content increases, the bandgap widens, the absorption edge shifts towards higher photon energies, and the material becomes more transparent in the visible region while maintaining high absorption in the UV range. This is accompanied by a decrease in the refractive index and extinction coefficient at low energies, resulting in enhanced light transmission and reduced optical losses key advantages for photovoltaic performance. Moreover, the optical conductivity analysis revealed that $CuInSe_2$ exhibits stronger electronic response to low-energy photons, while $CuInS_2$ is more efficient at higher-energy absorption, making their combination ideal for designing tandem or graded-bandgap solar cells. Despite these promising results, practical challenges such as material stability, manufacturing processes, and economic feasibility remain to be addressed. Therefore, future work should focus on experimental validation of these theoretical findings, device-level fabrication, and performance evaluation under real-world conditions. Overall, the $CuIn(Se_{1-x}S_x)_2$ alloy system stands out as a promising and tunable material platform for next-generation thin-film solar cells and optoelectronic applications.

References

[1] W. J. Wang, Y. Jiang, X. Z. Lan, C. Wang, X. M. Liu, B. B. Wang, and X. N. Ding, "Synthesis of CuInSe2 monodisperse nanoparticles and the nanorings shape evolution via a green solution reaction route,» Materials Science in Semiconductor Processing, vol. 15, no.5, pp.467-471, 2012

[2] S. Cui, W. Feng, H. Hu, Z. Feng, and Y. Wang, "Structural and electronic properties of ZnO under high pressure," Journal of Alloys and Compounds, vol. 476, no. 1-2, pp. 306-310, 2009

[3] A. M. Fernandez, and R. N. Bhattacharya, "Electrodeposition of CuIn1− xGaxSe2 precursor films: optimization of film composition and morphology," Thin Solid Films, vol. 474, no. 1-2, pp. 10-13, 2005.

[4] D. A. Tuan, P. Vu, and N. V. Lien, "Design and control of a Three-Phase T-Type Inverter using Reverse-Blocking IGBTs", Eng. Technol. Appl. Sci. Res., vol. 11, no. 1, pp.6614-6619, 2021

[5] A. S. Al-Ezzi, M. N. M. Ansari, N. M. L. Tan, "Flexible and freestanding solar cells based on metal organic chemical vapour deposition-grown graphene", Chemical papers, https://doi.org/10.1007/s11696-025-03910-2, 2025

[6] A. S. Al-Ezzi, M. N. M. Ansari, "Analytical modelling and performance study of single-junction GaAs-based solar cell efficiency", Journal of Korean Physical Society, vol. 86, no. 3, pp.245-262, 2025

[7] A. S. Al-Ezzi, M. N. M. Ansari, "Numerical analysis and performance study of a double-heterojunction GaAs-based solar cell", Journal of Computational Electronics, vol. 23, no. 2, pp.358-368, 2024

[8] J. Xiao, Y. Xie, Y. Xiong, R. Tang, and Y. Qian, "A mild solvothermal route to chalcopyrite quaternary semiconductor CuIn (SexS1− x)$_2$ nanocrystallites," Journal of Materials Chemistry, vol. 11, no. 5, pp. 1417-1420, 2001

[9] S. Bandyopadhyaya, S. Roy, S. Chaudhuri, and A. K. Pal, "CuIn (SxSe1− x) 2 films prepared by graphite box annealing of In/Cu stacked elemental layers," Vacuum, vol. 62, no.1, pp. 61-73., 2001

[10] G. Wang, G. Cheng, B. Hu, X. Wang, S. Wan, S. Wu, and Z. Du, "Preparation of CuIn (SxSe1–x)$_2$ thin films with tunable band gap by controlling sulfurization temperature of CuInSe2," Journal of Materials Research, vol. 25, no. 12, pp. 2426-2429, 2010.

[11] C. Xiang, Z. Yujun, Y. Ruohe, and H. Julong, "Impact of lattice volume on the band gap broadening of isovalent S-doped CuInSe2," Journal of Semiconductors, vol. 29, no. 10, pp. 1883-1888, 2008.

[12] C. J. Sheppard, V. Alberts, and J. R. Botha, "Structural and optical characterization of single phase CuIn (Se, S) 2 thin films deposited using a two step process," .Physica Status Solidi C, vol. 5, no. 2, pp. 641-644, 2008

[13] K. Zeaiter, and C. Llinarès, "Optical properties of the quaternary alloy system Culn (S x Se 1− x)2 investigated by spectroscopic ellipsometry, " Journal of Applied Physics, vol. 86, no. 12,pp. 6822-6825, 1999

[14] M. D. Segall, P. J. Lindan, M. A. Probert, C. J. Pickard, P. J. Hasnip, S. J. Clark, and M. C. Payne, "First-principles simulation: ideas, illustrations and the CASTEP code," Journal of Physics: Condensed Matter, vol. 14, no. 11, p.2717, 2002

[15] S. J. Clark, M. D. Segall, C. J. Pickard,P. J. Hasnip, M. I. Probert, K. Refson, and M. C. Payne, "First principles methods using CASTEP. Zeitschrift für Kristallographie-Crystalline Materials," vol. 220, no. 5-6, pp. 567-570, 2005

[16] J. P. Perdew, K. Burke,and M. Ernzerhof, "Generalized gradient approximation made simple," Physical Review Letters, vol. 77, no. 18, p. 3865, 1996

[17]E. Kask, et al., "Defect studies in Cu2ZnSnSe4 and Cu2ZnSn (Se0. 75S0. 25) 4 by admittance and photoluminescence spectroscopy," Materials Science in Semiconductor Processing, vol. 16, no. 3, pp. 992-996, 2013

[18] A. Contreras Miguel et al., "Issues on the chalcopyrite/defect-chalcopyrite junction model for high-efficiency Cu(In, Ga) Se2 solar cells, " Solar Energy Materials and Solar Cells, vol. 49, no.1-4, pp. 239-247, 1997

[19] R. Herberholz, et al., "Prospects of wide-gap chalcopyrites for thin film photovoltaic modules," Solar Energy Materials and Solar Cells, vol. 49, no.1-4, pp. 227-237, 1997

[20] J. Pohl, and K. Albe, "Thermodynamics and kinetics of the copper vacancy in CuInSe2, CuGaSe2, CuInS2, and CuGaS2 from screened-exchange hybrid density functional theory," Journal of Applied Physics, vol. 108, no. 2, p. 023509, 2010

[21] D. Vanderbilt, "Soft self-consistent pseudopotentials in a generalized eigenvalue formalism," Physical Review B, vol. 41, no.11, p. 7892, 1990

[22] H. J. Monkhorst, and J. D. Pack,. "Special points for Brillouin-zone integrations," Physical Review B, vol. 13, no. 12, p.5188, 1976

[23] F. D. Murnaghan, "The compressibility of media under extreme pressures," Proceedings of the National Academy of Sciences, vol. 30, no. 9, pp. 244-247, 1944

[24] F. C. Wan, F. L. Tang, Z. X. Zhu, H. T. Xue, W. J. Lu, Y. D. Feng, and Z. Y. Rui, "First-principles investigation of the optical properties of CuIn (SxSe1–x) 2, " Materials Science in Semiconductor Processing, vol. 16, no. 6, pp. 1422-1427, 2013.

[25] V. L. Shaposhnikov, A.V. Krivosheeva, V. E. Borisenko, J. L. Lazzari,and F. A. d'Avitaya,, " Ab initio modeling of the structural, electronic, and optical properties of A II B IV C 2 V semiconductors, " Physical Review B - Condensed Matter and Materials Physics, vol. 85, no. 20, p. 205201, 2012

[26] P. Nayebi, K. Mirabbaszadeh, and M. Shamshirsaz, " Density functional theory of structural, electronic and optical properties of CuXY2 (X= In, Ga and Y= S, Se) chalcopyrite semiconductors," Physica B: Condensed Matter, vol. 416, pp. 55-63, 2013

[27] B. I. Adetunji, "Pressure effect on the structural and electronic properties of CuInS2," Solid State Sciences, vol. 55, pp. 42-47, 2016

[28] E. Mazalan, M. S. A. Aziz, N. A. S. Amin, F. D. Ismail, M. S. Roslan, and K. Chaudhary, " First principles study on crystal structures and bulk modulus of CuInX2 (X= S, Se, S-Se) solar cell absorber," Journal of Physics: Conference Series (vol. 2432, no. 1, p. 012009). IOP Publishing, 2023

[29] J. W. Yang and L. An, " First-principles determination of pressure-induced structure, anisotropic elasticity and ideal strengths of CuInS2 and CuInSe2, " Solid State Communications, vol. 316, p.113952, 2020

[30] H. L. Hwang, C. Y. Sun, C. Y. Leu, C. L, Cheng, and C. C. Tu,." Growth of CuInS2 and its characterization," Revue de Physique Appliquée, vol. 13, no. 12, pp. 745-751, 1978

[31] M. L. Fearheiley, K. J. Bachmann, Y. H. Shing, S. A. Vasquez, and C. R. Herrington, "The lattice constants of CuInSe 2. Journal of electronic materials," vol. 14, pp. 677-683, 1985

[32] T. Tinoco, A. Polian, D. Gomez, and J. P. Itie, " Structural studies of CuInS2 and CuInSe2 under high pressure, " Physica Status Solidi (b), vol. 198, no 1, pp. 433-438, 1996

[33] M. Belhadj, A. Tadjer, B. Abbar, Z. Bousahla, B. Bouhafs, and H. Aourag, "Structural, electronic and optical calculations of Cu (In, Ga) Se2 ternary chalcopyrites," Physica Status Solidi (b), vol. 241, no. 11, pp. 2516-2528, 2004.

[34] A. Sajid, S. Ullah, G. Murtaza, R. Khenata, A. Manzar, and S. B. Omran, " Electronic structure and optical properties of chalcopyrite CuYZ2 (Y= Al, Ga, In; Z= S, Se): an ab initio study," J. Optoelectronics and Advanced Materials, vol. 16, p.76, 2014

[35] **M.** Hadjab, M. Ibrir, S. Berrah, H. Abid, and M. A. Saeed, "Structural, electronic and optical properties for chalcopyrite semiconducting materials: ab-initio computational study," Optik, vol. 169, pp. 69-76., 2018

[36] M. I. Alonso, K. Wakita, J. Pascual, M. Garriga, and N. Yamamoto, "Optical functions and electronic structure of CuInSe 2, CuGaSe 2, CuInS 2, and $CuGaS_2$,".Physical Review B, vol. 63, no. 7, p. 075203, 2001

[37] S. Adachi, "Properties of semiconductor alloys: group-IV, III-V and II-VI semiconductors," John Wiley & Sons, 2009.

[38] C. F. Klingshirn, Semiconductor Optics. Springer Science & Business Media, 2012.

[39] M. Gajdošet al. "Linear optical properties in the projector-augmented wave methodology," Physical Review B-Condensed Matter and Materials Physics, vol.73, no..4, 045112 , 2006

[40] A. Soni et al. "Electronic and optical modeling of solar cell compounds CuGaSe2 and CuInSe2," Journal of Electronic Materials, vol. 40, no.11, pp. 2197-2208, 2011

[41] S. Levcenkoet al. "Optical spectra and energy band structure of single crystalline CuGaS2 and CuInS2," Journal of Physics: Condensed Matter, vol. 19, no. 45, p. 456222, 2007

[42] J. C. Rifeet al. "Optical properties of the chalcopyrite semiconductors ZnGe P 2, ZnGe As 2, CuGa S 2, CuAlS2, CuInSe2, and AgIn Se 2," Physical Review B, vol. 16, no.10, p. 4491, 1977

[43]M. Othman, E. R. G. U. N. Kasap, and N. Korozlu, "The structural, electronic and optical properties of InxGa1− xP alloys," Physica B: Condensed Matter, vol. 405, no. 10, pp. 2357-2361, 2010

[44] A. Mouhoub, F. Khaled, and A. Bouloufa," Performance Analysis of Ultrathin Cu (In, Ga) Se2 Solar Cells with Backwall Superstrate Configuration Using AMPS-1D," Engineering, Technology & Applied Science Research, vol. 12, no.6, pp. 9687-9691, 2022

[45] N. Bouarissa, H. Aourag, "Effective masses of electrons and heavy holes in InAs, InSb, GaSb, GaAs and some of their ternary compounds," Infrared Physics and Technology, vol. 40, no. 4, pp.343-349, 1999

[46] M. Merabet, I. Bouchama, T. Chihi, L. Foudia, F. Saidi, and N. Bouarissa, ‘Ab initio study of the effect of sulphur concentration on the structural, electronic and optical properties of $CuIn(Se_{1-x}S_x)_2$ compound using generalized gradient approximation’, Eng. Technol. Appl. Sci. Res., vol. 15, no. 3, pp. 24026–24034, June 2025.

Chapter IV

Photovoltaic Application of CuIn$(Se_{1-x}S_x)_2$ materials

IV.1 Introduction

Chalcopyrite semiconductors, such as $CuInSe_2$ and $CuInS_2$, have attracted significant research attention due to their remarkable optoelectronic properties [1], direct bandgaps, and high absorption coefficients, making them excellent candidates for solar cell applications. The chalcopyrite crystal structure of these I–III–VI_2 compounds comprising two face-centered cubic sublattices—facilitates efficient charge transport and allows for tunable energy gaps. Devices based on $CuInSe_2$ exhibit a direct bandgap close to 1.0 eV [2] and a high absorption coefficient exceeding 10^4 cm^{-1}, making them highly effective as absorber layers in thin-film photovoltaics. Recent studies have reported power conversion efficiencies (PCE) surpassing 18% for $CuInSe_2$ based devices, alongside excellent long-term stability and superior crystal quality [3,4].

On the other hand, $CuInS_2$, another chalcopyrite compound, offers a wider bandgap (~1.5–1.6 eV) [5], which makes it particularly attractive for tandem solar cells and quantum dot photovoltaic designs. Despite its promising theoretical potential, the practical efficiency of $CuInS_2$ devices is often constrained by interface recombination phenomena, a common challenge in chalcopyrite-based absorbers [6].

Numerical simulation tools particularly SCAPS-1D play a pivotal role in optimizing absorber layer thickness, doping concentration, and defect density in chalcopyrite solar cells, thereby enabling higher open-circuit voltages, short-circuit currents, and fill factors under standard AM1.5G illumination [7].

In recent years, hybrid approaches involving integration or compositional grading between $CuInS_2$ and CIGS ($Cu(In,Ga)(S,Se)_2$) have emerged at the forefront of research. Such strategies aim to combine the unique advantages of each chalcopyrite absorber, extending the performance boundaries of next-generation thin-film photovoltaics [7].

In this work, we employ a hybrid $CuInS_2$/CIGS architecture to enhance light absorption, improve charge separation, and ultimately boost the efficiency of chalcopyrite thin-film solar cells. Through a systematic simulation study using SCAPS-1D, we investigate the effects of absorber layer properties, compositional grading, and defect control, demonstrating the potential of the hybrid design for advancing high-performance photovoltaic technologies.

IV.2. Modeling of substrate CuInSe$_2$ and CuInS$_2$ solar cells

The conventional structure of CuInSe$_2$ and CuInS$_2$ solar cells typically comprises a glass substrate, a molybdenum (Mo) back contact, the p-type CuInSe$_2$ or CuInS$_2$ absorber layer, an n-type CdS buffer layer, and a transparent conducting oxide (TCO) front contact layer, generally made of ZnO. This layered configuration is meticulously designed to maximize light absorption, enhance charge carrier transport, and optimize charge collection within the absorber layers.

In this structure, the CdS buffer layer is positioned between the ZnO window layer and the p-type absorber to form a high-quality p–n heterojunction critical for efficient photovoltaic operation. The buffer layer thickness is generally around 0.1 μm, with donor doping concentrations typically near 1×10^{17} cm^{-3} and a relatively wide band gap of approximately 2.4 eV [8], which helps reduce absorption losses while facilitating good junction properties. The CuInSe$_2$ and CuInS$_2$ absorber layers are p-type semiconductors with thicknesses commonly near 3 μm, doped at acceptor densities around 1×10^{16} cm^{-3}, with band gap energies of about 1.04 eV [2] for CuInSe$_2$ and roughly 1.53 eV [5] for CuInS$_2$, enabling effective solar spectrum absorption. The ZnO (n^+) window layer used as the front contact is a wide bandgap TCO with a thickness of about 0.1 μm, a band gap near 3.3 eV [9], and donor concentrations around 1×10^{18} cm^{-3}, ensuring transparency and efficient charge extraction. Figure IV.1 in the related literature illustrates the schematic of this conventional solar cell configuration.

In the initial phase of this study, we focus on investigating how the thickness and doping concentration of the CuInSe$_2$ and CuInS$_2$ absorber layers influence the current density–voltage (J–V) characteristics and the quantum efficiency (QE) of the standard ZnO/CdS/CuInSe$_2$ and ZnO/CdS/CuInS$_2$ solar cells. Such investigations are essential for optimizing device performance and are informed by both experimental and numerical simulation studies.

IV.3. Physical model and simulation parameters

SCAPS-1D software (version 3.3.07) was employed to simulate the performance of CuInSe$_2$ and CuInS$_2$ solar cells, providing a rigorous numerical framework for solving the Poisson and continuity equations for electrons and holes. This approach enables the accurate determination of current–voltage (J–V) characteristics and quantum efficiency (QE) under standardized AM1.5G illumination conditions (100mW cm^{-2}) at 300K, ensuring that the simulation environment closely mirrors typical operating scenarios.

The modeling in SCAPS-1D uses the Newton method by default to solve these coupled semiconductor equations, allowing for precise analysis of charge carrier dynamics [10], recombination mechanisms, and transport behavior within multilayer device structures. Input simulation parameters including layer thickness, energy bandgap, electron affinity, relative permittivity, carrier densities, mobilities, densities of states for conduction and valence bands, thermal velocities, and electron/hole capture cross-sections are detailed in **Table IV.1**, as established from verified literature sources and previous experimental or theoretical work. For material-specific properties, values such as the bandgap (Eg) for $CuInSe_2$ and $CuInS_2$ alloys are drawn directly from references and tabulated data, providing critical input for the simulation and ensuring reliable modeling of optical absorption and carrier generation.

By integrating this modeling strategy, SCAPS-1D facilitates a precise assessment of photovoltaic performance and supports device optimization through careful control of layer physical properties, doping concentrations, and defect densities.

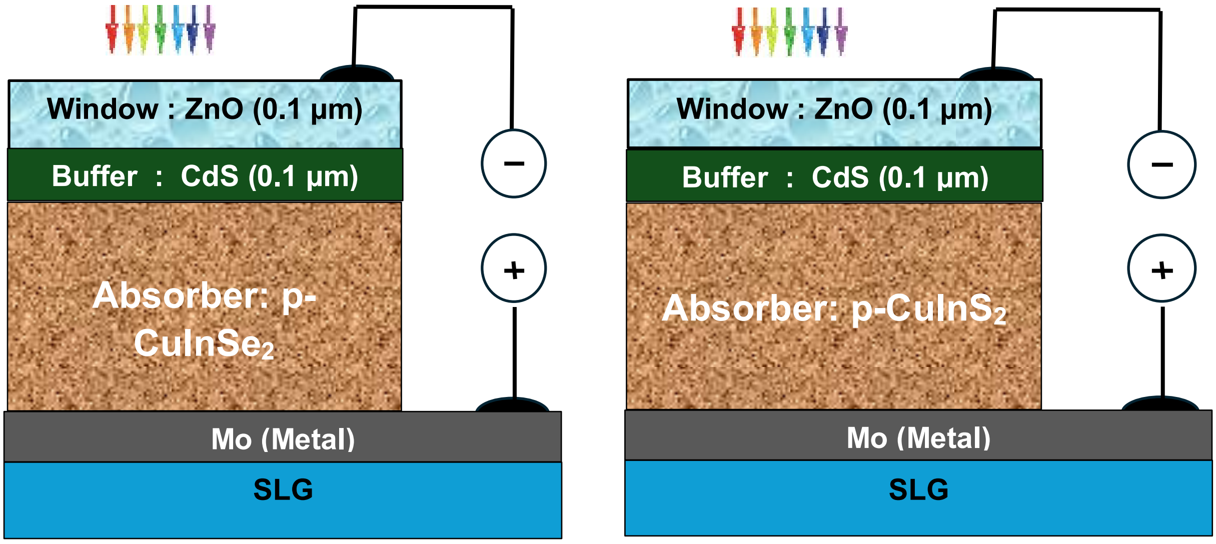

Figure IV.1: $CuInSe_2$ and $CuInS_2$ solar cell structures.

The input parameters for each layer in the proposed structure are listed in Table IV.1. These include the layer thickness, relative permittivity ε_r , band gap Eg, electron affinity χe, electron and hole mobilities μ_n/μ_p , effective density of states in the conduction and valence bands N_C/N_V , and donor/acceptor concentrations N_D/N_A . Reflection at the front contact was disregarded. The surface recombination velocities for holes and electrons S_n/S_p at both the front and back contacts were set to 1 × 10^7 cm/s.

Since all the layers are polycrystalline, they inherently contain a wide range of defects [11]. Therefore, for the $CuInSe_2$ and $CuInS_2$ materials, we used two neutral defect distributions, while for the ZnO and CdS layers, we also implemented two neutral defect distributions. The parameters of these neutral defect distributions are provided by SCAPS-1D.

$CuInSe_2$ and $CuInS_2$ possess distinct physical characteristics, including differences in color, crystal structure, and electrical properties [12] Both compounds adopt the chalcopyrite crystal structure (space group I$\bar{4}$2d, tetragonal) and show good structural stability under ambient conditions. Experimentally, both $CuInSe_2$ and $CuInS_2$ are natural p-type semiconductors having dominant hole conduction, as determined by Hall measurements and conductivity studies [13-14]

The material properties employed in the simulations are documented in the literature, and the parameters for $CuInSe_2$, $CuInS_2$, and CdS used in our simulations are provided in Table IV.1

Table IV.1: Parameters values of $CuInSe_2$ and $CuInS_2$ solar cell structures used in SCAPS-1D [7,15-22].

Material properties	**$CuInSe_2$**	**$CuInS_2$**	**CdS**	**ZnO**
Thickness	Varied	Varied	0.1	0.1
Band gap [eV]	1.04	1.53	2.4	3.3
Electron affinity [eV]	4.7	4.5	4.2	4.6
Dielectric permittivity (relative)	10	10	10	9
CB (conduction band) effective density of states [cm^{-3}]	2 × 10^{18}	2 × 10^{18}	2 × 10^{18}	2.2 × 10^{18}
VB (valence band) effective density of states [1/cm^3]	2 × 10^{18}	2 × 10^{18}	1.5 × 10^{19}	1.8 × 10^{19}
Electron mobility μn[cm^2 /Vs]	50	50	100	100
Hole mobility μp [cm^2 /Vs]	20	20	25	25
Shallow uniform donor density N_D [1/cm^3]	0	0	1 × 10^{17}	1 × 10^{18}
Shallow uniform acceptor density N_A [1/cm^3]	1 × 10^{17}	1 × 10^{17}	0	0

IV.4. Band diagram

The band gap and optical properties of CuInSe2 and CuInS2 have been extensively studied through both theoretical calculations and experimental investigations. Experimentally, it is well established that CuInSe2 exhibits a direct forbidden band gap of 1.04 eV [23] while CuInS2 possesses a direct forbidden band gap of approximately 1.5 eV [24]. These values indicate that both compounds are direct band gap semiconductors, making them attractive for photovoltaic applications [25].

Figure IV.2 represents the energy band diagrams of the solar cell structures based on $CuInSe_2$ and $CuInS_2$, as obtained through simulation. These diagrams were constructed using the optical absorption data reported in experimental studies, specifically those presented by Möller [26] and by Chopra [27]. Such data were employed as the basis for analyzing the optical and electronic properties of both compounds.

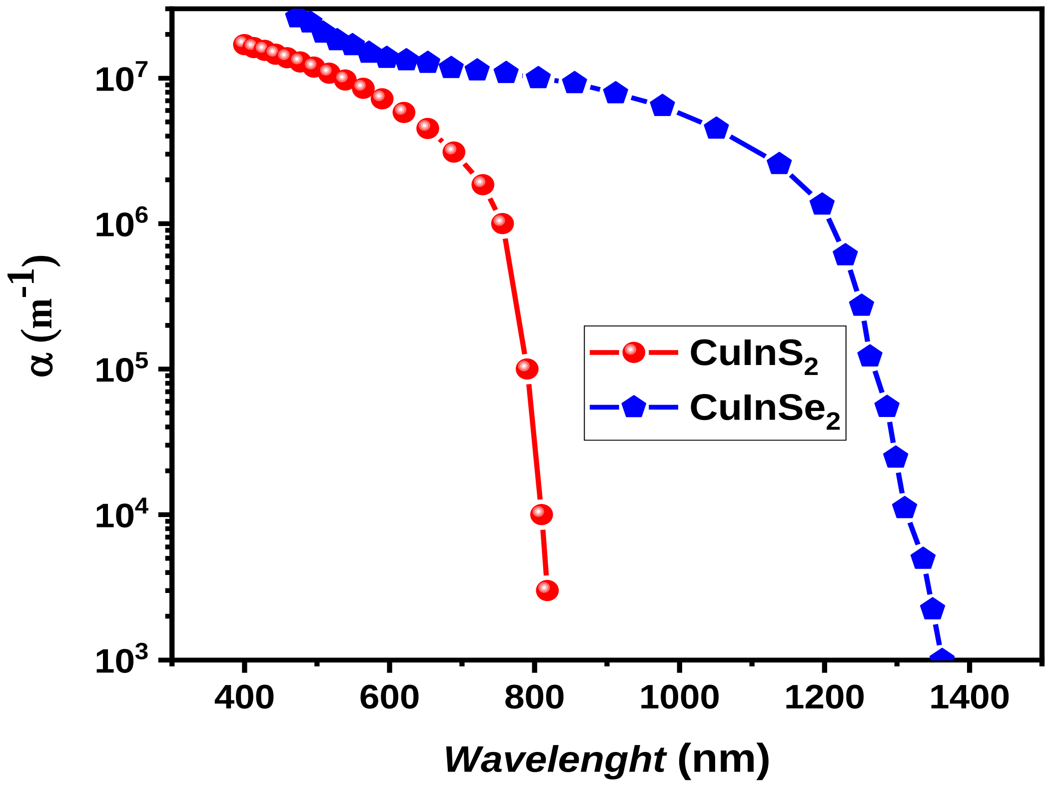

Figure IV.2: Absorption coefficient α for both $CuInSe_2$ and $CuInS_2$ absorber films used in the simulation.

The figure illustrates the optical absorption coefficient (α) as a function of wavelength for thin films of $CuInS_2$ and $CuInSe_2$. Both materials exhibit very high absorption coefficients on the order of 10^7 m^{-1} at shorter wavelengths (400–600 nm), indicating their strong capability to absorb visible light efficiently. For $CuInS_2$, the absorption coefficient remains high until about 800 nm, after which it sharply decreases, reflecting its higher band gap around 1.5 eV. In contrast, $CuInSe_2$

maintains a high absorption coefficient over a broader wavelength range, extending up to approximately 1200 nm before a significant drop, consistent with its narrower band gap of about 1.04 eV. The sharp decline in absorption coefficient at specific wavelengths corresponds to the fundamental absorption edges related to their band gaps. This spectral behavior means that $CuInSe_2$ can absorb lower-energy photons with longer wavelengths than $CuInS_2$. Such strong absorption properties across different parts of the solar spectrum make both materials especially suitable for use as absorber layers in thin-film solar cells, where efficient light harvesting is critical for high photovoltaic performance.

Figures IV.3 (a) and (b) present the simulated band diagrams for solar cell structures based on $CuInSe_2$ and $CuInS_2$, respectively. Each diagram illustrates the variation of conduction band edge (Ec, black curve) and valence band edge (Ev, red curve) across the device layers: the p-type absorber ($CuInSe_2$ or $CuInS_2$), n-type CdS buffer, and n-type ZnO window.

(a)

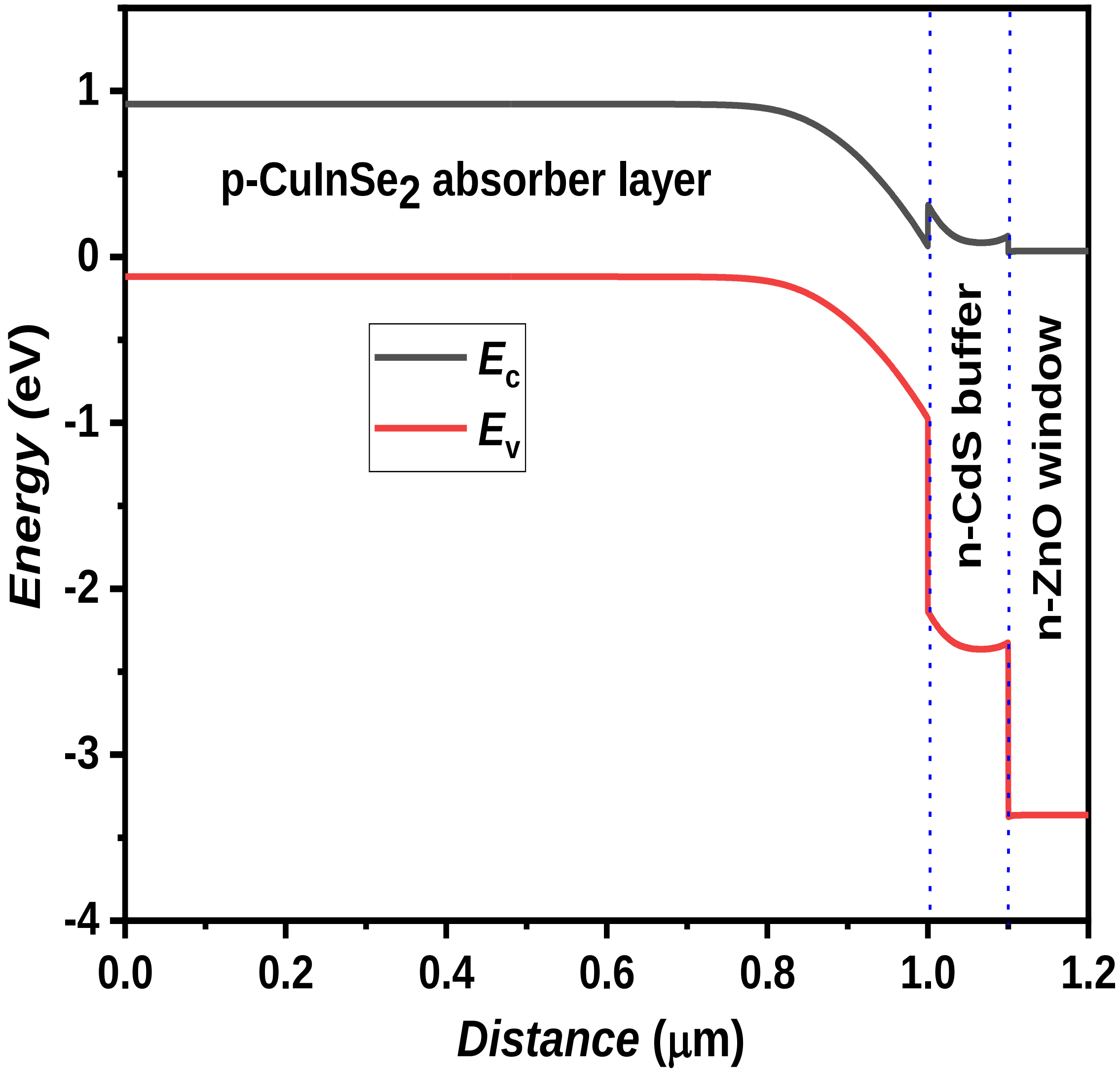

(b)

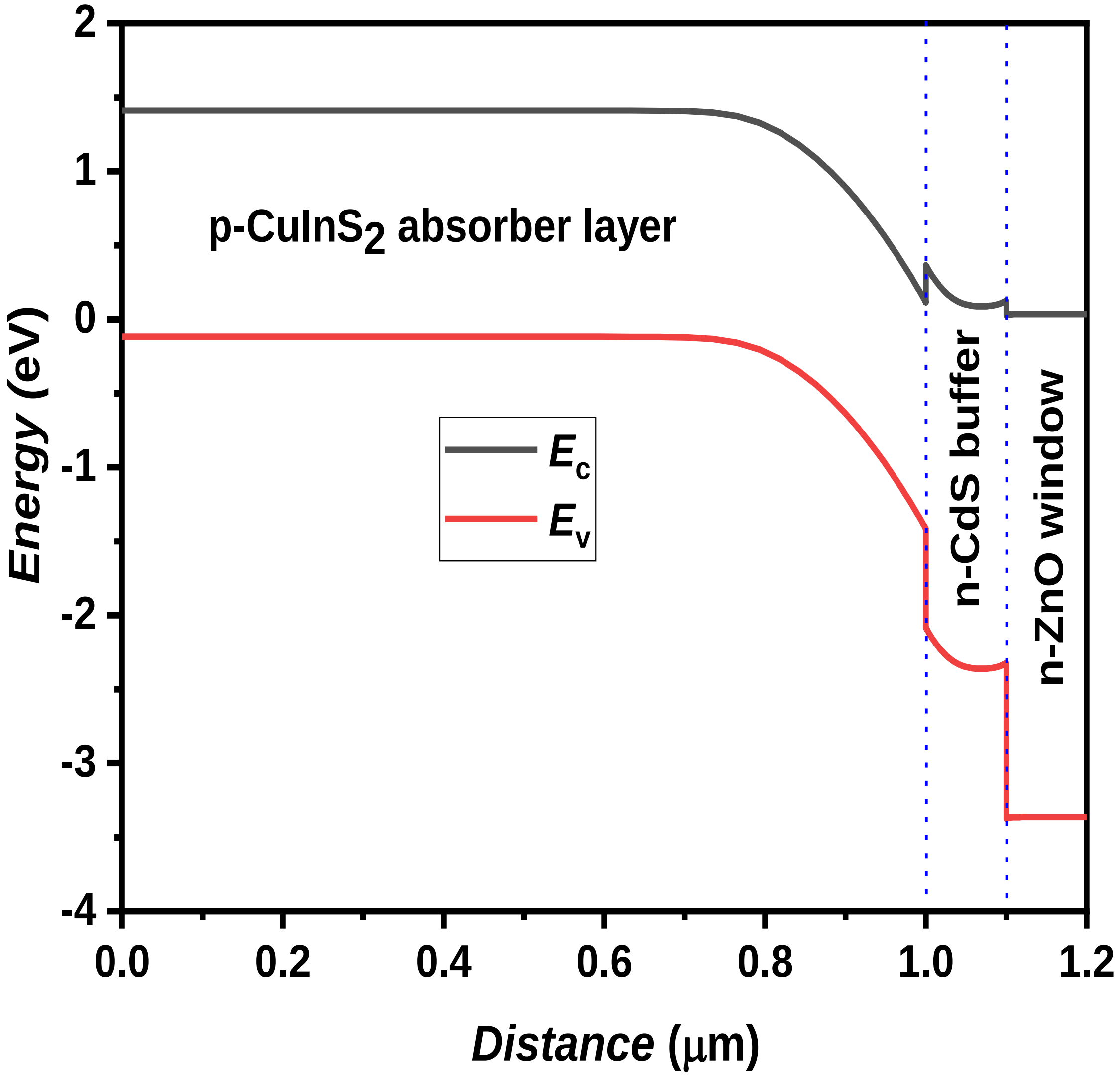

Figure IV.3: Band diagram for (a) CuInSe$_2$ and (b) CuInS$_2$ solar cells structures used in the simulation.

The band diagrams illustrate the variation of energy levels across the layers of the solar cells based on CuInSe$_2$ and CuInS$_2$. The p-type absorber layer shows a clear energy gap between the conduction band edge and the valence band edge, which is essential for absorbing light and generating electron-hole pairs. At the interfaces between the absorber, the n-type CdS buffer layer, and the n-type ZnO window, there are noticeable discontinuities in the band edges due to differences in the electronic properties of the materials. These discontinuities create built-in electric fields that facilitate the efficient separation and transport of photogenerated charge carriers-electrons are driven toward the ZnO layer, while holes move toward the absorber layer.

The band gap in $CuInS_2$ is wider than in $CuInSe_2$, which affects the spectral response and the open-circuit voltage of the solar cells. Overall, these band diagrams provide important insights into the charge dynamics and the photovoltaic efficiency of each solar cell structure.

IV.5. Thickness optimization of $CuInSe_2$ and $CuInS_2$ absorber layer

Thickness plays a crucial role in the design and fabrication of thin-film solar cells, as it is a key factor in balancing optical absorption and carrier transport efficiency. Selecting the optimal absorber layer thickness is not merely an engineering parameter; it is an essential element that directly influences the photovoltaic cell performance. In this context, the performance of solar cells based on CdS/ZnO/$CuInSe_2$ and CdS/ZnO/$CuInS_2$ structures was examined, utilizing the material parameters summarized in Table IV.1. Simulation results, as illustrated in Figure IV.4, show the evolution of the main photovoltaic characteristics—the open-circuit voltage (Voc), short-circuit current density (Jsc), fill factor (FF), and photovoltaic conversion efficiency (η) as functions of the absorber layer thickness for both $CuInSe_2$ and $CuInS_2$.

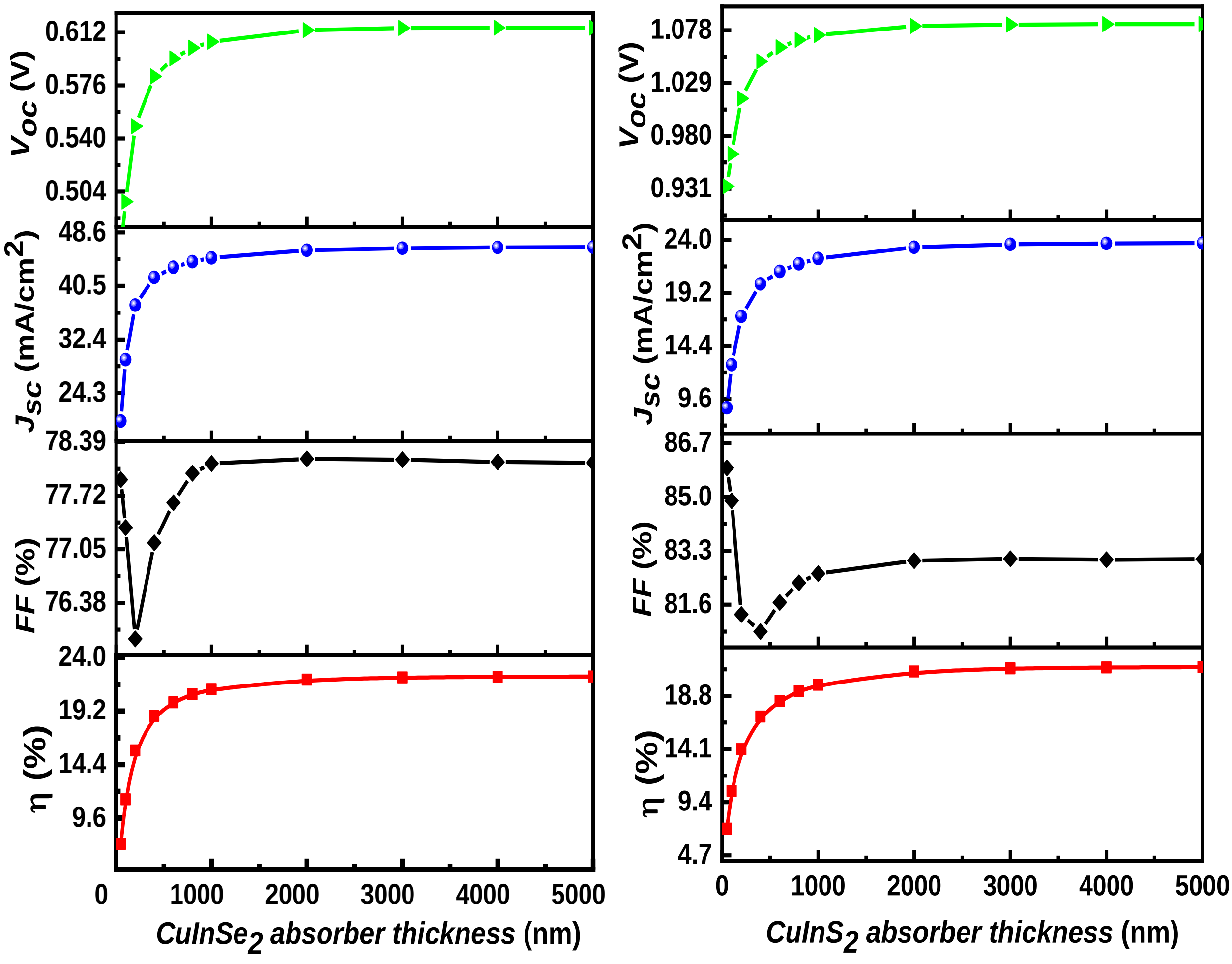

Figure IV.4: Cell performance as a function of $CuInSe_2$ and $CuInS_2$ absorber layer thickness.

As the thickness of the CuInSe$_2$ absorber layer increases, all key photovoltaic parameters open-circuit voltage (*Voc*), short-circuit current density (*Jsc*), fill factor (*FF*), and conversion efficiency (η) improve rapidly at first. This is because a thicker CuInSe$_2$ layer absorbs more light, generating a greater number of electrons–holes pairs for current production. When the thickness reaches around 2000nm (2µm), these metrics approach their maximum values: *Jsc* stabilizes near 46mA/cm², η approaches 22%, *Voc* and *FF* also reach peak performance. Beyond this point, further increases in thickness bring little benefit, as almost all incident photons are already absorbed and other losses, such as recombination, may increase. Thus, the optimal absorber thickness for CuInSe$_2$ is about 2µm, balancing light absorption and electronic transport for maximum solar cell efficiency.

For the CuInS$_2$ solar cell, a similar trend is observed. As the absorber thickness increases, *Voc*, *Jsc*, *FF*, and efficiency η all show marked improvement early on, primarily due to enhanced photon absorption and increased carrier generation. However, once the CuInS$_2$ layer reaches approximately 2000nm (2µm) in thickness, the rise in performance parameters flattens out. The short-circuit current density (*Jsc*) stabilizes around 23 mA/cm² and the conversion efficiency (η) peaks close to 21%. Beyond this optimal thickness, additional increases have minimal effect on cell performance. Therefore, the optimal absorber thickness for CuInS$_2$ is also 2µm, which ensures that nearly all useful light is absorbed without incurring extra losses.

For a deeper evaluation of how absorber thickness impacts current generation in solar cells, the quantum efficiency (QE) as a function of wavelength has been calculated for varying thicknesses of the absorber layer in both CuInSe$_2$ and CuInS$_2$ solar cell structures. The results are presented in Figure IV.5 for absorber thicknesses ranging from 0.1 to 5 µm.

For the CuInSe$_2$ solar cell, the quantum efficiency (QE) improves significantly with increasing absorber layer thickness. As the thickness grows, the cell becomes more effective at absorbing photons, especially in the longer wavelength region. This effect is observed by the curve extending closer to 1,200nm as the layer becomes thicker. With a sufficiently thick absorber (~3µm), QE approaches nearly 100% in the intermediate wavelength range (400–1100nm), indicating almost all incident photons are successfully converted into charge carriers up to the absorption edge. In thinner layers, current losses are more apparent since lower-energy photons are not absorbed efficiently, resulting in reduced QE in the infrared region.

(a)

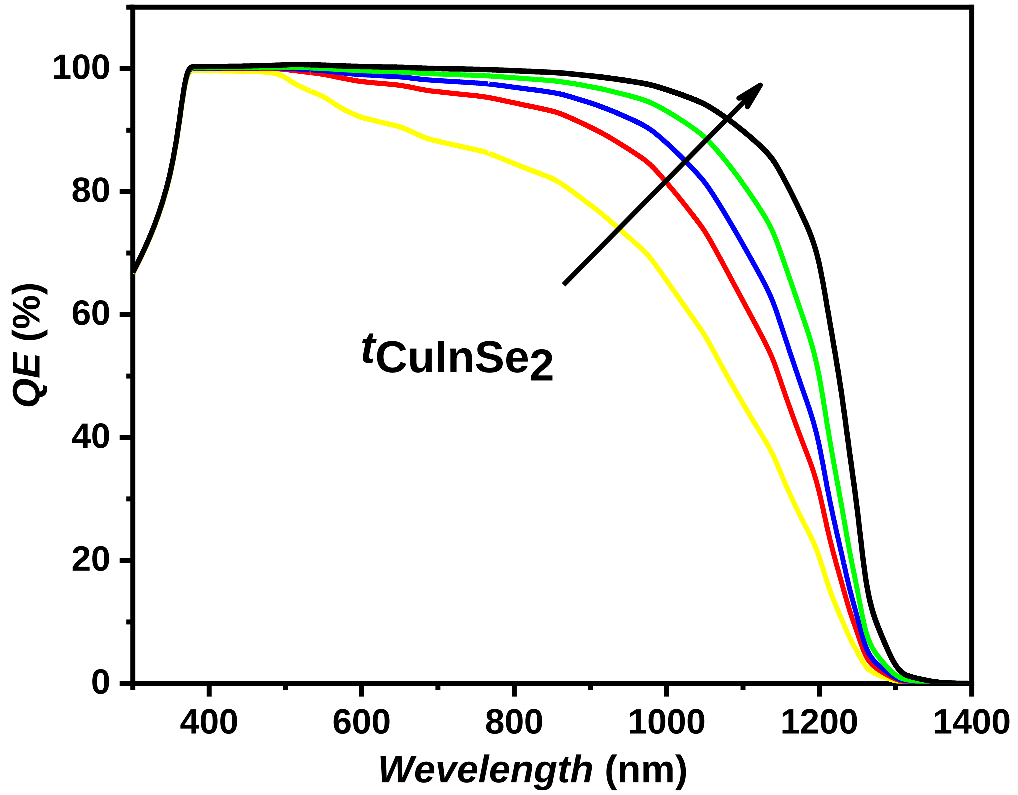

(b)

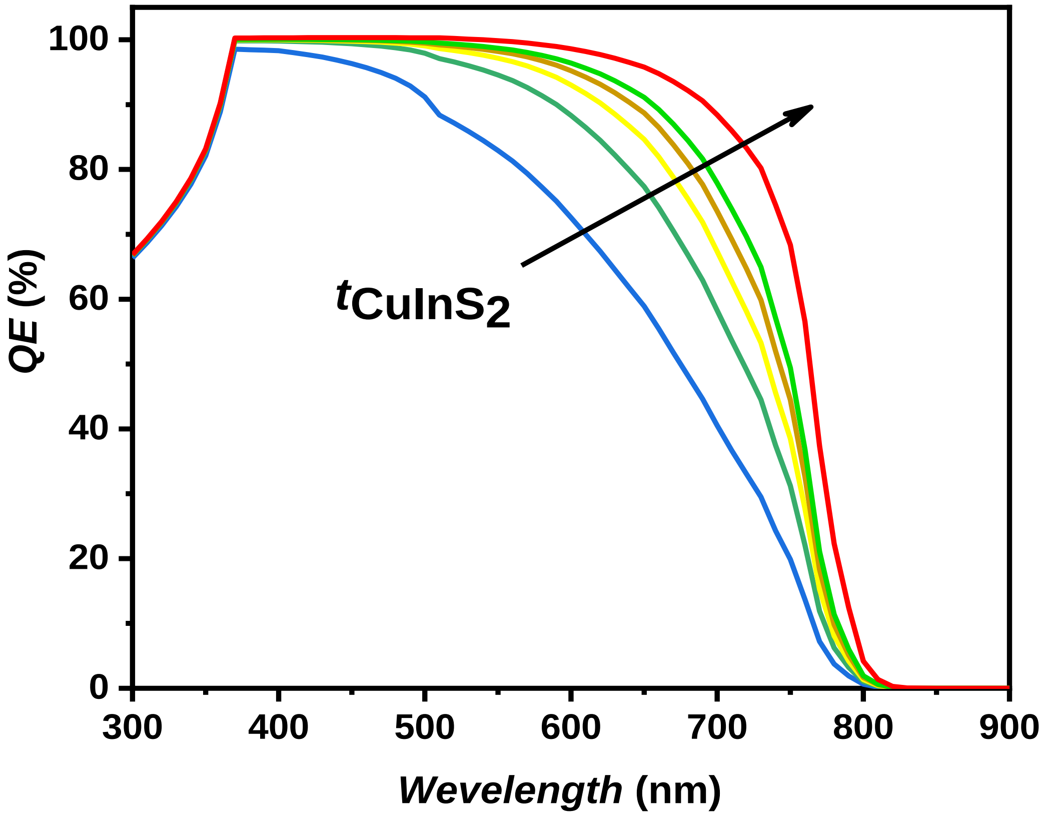

Figure IV.5. Quantum efficiency versus wavelength of (a) $CuInSe_2$ and (b) $CuInS_2$ solar cell structures.

Similarly, for the $CuInS_2$ solar cell, increasing absorber thickness enhances QE, though the optimal range is dictated by the material's larger band gap. As thickness increases, QE remains high across the visible spectrum (300–800nm) and then drops sharply near the absorption edge around 800nm. Maximum quantum efficiency is achieved for the thickest absorber, reflecting highly efficient conversion of incident photons in the usable spectral range. If the absorber is too thin, a considerable fraction of incident light (particularly longer wavelengths) is not absorbed, causing current losses and limiting device performance.

In summary, both $CuInSe_2$ and $CuInS_2$ solar cells benefit from increased absorber thickness, which ensures strong photon absorption and maximized quantum efficiency throughout the relevant spectral range of each material. However, the range of effective absorption is set by the intrinsic band gap: $CuInSe_2$ captures a broader spectrum reaching the infrared, while $CuInS_2$ is limited to shorter wavelengths due to its wider band gap. Thus, choosing the appropriate absorber thickness is essential for maximizing cell performance in either case.

IV.6. Optimization of acceptor density $N_A(CuInSe_2)$ and $N_A(CuInS_2)$

The acceptor concentration (N_A) in the absorber layer is a critical parameter for optimizing the performance of $CuInSe_2$ and $CuInS_2$ based thin-film solar cells. By systematically adjusting the acceptor density from very low 10^{11} cm^{-3} to very high values 10^{19} cm^{-3}, one can observe substantial changes in the main photovoltaic parameters: open-circuit voltage (*Voc*), short-circuit current density (*Jsc*), fill factor (*FF*), and conversion efficiency (η). Figure IV.6 presents the simulated photovoltaic behavior as a function of N_A for both $CuInSe_2$ and $CuInS_2$ absorber layers, allowing identification of the optimal doping for maximum solar cell performance.

As *NA* in the $CuInSe_2$ absorber increases, the open-circuit voltage (*Voc*) rises steadily, reaching its peak at the highest concentrations shown. The short-circuit current density (*Jsc*) remains nearly constant for N_A up to roughly 10^{16} cm^{-3}, then drops sharply as N_A exceeds 10^{17} cm^{-3}. This drop is attributed to increased free carrier recombination in the heavily doped material, which limits effective carrier collection. The fill factor (*FF*) and conversion efficiency (η) improve with increasing N_A up to around 10^{16}–10^{17} cm^{-3}, peaking at $\eta \approx 23.3$ %. However, for concentrations above this optimal range, both *FF* and efficiency decline sharply, again due to recombination losses. Therefore, the optimal acceptor concentration for $CuInSe_2$ is between 10^{16} cm^{-3} and 10^{17}cm^{-3}, providing high voltage, stable current, and maximal cell efficiency.

For $CuInS_2$, increasing N_A leads to a continuous rise in *Voc* and a moderate increase in *FF* up to about 10^{16}–10^{17} cm^{-3}, where the maximum conversion efficiency (η) of approximately 21.2 %

is achieved. The short-circuit current density (*Jsc*) remains nearly constant up to this optimum, then decreases drastically at higher doping levels because of intensified carrier recombination. Beyond the optimal concentration, both voltage and efficiency drop off, making overly high acceptor densities detrimental to performance. The best results for $CuInS_2$ solar cells are also obtained for N_A in the range of 10^{16} cm^{-3} to 10^{17} cm^{-3}, balancing high voltage and minimal recombination losses to maximize efficiency.

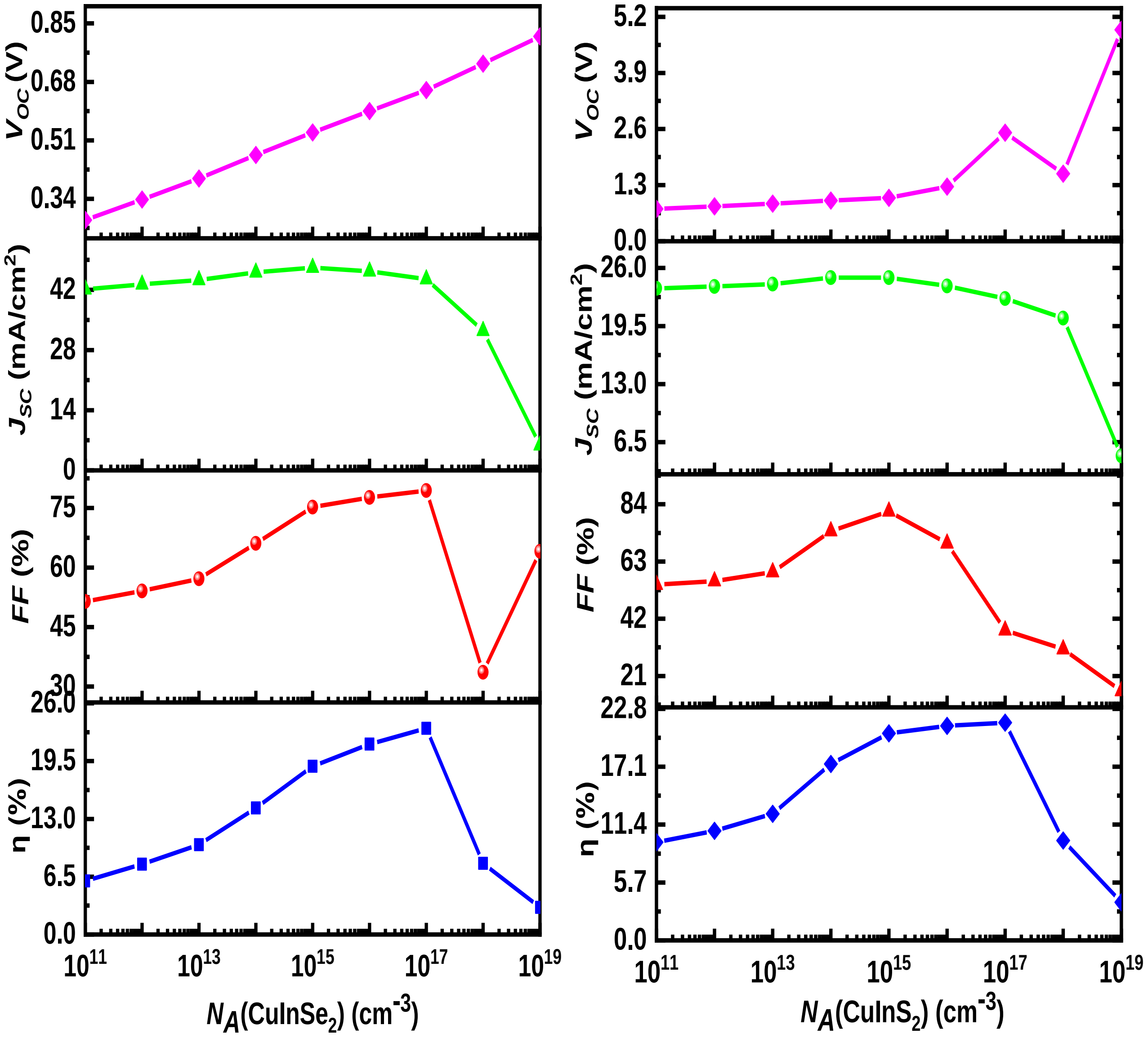

Figure IV.6: Effect of acceptor concentration of absorber layer $N_A(CuInSe_2)$ and $N_A(CuInS_2)$ on cell performances.

The quantum efficiency (QE) of $CuInSe_2$ and $CuInS_2$ solar cells is highly sensitive to the acceptor concentration (NA) within the absorber layers. Variations in doping levels directly impact the efficiency of converting incident photons into electrical current across the solar spectrum. As illustrated in Figure IV.7, this behavior highlights the crucial role of acceptor concentration in optimizing solar cell performance.

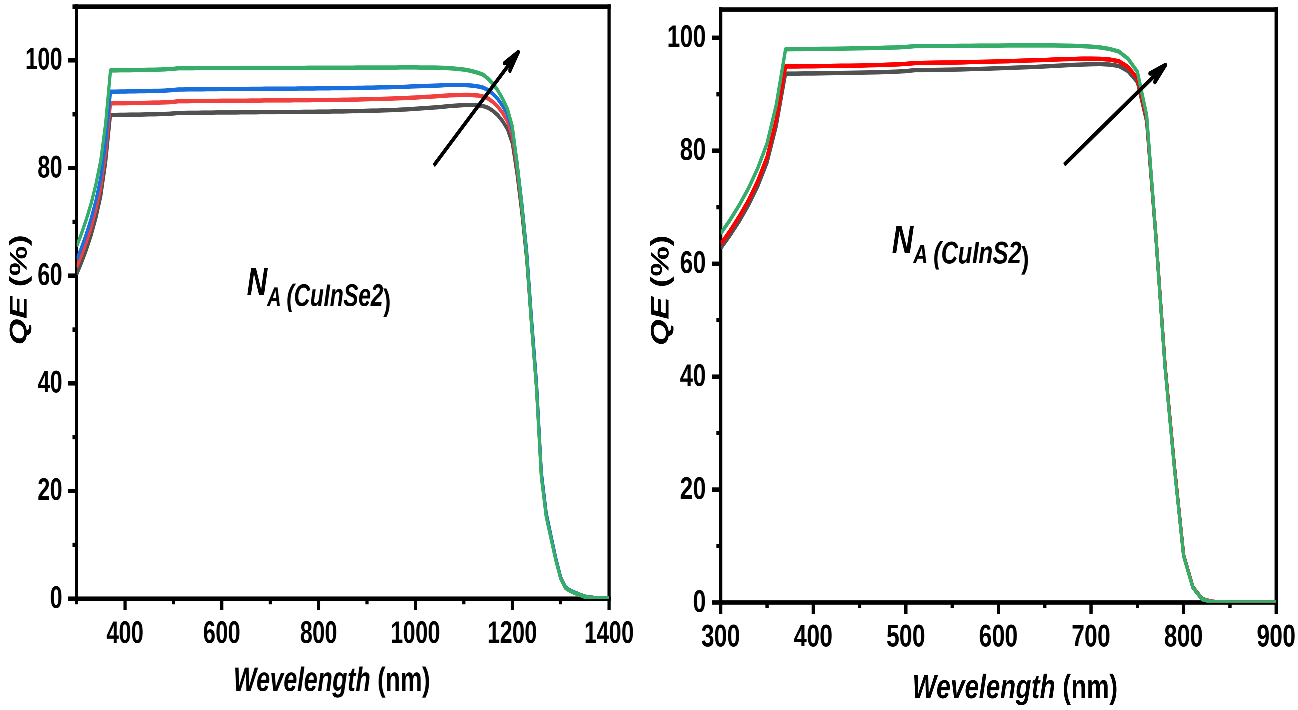

Figure IV.7: Quantum efficiency (QE) of $CuInSe_2$ and $CuInS_2$ solar cells at various acceptor concentrations NA($CuInSe_2$) and NA($CuInS_2$).

In the QE versus wavelength plot for $CuInSe_2$ solar cells, we observe that increasing the acceptor concentration (N_A) in the absorber layer enhances quantum efficiency across a broad spectral range. Higher N_A improves carrier collection by reducing recombination losses, so that most photogenerated carriers are efficiently collected and contribute to the current. This effect is especially noticeable near the long-wavelength edge (1,000–1,200nm), where the quantum efficiency is maximized and the response extends further due to improved absorption and transport properties. Across all curves, nearly ideal QE values (~98–100%) are reached in the visible and near-infrared regions, reflecting superior photon-to-current conversion when the cell is properly doped.

For $CuInS_2$, the quantum efficiency also increases with higher acceptor concentration, but its enhancement is limited by the material's larger band gap. As N_A rises, carrier collection and separation efficiency improve, leading to higher QE in the range from 400nm up to the absorption edge near 800nm. The curves show very high QE (close to 100%) in the visible region, peaking just before the band edge. This trend demonstrates that optimal doping boosts conversion efficiency by minimizing carrier recombination and maximizing the collection of photogenerated electrons and holes, even though the effective spectral window is narrower than $CuInSe_2$ due to the wider band gap.

IV.7. Influence of defect state density of $CuInSe_2$ and $CuInS_2$ absorber layers

Defect state density (NT) in the absorber layers is a critical parameter affecting the performance of $CuInSe_2$ and $CuInS_2$ solar cells. These bulk defects serve as trap states within the band-gap and strongly influence carrier recombination, thus impacting current generation and overall device efficiency. Figures illustrate how increasing the trap defect density affects the main photovoltaic characteristics, helping clarify the connection between material quality and solar cell output, and these trends are shown in Figure IV.8.

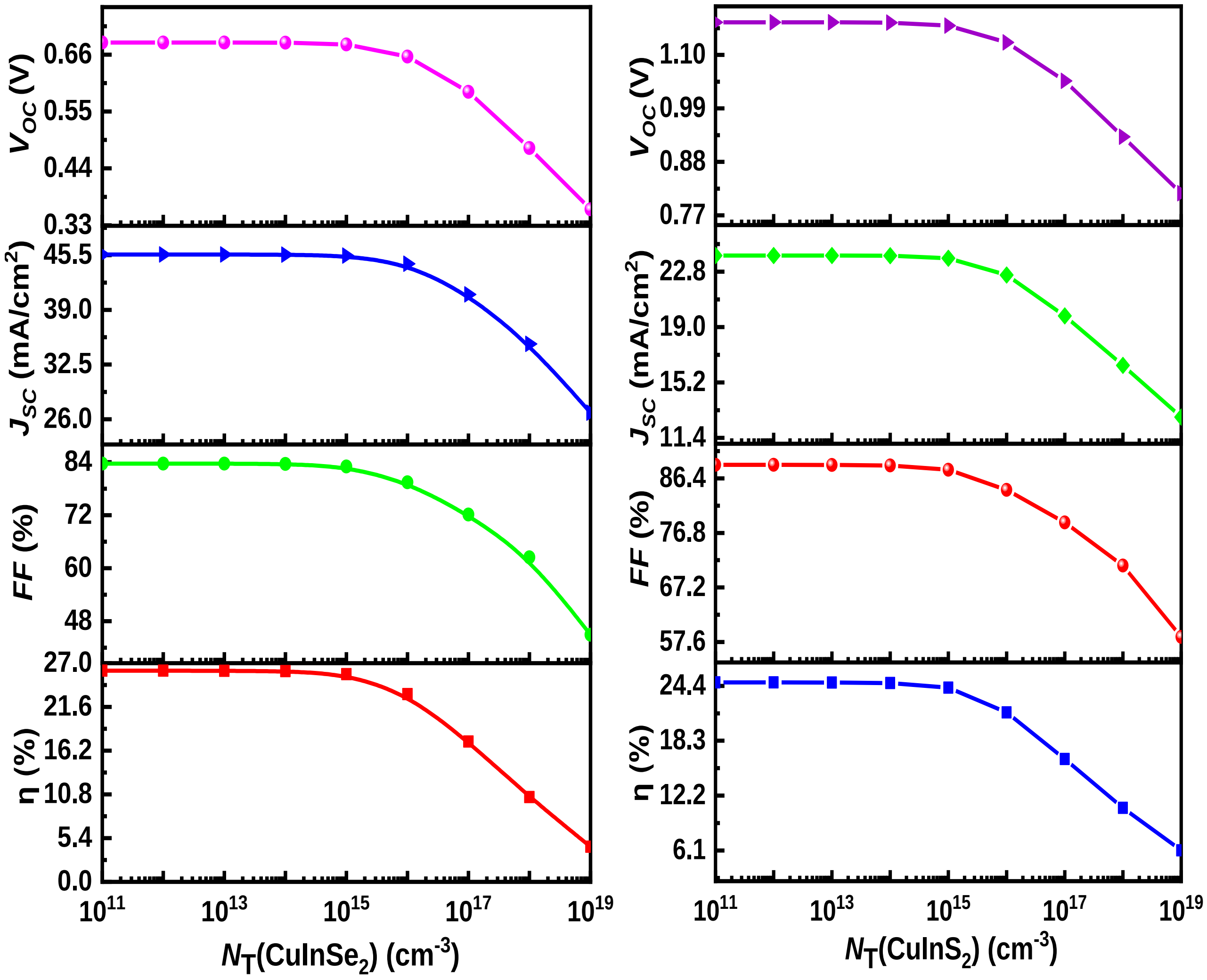

Figure IV.8: Effect of defect density of (a) $CuInSe_2$ and (b) $CuInS_2$ absorber layer on the solar cell performances.

For $CuInSe_2$, as the defect density (N_T) in the absorber increases, all photovoltaic parameters: open-circuit voltage (*Voc*), short-circuit current density (*Jsc*), fill factor (*FF*), and conversion efficiency (η) gradually decline, with a sharper drop beyond $N_T \approx 10^{15}$ cm^{-3}. At low defect concentrations ($\leq 10^{15}$ cm^{-3}), carrier recombination is minimized, allowing efficient carrier collection and yielding high *Voc*, *Jsc*, *FF*, and η, with values such as *Jsc* ≈ 45mA/cm^2, *Voc* ≈ 0.66V, *FF* ≈ 84%, and η ≈ 27% as shown in the figure. However, as defect density increases, more charge carriers become trapped or recombine non-radiatively, which means less current reaches the external circuit and efficiency plummets dropping to η ≈ 5% at the highest defect levels. Thus, minimizing trap states is essential for high performance in $CuInSe_2$ solar cells.

Similarly, for $CuInS_2$, higher defect state concentrations in the absorber bulk result in pronounced losses in device performance. All four key parameters fall sharply after $N_T \approx 10^{15}$cm^{-3}. At low trap densities, performance is optimal when *Jsc* ≈ 23mA/cm^2, *Voc* ≈ 1.1V, *FF* ≈ 86%, and η ≈ 24%. When defect density increases, carrier lifetimes shorten due to more recombination events, leading to a substantial reduction in output values. At $N_T \approx 10^{19}$ cm^{-3}, efficiency drops to nearly η ≈ 6%, demonstrating how sensitive $CuInS_2$ is to bulk defect concentration. Therefore, reducing trap states within the absorber layer is equally vital for achieving maximum efficiency in $CuInS_2$ solar cells.

Figure IV.9 illustrates how the quantum efficiency (QE) varies with wavelength for $CuInSe_2$ and $CuInS_2$ solar cells as a function of different defect state densities N_T in their absorber layers. This analysis provides deeper insight into the impact of increasing bulk defect concentration on the cells' ability to efficiently convert incident light across the spectrum, emphasizing that controlling such defects is essential for achieving optimal photovoltaic performance.

The figure shows that the quantum efficiency QE of $CuInSe_2$ decreases significantly as the trap defect density N_T in the absorber layer increases. As N_T increases, meaning more trap defects in the material, the probability of photogenerated electrons and holes being captured by these defects rises, leading to their recombination before reaching the electrodes. This effect is particularly evident at longer wavelengths (from about 800 to 1200 nm), where QE drops from nearly 100% at low N_T to less than 40% at high N_T, especially in the 800–1200 nm range. This indicates a reduction in carrier collection efficiency and a significant loss of current due to recombination at defect sites.

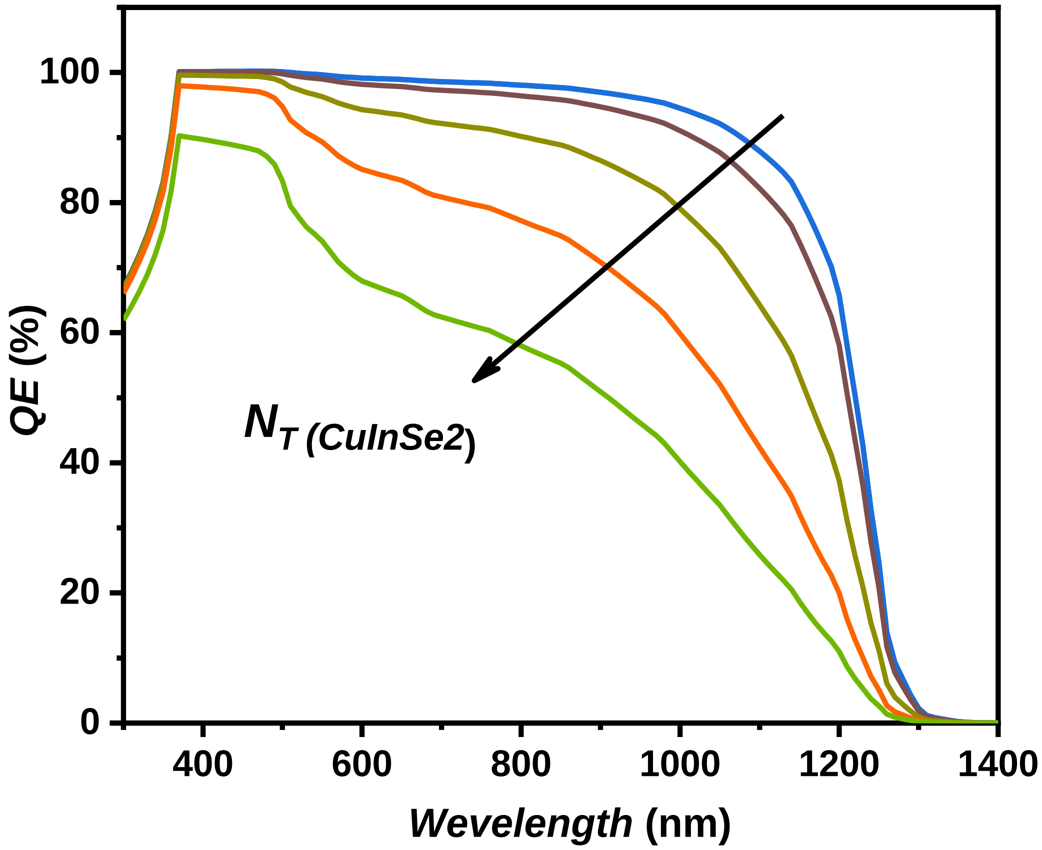

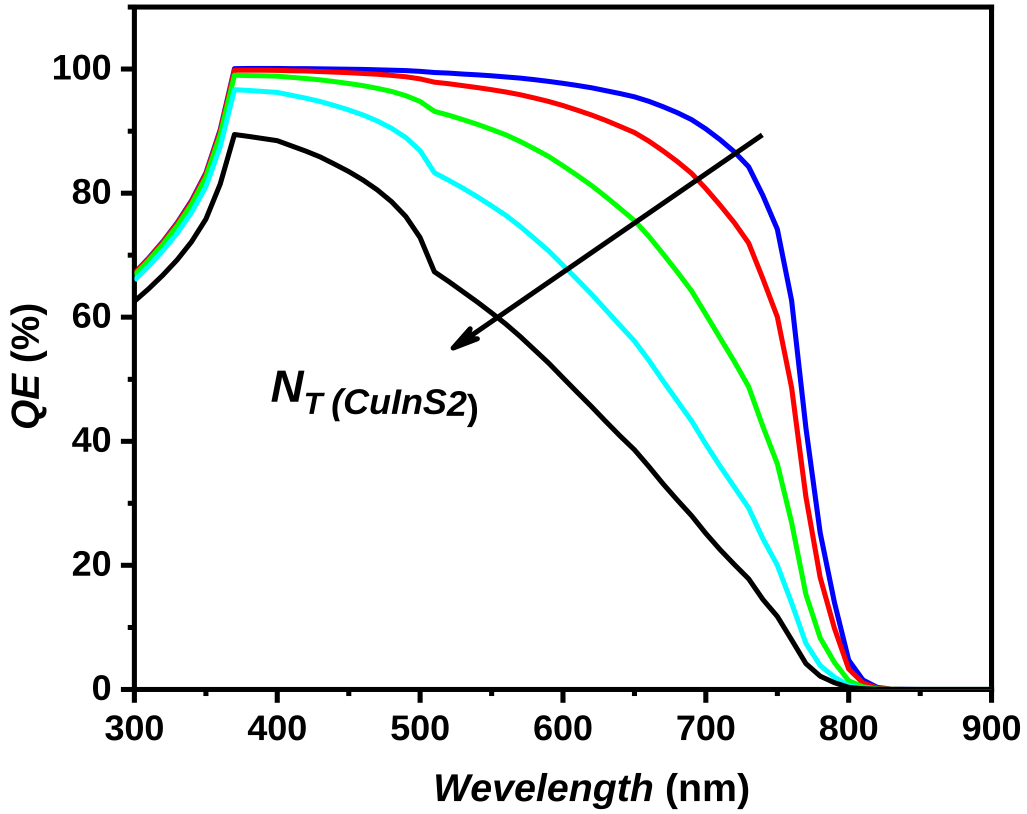

Figure IV.9: Quantum efficiency versus wavelength of $CuInSe_2$ and $CuInS_2$ solar cells with various N_T values.

Similarly, the figure for $CuInS_2$ shows that the quantum efficiency (QE) clearly decreases as NT increases. As the trap defect density in the material rises, the cell's ability to collect charge carriers diminishes and recombination effects become more significant, leading to a noticeable drop in QE, especially from around 500 nm up to the absorption edge at 800 nm. At high N_T, QE can fall below 60% at 500 nm and approach zero near 800 nm. This demonstrates that material quality (low N_T) is crucial for achieving strong spectral response and high conversion efficiency in $CuInS_2$ solar cells.

IV.8. Hybrid $CuInS_2$/CIGS solar cells modeling

In this study, we employed a hybrid approach combining $CuInS_2$ and CIGS to enhance light absorption and improve the conversion efficiency of thin-film solar cells. This type of hybridization was chosen because it allows for the complementary properties of each material to be exploited: $CuInS_2$ features a wider band gap that enables absorption of high-energy photons, while CIGS has a narrower band gap that facilitates efficient absorption of longer wavelengths. This results in a broader portion of the solar spectrum being utilized. The combination promotes the generation of more electron-hole pairs, improves charge separation, and reduces recombination losses, thereby increasing the overall cell efficiency. As illustrated in Figure IV.10, the layers are arranged in a way that ensures an optimal interaction between the materials to maximize light absorption and enhance charge transport.

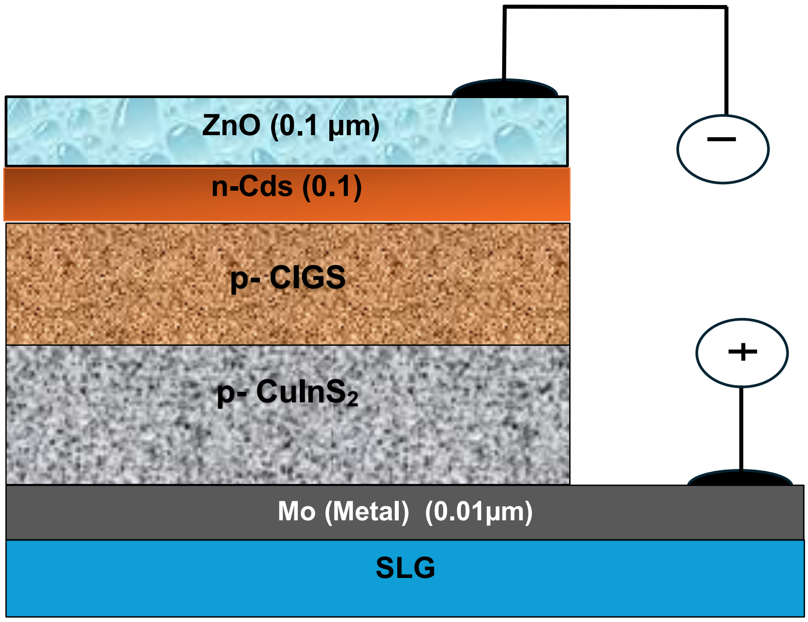

Figure IV.10: Hybrid solar cells for different structures: $CuInS_2$/CIGS/CdS/ZnO Hybrid solar cell structures.

The physical properties of the CIGS material employed in the simulation are already provided in the SCAPS-1 simulator database. The parameter values of CIGS, $CuInS_2$, CdS, and ZnO utilized in our simulation are summarized in Table IV.2.

Table IV.2: Parameters values of CIGS, $CuInS_2$, CdS and ZnO materials used in the simulation. [7,15-22].

Material properties	$CuInS_2$	CIGS	CdS	ZnO
Thickness (µm)	3	To be varied	0.1	0.1
Band gap [eV]	1.53	1.2	2.4	3.3
Electron affinity [eV]	4.5	4.5	4.2	4.6
Dielectric permittivity (relative)	10	10	10	9
CB (conduction band) effective density of states [cm^{-3}]	2×10^{18}	2×10^{18}	2×10^{18}	2.2×10^{18}
VB (valence band) effective density of states [$1/cm^3$]	2×10^{18}	2×10^{18}	1.5×10^{19}	1.8×10^{19}
Electron mobility µn[cm^2 /Vs]	50	100	100	100
Hole mobility µp [cm^2 /Vs]	20	20	25	25
Shallow uniform donor density N_D [$1/cm^3$]	0	0	1×10^{17}	1×10^{18}
Shallow uniform acceptor density N_A [$1/cm^3$]	1×10^{17}	To be varied	0	0

IV.8.1 Band diagrams

Hybridization in solar cell technology involves integrating multiple absorber materials with different band gaps into a single device structure, enabling broader and more efficient absorption of the solar spectrum. Each layer is optimized to capture photons of specific energy ranges, and by combining materials such as $CuInS_2$ and CIGS, hybrid solar cells are able to maximize light harvesting, enhance charge carrier separation, and minimize recombination losses. These improvements lead to superior photovoltaic performance and higher conversion efficiency compared to conventional single-junction cells.

In particular, when the CIGS layer is deposited over the $CuInS_2$ layer, the energy alignment and sequential arrangement of the layers play a fundamental role in enhancing cell performance. In this hybrid configuration, the $CuInS_2$ layer acts as a back surface field (BSF), which supports efficient charge transport by generating an internal electric field. This field repels minority carriers away from the back contact, reducing recombination rates at the rear interface. Consequently, charge collection efficiency is improved, resulting in a significant increase in the overall efficiency of the solar cell.

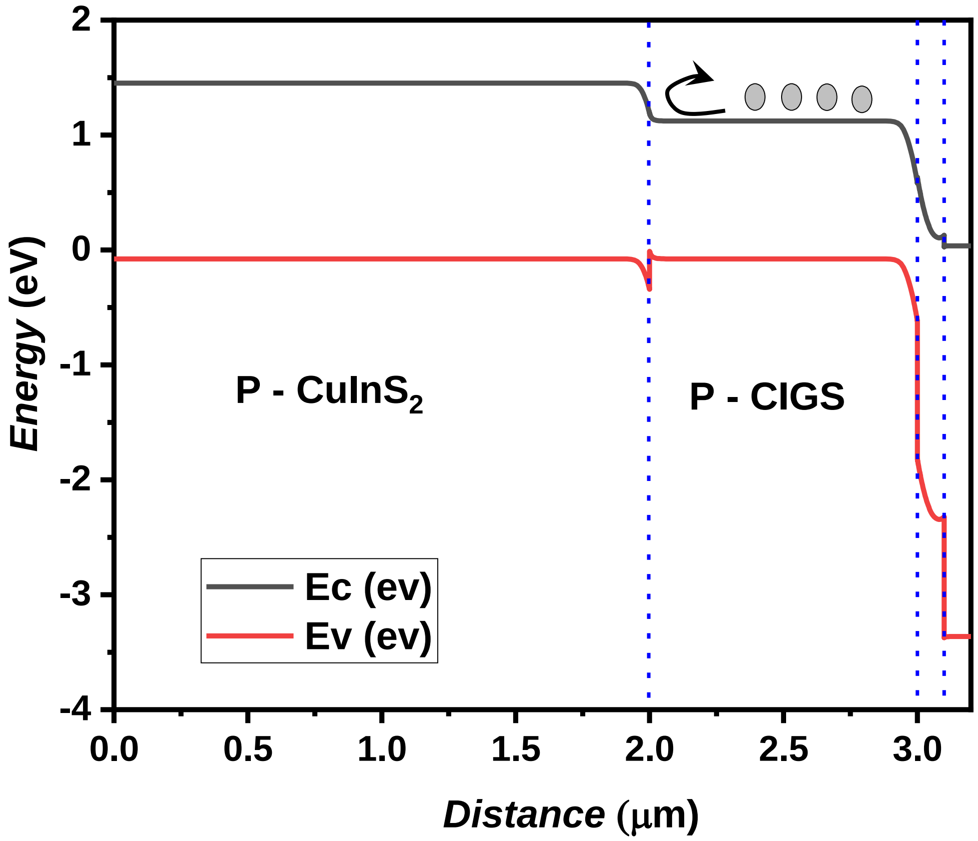

Figure IV.11: Energy band diagrams for CuInS$_2$/CIGS/CdS/ZnO Hybrid solar cell structures obtained by simulation.

Figure IV.11 illustrates the energy band diagrams for CuInS$_2$/CIGS/CdS/ZnO hybrid solar cell structures obtained by simulation. As shown in the figure, there are distinct gradients and variations in the conduction band edge (Ec) and valence band edge (Ev) at the interfaces between the different layers. This band alignment facilitates effective charge separation, as electrons and holes move across the energetic barriers, which reduces recombination and supports selective charge transport from one layer to the next.

Furthermore, the hybrid structure enables optimal utilization of the solar spectrum, since each material has a different band gap allowing it to absorb specific portions of incoming photons, thereby increasing the number of generated charge carriers and improving charge collection efficiency. The back surface field (BSF) created by the CuInS$_2$ layer repels minority carriers away from the back contact and minimizes recombination losses, ultimately resulting in enhanced overall conversion efficiency for the solar cell.

IV.8.2 Thickness optimization of CIGS absorber layers for $CuInS_2$/CIGS/CdS/ZnO Hybrid solar cell structures

Optimizing the thickness of the absorber layer is essential in hybrid $CuInS_2$/CIGS/CdS/ZnO solar cell structures to maximize device performance. Since the CIGS layer acts as the primary absorber for a broad range of wavelengths, its thickness directly affects key photovoltaic parameters including efficiency, open-circuit voltage, short-circuit current density, and fill factor. Figure IV.12 illustrates the variation in these parameters as a function of CIGS absorber thickness.

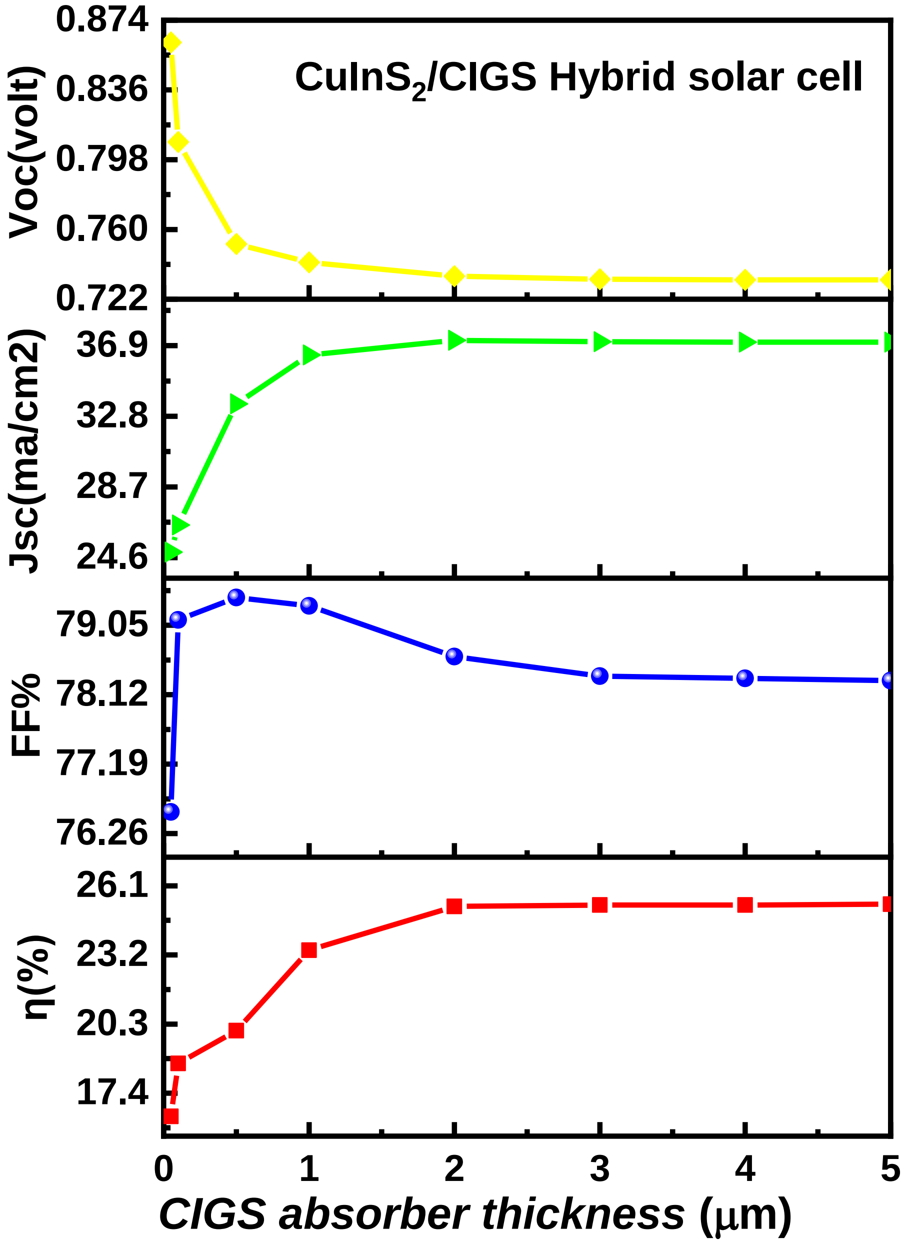

Figure IV.12: Hybrid solar cell performance as a function of CIGS absorber layer thickness.

As the thickness of the CIGS absorber increases in a $CuInS_2$/CIGS hybrid solar cell, several key photovoltaic parameters change due to improved light absorption and carrier generation. For example, at a thickness of 1 μm, the cell efficiency (η) reaches about 20% and the short-circuit current density (Jsc) is approximately 36 mA/cm². When the thickness increases to 2 μm, the efficiency rises to 25.2% and the Jsc increases to around 37 mA/cm².

These values show that both efficiency and current density become much higher as the absorber thickness increases up to 2 μm, because more incident light is absorbed, especially at longer wavelengths, generating more electron-hole pairs. However, beyond 2 μm, further increases in thickness result in only small performance improvements, indicating nearly all usable light has already been absorbed. In contrast, an absorber layer thinner than 2 μm leads to insufficient light absorption, significant decreases in cell efficiency, and lower Jsc. This emphasizes the importance of optimizing the absorber thickness to maximize solar cell performance.

IV.8.3 Optimization of Acceptor Density N_A in the CIGS Absorber Layer for $CuInS_2$/CIGS/CdS/ZnO Hybrid Solar Cell Structures

Understanding the acceptor concentration N_A in the absorber layer is crucial because it directly affects the electric field within the solar cell, which in turn influences charge separation, recombination rates, and overall device efficiency. Optimizing N_A ensures efficient carrier collection and minimal losses, leading to improved photovoltaic performance.

Figure IV.13 illustrates how varying the acceptor concentration N_A in the CIGS absorber layer impacts the performance of hybrid $CuInS_2$/CIGS solar cells. Key photovoltaic parameters such as open-circuit voltage *Voc*, short-circuit current density *Jsc*, fill factor *FF*, and efficiency η are plotted as functions of $N_A(CIGS)$.

As the acceptor concentration increases from low values ($\approx 10^{12}$ cm^{-3}), the open-circuit voltage Voc and efficiency (η) rise gradually and become optimal at concentrations around 10^{15} cm^{-3}. At this range, the cell achieves a good balance between efficient carrier collection and minimized recombination, resulting in high Voc, Jsc and η .

If N_A exceeds 10^{16} cm^{-3}, further increases lead to a sharp decline in Jsc and FF, indicating greater recombination and reduced carrier collection. Extremely high acceptor concentrations ($>10^{17}$ cm^{-3}) result in performance loss due to increased defects and space-charge limitations.

Therefore, the optimal acceptor concentration for maximum efficiency and reliable operation in hybrid CuInS$_2$CIGS cells is found to be about 10^{15} cm^{-3}, where the cell achieves maximum Voc and maintains high Jsc, FF, and η.

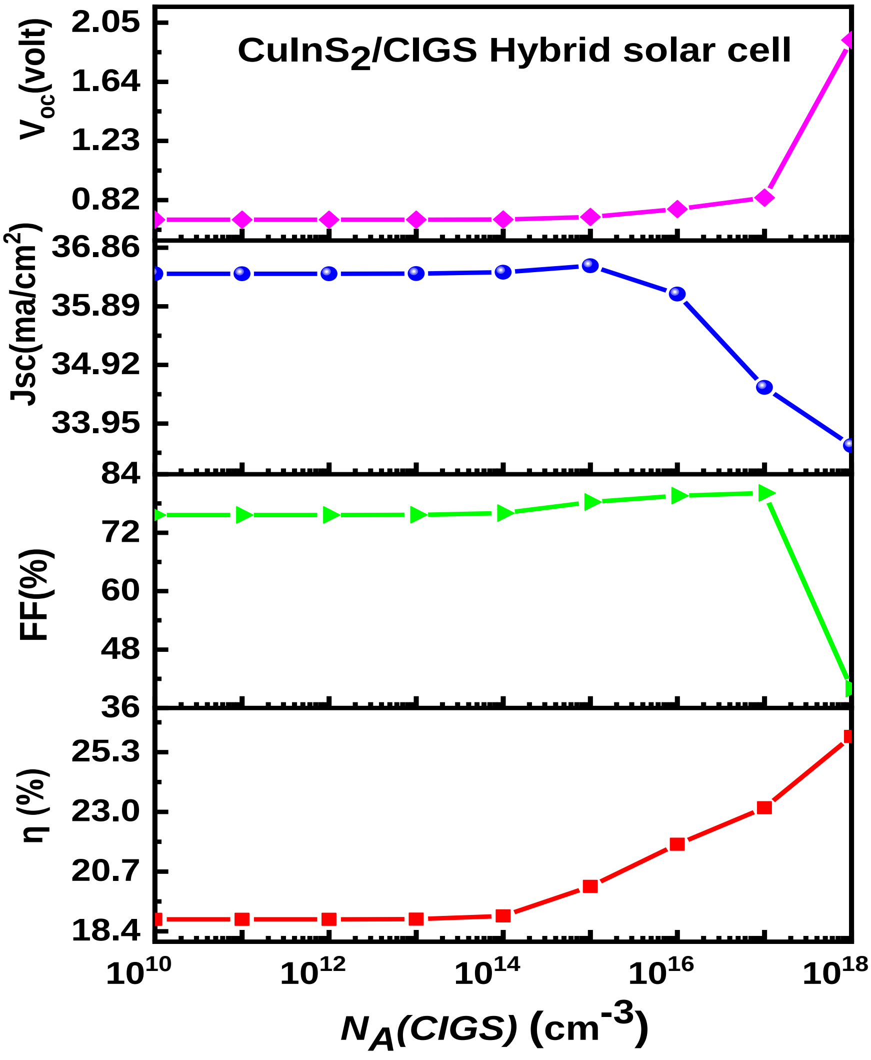

Figure IV.13: Effect of acceptor concentration of CIGS absorber layer, N_A(CIGS), on Hybrid CuInS$_2$/CIGS solar cell performance.

IV.8.4 Influence of defect state density N_t in the CIGS absorber layer on CuInS$_2$/CIGS/CdS/ZnO hybrid solar cell structures

Understanding the influence of defect state density (N_T) in the CIGS absorber is vital for enhancing the performance of hybrid CuInS$_2$/CIGS solar cells. These defect states serve as recombination centers for charge carriers, thereby significantly impacting major photovoltaic characteristics and the overall efficiency of the device. Figure IV.14 displays the simulated trends of open-circuit voltage (Voc), short-circuit current density (Jsc), fill factor (FF), and efficiency (η) with respect to N$_T$(CIGS) under front-side illumination.

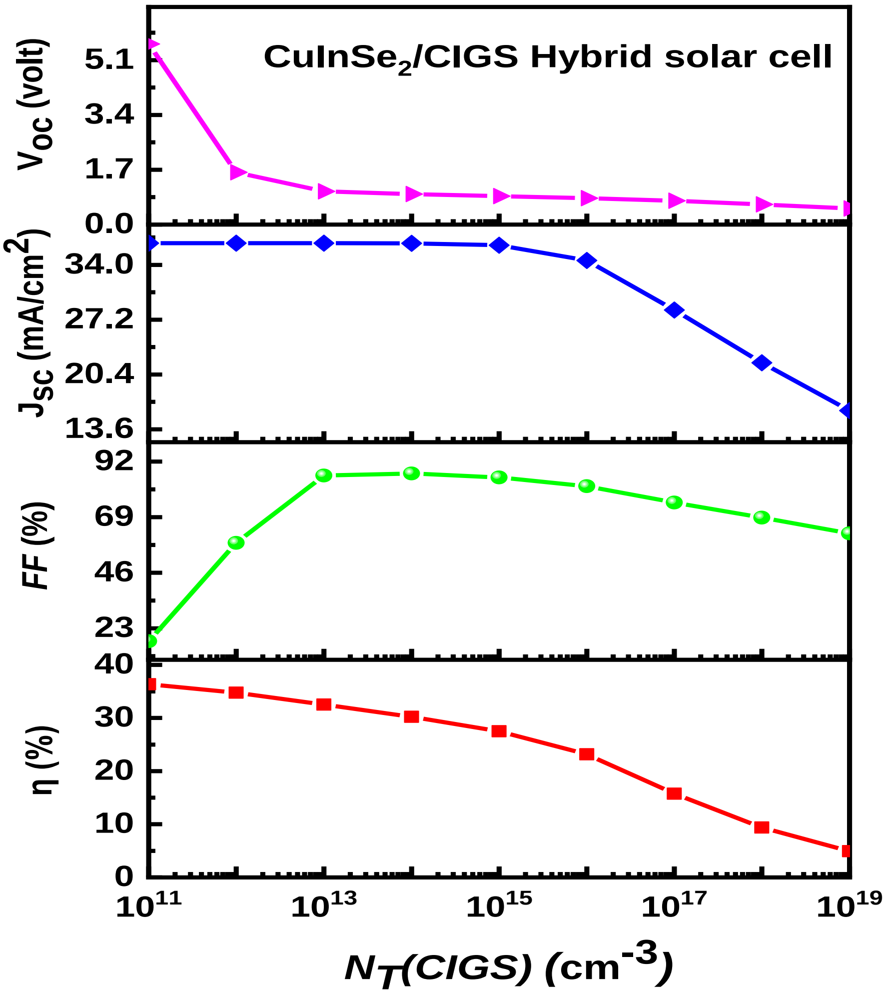

Figure IV.14: Effect of defect density of CIGS absorber layer, *N*$_T$(CIGS), on Hybrid CuInS$_2$/CIGS solar cells performances.

Recent simulation studies show that a defect density near 10^{13} cm^{-3} in the CIGS absorber layer yields the optimal solar cell performance. At this value, the device balances minimal recombination losses with efficient carrier collection, achieving a high open-circuit voltage (Voc ≈ 0.92 V), robust short-circuit current density (Jsc ≈ 33.0 mA/cm^2), fill factor (FF ≈ 82%), and high overall efficiency. If the defect density decreases below or increases above this optimal value, performance drops significantly higher densities introduce excessive recombination centers, while lower densities have diminishing returns on further improvement. Therefore, controlling and maintaining N$_T$ around 10^{13} cm^{-3} is critical for maximizing conversion efficiency and photovoltaic output in hybrid CuInS$_2$/CIGS solar cells.

IV.9 Conclusion

This chapter systematically investigates the modeling, optimization, and hybridization of chalcopyrite thin-film solar cells based on $CuInSe_2$, $CuInS_2$, and their combination with CIGS, using the SCAPS-1D simulation platform. The results demonstrate that careful control of critical design parameters absorber thickness, acceptor concentration, and defect state density is essential for maximizing photovoltaic performance in these devices. An optimal absorber thickness of around 2–3 µm, acceptor densities between 10^{16} and 10^{17} cm^{-3}, and low defect densities ($<10^{15}$ cm^{-3}) enable high open-circuit voltage, short-circuit current density, fill factor, and conversion efficiency values that align with, or even surpass, experimental benchmarks.

The study further highlights the advantages of hybrid solar cell architectures that integrate layers of $CuInS_2$ and CIGS. This approach leverages complementary band gaps for enhanced light harvesting, efficient charge separation, and minimized recombination loss, resulting in superior device performance compared to conventional single-junction cells. The hybrid design not only improves efficiency and stability but also allows for reduction in the use of critical materials, paving the way for more cost-effective and sustainable photovoltaics.

Overall, the findings in this chapter underline the pivotal role of chalcopyrite materials and advanced simulation techniques in the design of next-generation thin-film solar cells, and provide a robust blueprint for further research and innovation in high-efficiency, low-cost, and scalable photovoltaic technologies.

References

[1] Mudryi, A. V., Victorov, I. A., Gremenok, V. F., Patuk, A. I., Shakin, I. A., & Yakushev, M. V. (2003). Optical spectroscopy of chalcopyrite compounds CuInS2, CuInSe2 and their solid solutions. Thin Solid Films, 431, 197-199.

[2] A. Sajid, S. Ullah, G. Murtaza, R. Khenata, A. Manzar, and S. B. Omran, " Electronic structure and optical properties of chalcopyrite CuYZ2 (Y= Al, Ga, In; Z= S, Se): an ab initio study," J. Optoelectronics and Advanced Materials, vol. 16, p.76, 2014

[3] Jiang, J., Giridharagopal, R., Jedlicka, E., Sun, K., Yu, S., Wu, S., ... & Xin, H. (2020). Highly efficient copper-rich chalcopyrite solar cells from DMF molecular solution. Nano Energy, 69, 104438.

[4] Dejene, F. B. (2009). The structural and material properties of CuInSe2 and Cu (In, Ga) Se2 prepared by selenization of stacks of metal and compound precursors by Se vapor for solar cell applications. Solar Energy materials and Solar cells, 93(5), 577-582.

[5] Díaz-Loera, A., Ramos-Serrano, J. R., & Calixto, M. E. (2022). Semiconducting CuIn (SX, Se1− X) 2 thin-film solar cells modeling using SCAPS-1D. MRS Advances, 7(2), 28-32.

[6] Sood, M., Bombsch, J., Lomuscio, A., Shukla, S., Hartmann, C., Frisch, J., ... & Siebentritt, S. (2022). Origin of interface limitation in Zn (O, S)/CuInS2-based solar cells. ACS Applied Materials & Interfaces, 14(7), 9676-9684.

[7] Rahal, A., Bouchama, I., Ghebouli, M. A., Ghebouli, B., Fatmi, M., Alomairy, S., ... & Chellouche, M. (2025). Optimization of structural and electronic properties in CuO/CIGS hybrid solar cells for high-efficiency, sustainable energy conversion. RSC advances, 15(29), 23311-23318.

[8] Guillen, C., Martínez, M. A., Herrero, J., & Gutierrez, M. T. (1999). Chemical studies of solar cell structures based on electrodeposited CuInSe2. Solar energy materials and solar cells, 58(2), 219-224.

[9] Hála, M., Fujii, S., Redinger, A., Inoue, Y., Rey, G., Thevenin, M., ... & Siebentritt, S. (2015). Highly conductive ZnO films with high near infrared transparency. Progress in Photovoltaics: Research and Applications, 23(11), 1630-1641.

[10] Sk, M., Islam, M. T., & Gourav. (2024). Exploring the structural, electronic, optical, transport, and photovoltaic properties of Rb2LiGa (Br/I) 6 using DFT and SCAPS-1D simulations. Scientific Reports, 14(1), 24813.

[11] Repins, I., Contreras, M., Romero, M., Yan, Y., Metzger, W., Li, J., ... & Noufi, R. (2008, May). Characterization of 19.9%-efficient CIGS absorbers. In 2008 33rd IEEE photovoltaic specialists conference (pp. 1-6). IEEE.

[12] Hashimoto, Y., Kohara, N., Negami, T., Nishitani, N., & Wada, T. (1998). Chemical bath deposition of Cds buffer layer for GIGS solar cells. Solar Energy Materials and Solar Cells, 50(1-4), 71-77.

[13] Werner, F., Colombara, D., Melchiorre, M., Valle, N., El Adib, B., Spindler, C., & Siebentritt, S. (2016). Doping mechanism in pure CuInSe2. Journal of Applied Physics, 119(17).

[14] Look, D. C., & Manthuruthil, J. C. (1976). Electron and hole conductivity in CuInS2. Journal of Physics and Chemistry of Solids, 37(2), 173-180.

[15] Javed, A., Nasir, M. F., Azam, S., & Amin, M. A. (2025). Numerical simulation for a suitable electron transport layer of a lead-free CuInSe2 based perovskite solar cell and PV module. International Journal of Electrochemical Science, 20(1), 100893.

[16] Mostefaoui, M., Mazari, H., Khelifi, S., Bouraiou, A., & Dabou, R. (2015). Simulation of high efficiency CIGS solar cells with SCAPS-1D software. Energy Procedia, 74, 736-744.

[17] Nykyruy, L. I., Yavorskyi, R. S., Zapukhlyak, Z. R., Wisz, G., & Potera, P. (2019). Evaluation of CdS/CdTe thin film solar cells: SCAPS thickness simulation and analysis of optical properties. Optical Materials, 92, 319-329.

[18] Ait Abdelkadir, A., Oublal, E., Sahal, M., & Gibaud, A. (2022). Numerical simulation and optimization of n-Al-ZnO/n-CdS/p-CZTSe/p-NiO (HTL)/Mo solar cell system using SCAPS-1D. Results in Optics, 8, 100257.

[19] Teyou Ngoupo, A., Ouédraogo, S., & Ndjaka, J. M. (2019). Numerical analysis of interface properties effects in CdTe/CdS: O thin film solar cell by SCAPS-1D. Indian Journal of Physics, 93(7), 869-881.

[20] Biswas, S. K., Mim, M. K., & Ahmed, M. M. (2023). Design and Simulation of an Environment-Friendly ZrS2/CuInS2 Thin Film Solar Cell Using SCAPS 1D Software. Advances in Materials Science and Engineering, 2023(1), 8845555.

[21] Kotbi, A., Hartiti, B., Batan, A., Fadili, S., Ridah, A., & Thevenin, P. (2019). The effect of several parameters on the performance of C-uIns2-based solar cells using the SCAPS-1D software. Journal of Fundamental and Applied Sciences, 11(2), 699-716.

[22] Esman, A. K., Zykov, G. L., Potachits, V. A., & Kuleshov, V. K. (2020). Simulation of thin-film solar cells with a CuInSe2 chalcopyrite structure. Энергетика. Известия высших учебных заведений и энергетических объединений СНГ, 63(1), 5-13.

[23] Yakushev, M. V., Mudryi, A. V., Gremenok, V. F., Zalesski, V. B., Romanov, P. I., Feofanov, Y. V., ... & Tomlinson, R. D. (2003). Optical properties and band gap energy of CuInSe2 thin films prepared by two-stage selenization process. Journal of Physics and Chemistry of Solids, 64(9-10), 2005-2009.

[24] Abaab, M., Kanzari, M., Rezig, B., & Brunel, M. (1999). Structural and optical properties of sulfur-annealed CuInS2 thin films. Solar Energy Materials and Solar Cells, 59(4), 299-307.

[25] Wang, C., Li, X., & Wang, Y. (2017, October). First-principles Calculations on Electronic and Elastic Properties of CuInS2 andCuInSe2 at Ambient Pressure. In 7th International Conference on Management, Education, Information and Control (MEICI 2017) (pp. 176-180). Atlantis Press.

[26] Möller, H. J. (1993). Semiconductors for solar cells. In Semiconductors for solar cells (pp. 343-343).

[27] Chopra, K. L., & Das, S. R. (1983). Why thin film solar cells? In Thin film solar cells (pp. 1-18). Boston, MA: Springer US.

General conclusion

General conclusion

The global energy landscape is undergoing a profound and necessary transformation due to the convergence of environmental degradation, economic pressures, and increasing social demands. Since the 1980s, humanity has surpassed the Earth's biocapacity, resulting in escalating climate change, biodiversity loss, and ecological instability. At the core of this crisis lies the continued reliance on fossil fuels, which not only contribute significantly to global greenhouse gas emissions but are also finite and subject to volatile geopolitical dynamics. In parallel, the global demand for electricity is rapidly increasing, especially in developing countries where energy access remains a major development barrier. Over one billion people still live without electricity, further reinforcing the urgent need for clean, accessible, and reliable energy alternatives. Addressing this dual challenge environmental sustainability and energy equity necessitates a decisive shift toward renewable, decentralised, and low-carbon energy technologies.

Solar energy stands out as one of the most promising renewable energy solutions. The sun provides more energy to the Earth's surface in a single hour than global humanity consumes in an entire year. This unmatched potential makes solar power a crucial pillar in the global transition to sustainable energy. Unlike fossil fuels, solar energy is clean, abundant, and geographically universal. Moreover, photovoltaic (PV) technologies capable of converting sunlight directly into electricity are especially attractive due to their scalability, modularity, and silent operation. PV systems can be deployed in diverse settings, from remote villages to urban rooftops, offering a distributed model of energy generation that reduces transmission losses and enhances grid resilience.

The evolution of photovoltaic technologies has progressed through multiple generations. First-generation silicon-based solar cells continue to dominate the market because of their high efficiencies and long-term reliability. However, the production of crystalline silicon involves energy-intensive processes, high material consumption, and rigid module design, which collectively raise costs and limit their integration in flexible or lightweight applications. In response to these limitations, second-generation thin-film technologies have been developed, aiming to offer competitive performance with lower production costs, smaller ecological footprints, and greater design versatility.

Among thin-film materials, copper-based chalcogenides have shown remarkable potential. Compounds such as $Cu(In,Ga)Se_2$, $CuInSe_2$ (CISe), and $CuInS_2$ (CIS) are known for their strong absorption coefficients, direct band gaps in the ideal range, and high tolerance to structural defects.

Particularly, CISe and CIS belong to the chalcopyrite crystal family and exhibit excellent photoelectrical stability and compatibility with low-temperature deposition techniques. These features make them ideal candidates for high-efficiency, cost-effective solar cell applications.

However, further improvements in performance and versatility have been pursued through the development of alloy systems such as CuIn $(Se_{1-x}\,S_x)_2$. By partially substituting selenium with sulfur, researchers can finely tune the band gap of the absorber material. This band gap tunability enables better alignment with the solar spectrum, potentially increasing power conversion efficiency. Moreover, sulfur incorporation can enhance thermal and structural stability, reduce grain boundary recombination, and expand the range of suitable deposition processes. These advantages make CuIn $(Se_{1-x}\,S_x)_2$ a versatile platform for next-generation PV devices.

Several experimental and theoretical studies have examined the influence of sulfur content on the structural, optical, and electrical properties of CuIn $(Se_{1-x}\,S_x)_2$. Studies using solvothermal synthesis, Bridgman growth, and sulfurisation processes have shown that lattice parameters, optical band gaps, and electronic behaviour can all be controlled by adjusting the sulfur content. Theoretical calculations have supported these findings, showing that sulfur substitution alters the electronic band structure, defect formation energies, and optical constants of the material. These results confirm the viability of CuIn $(Se_{1-x}\,S_x)_2$ as a material system for efficient and stable thin-film solar cells.

Despite these valuable contributions, most studies have focused on the binary endpoints of the alloy system ($CuInSe_2$ and $CuInS_2$), leaving a knowledge gap regarding the intermediate compositions. These intermediate states are particularly important because they may offer superior trade-offs between light absorption, carrier transport, and thermal resilience. To address this gap, the present study adopts an integrated approach that combines first-principles simulations using density functional theory (DFT) and device-level modelling using the SCAPS-1D simulator. DFT simulations, conducted with the CASTEP module in the Materials Studio environment, provide insight into structural parameters, electronic band structures, dielectric properties, and optical behaviour across the full range of sulfur compositions.

To complement this material-level understanding, the SCAPS-1D numerical simulation tool is employed to evaluate the photovoltaic performance of full solar cell structures incorporating $CuIn(Se_{1-x}\,S_x)_2$ absorbers. The simulated devices are analysed under standard test conditions, with systematic variation in absorber thickness, acceptor doping concentration, and defect density. Key photovoltaic parameters—including short-circuit current density, open-circuit voltage, fill factor, and overall efficiency are calculated and examined to determine optimal operating conditions and structural configurations.

The integration of DFT and SCAPS-1D allows for a comprehensive understanding of the material-device relationship and offers a validated pathway toward the optimization of CuIn $(Se_{1-x} S_x)_2$ based solar cells. This dual-modelling strategy not only helps identify performance-limiting factors but also provides design principles for achieving high efficiency, long-term stability, and commercial scalability. The results of this work contribute to the broader effort of realizing sustainable and affordable photovoltaic solutions, especially in regions where energy poverty and environmental vulnerability intersect.

Moreover, future work should focus on experimental validation of the predicted material properties and device performances, development of scalable and cost-effective fabrication techniques for the tailored CuIn $(Se_{1-x} S_x)_2$ alloys, as well as long-term stability and durability assessments under real-world operating conditions. Additionally, addressing challenges related to defect control and interface engineering will be crucial for commercial deployment. This integrated approach is imperative to pave the way for large-scale manufacturing and adoption of sustainable photovoltaic technologies.

Ultimately, the outcomes of this work are expected to guide both research and industrial applications, contributing to sustainable energy solutions, energy equity, and global climate action.

Abstract

In this work, we investigated the structural, electronic, and optical properties of $CuInSe_2$ $CuInS_2$, and their alloy $CuIn(Se_{1-x}S_x)_2$ using CASTEP, based on density functional theory (DFT) with the Generalized Gradient Approximation (GGA). These simulations enabled a detailed analysis of how compositional variations and doping levels affect the band structure, dielectric function, and optical absorption characteristics. The study was complemented by SCAPS-1D simulations, which were used to simulate solar cell models incorporating these materials at compositions $x = 0$ and $x = 1$., allowing evaluation of their photovoltaic performance. Furthermore, a hybrid solar cell structure combining $CuInS_2$ and CIGS layers was modeled to examine the impact and importance of hybridization in reducing recombination losses, enhancing charge separation, and improving overall cell efficiency. The combined approach revealed that optimal tuning of doping concentration and absorber thickness enhances efficiency and overall solar cell performance, making $CuIn(Se_{1-x}S_x)_2$ a highly promising candidate for next-generation thin-film solar technologies.

Keywords: CASTEP, GGA, DFT, doping, structural properties, electronic properties, optical properties, SCAPS, hybrid solar cells, recombination, performance, efficiency.

ملخص

في هذا البحث، تم دراسة الخصائص البنيوية والإلكترونية والبصرية لمواد $CuInSe_2$ ، $CuInS_2$ وسبائكها $CuIn(Se_{1-x}S_x)_2$ باستخدام برنامج CASTEP المعتمد على نظرية دالة الكثافة DFT مع تقريب التدرج المعمم GGA. أتاحت هذه الحسابات دراسة تفصيلية لتأثير التغيرات التركيبية ومستويات التطعيم على بنية الحزمة، والدالة العازلة، وخصائص الامتصاص الضوئي. تم تكملة الدراسة باستخدام برنامج SCAPS-1D لمحاكاة هياكل الخلايا الشمسية المعتمدة على هذه المواد للتركيبين $x = 0$ و$x = 1$ ، مما مكن من تقييم الأداء الكهروضوئي لها. كما تم دراسة نظام شمسي مهجن يجمع بين طبقتي $CuInS_2$ وCIGS لفهم مدى تأثير وأهمية التهجين في تقليل خسائر إعادة التركيب، وتحسين فصل الحاملة الكهربائية، وزيادة كفاءة الخلية. أظهرت النتائج أن الضبط الأمثل لتركيز التشويب وسمك طبقة الامتصاص يؤدي إلى تحسين الكفاءة والأداء الكلي للخلايا الشمسية، مما يجعل $CuIn(Se_{1-x}S_x)_2$ مرشحًا واعدًا لتقنيات الخلايا الشمسية الرقيقة من الجيل القادم.

الكلمات المفتاحية: CASTEP، GGA، DFT ، التطعيم، الخصائص البنيوية، الخصائص الإلكترونية، الخصائص البصرية، SCAPS، الخلايا الشمسية المهجنة، إعادة التركيب، الأداء، الكفاءة.

Résumé

Dans cette étude, nous avons examiné les propriétés structurales, électroniques et optiques des matériaux $CuInSe_2$, $CuInS_2$ et de leur alliage $CuIn(Se_{1-x}S_x)_2$ à l'aide du logiciel CASTEP, fondé sur la théorie de la fonctionnelle de la densité (DFT) avec l'approximation du gradient généralisé (GGA). Ces simulations ont permis une analyse approfondie de l'impact des variations de composition et des niveaux de dopage sur la structure de bande, la fonction diélectrique et les caractéristiques d'absorption optique. L'étude a été complétée par l'utilisation du simulateur SCAPS-1D pour simuler des modeles des structures de cellules solaires intégrant ces matériaux aux compositions $x = 0$ et $x = 1$, permettant ainsi l'évaluation de leurs performances photovoltaïques. De plus, une structure de cellule solaire hybride combinant des couches de $CuInS_2$ et de CIGS a été modélisée afin d'examiner l'impact et l'importance de l'hybridation dans la réduction des pertes par recombinaison, l'amélioration de la séparation des charges et l'optimisation de l'efficacité globale de la cellule. Cette approche combinée a montré que l'ajustement optimal du dopage et de l'épaisseur de la couche absorbante améliore significativement le rendement et la performance globale, faisant de $CuIn(Se_{1-x}S_x)_2$ un candidat très prometteur pour les technologies photovoltaïques à couches minces de nouvelle génération.

Mots clés : CASTEP, GGA, DFT, dopage, propriétés structurales, propriétés électroniques, propriétés optiques, SCAPS, cellules solaires hybrides, recombinaison, performance, rendement.